2017

Enhancement of Intake Generated Swirl to Improve Lean Combustion

Mark Edward Ives
University of Windsor

Enhancement of Intake Generated Swirl to Improve Lean Combustion

by

Mark Ives

A Thesis
Submitted to the Faculty of Graduate Studies
through the Department of Mechanical, Automotive and Materials Engineering
in Partial Fulfillment of the Requirements for
the Degree of Master of Applied Science
at the University of Windsor

Windsor, Ontario, Canada

Enhancement of Intake Generated Swirl to Improve Lean Combustion

by

Mark Ives

APPROVED BY:

_____

X. Chen

Department of Electrical and Computer Engineering

_____

J. Tjong

Department of Mechanical, Automotive, and Materials Engineering

_____

G. T. Reader, Co-Advisor

Department of Mechanical, Automotive, and Materials Engineering

_____

M. Zheng, Co-Advisor

Department of Mechanical, Automotive, and Materials Engineering

04 October 2017

AUTHOR'S DECLARATION OF ORIGINALITY

I hereby certify that I am the sole author of this thesis and that no part of this thesis has been published or submitted for publication.

I certify that, to the best of my knowledge, my thesis does not infringe upon anyone's copyright nor violate any proprietary rights and that any ideas, techniques, quotations, or any other material from the work of other people included in my thesis, published or otherwise, are fully acknowledged in accordance with the standard referencing practices. Furthermore, to the extent that I have included copyrighted material that surpasses the bounds of fair dealing within the meaning of the Canada Copyright Act, I certify that I have obtained a written permission from the copyright owner(s) to include such material(s) in my thesis and have included copies of such copyright clearances to my appendix.

I declare that this is a true copy of my thesis, including any final revisions, as approved by my thesis committee and the Graduate Studies office, and that this thesis has not been submitted for a higher degree to any other University or Institution.

ABSTRACT

As stricter emission and fuel efficiency regulations continue to be set forth by government regulating bodies, the need to optimize the gasoline engine and control every aspect of combustion has never been greater. Gasoline engines which utilize exhaust gas recirculation (EGR) and lean-burn combustion systems are attractive pathways which have shown potential in reaching these targets. However, due to the suppressed reactivity, the ability to ignite and completely burn the mixture is reduced and can lead to unstable operation. It is well established that increased in-cylinder air motion can improve the mixing and turbulence generation which in turn, increases the probability of ignition and the flame velocity. This work investigates the potential benefit of enhanced swirl motion, which is the rotation of charge about the cylinder axis, under lean engine operating conditions. The ultimate objective is to extend the lean-limit of combustion and increase the thermal efficiency.

Steady flow tests were conducted on a cylinder head from a single-cylinder research engine using an in-house developed flow bench system. Swirl speeds were measured using a vane-type swirl meter. Computational fluid dynamics (CFD) simulations were conducted to investigate different intake geometries to enhance the swirl motion. The intake runner geometry which produced an increase in the swirl speed was tested on the flow bench. The steady-flow results showed an increase in the swirl ratio over the baseline measurements. Finally, engine tests were conducted to investigate the effect of the enhanced swirl. The engine test results demonstrated that the lean limits were extended and the thermal efficiency was increased with the enhanced swirl.

DEDICATION

This Thesis is dedicated to my parents, Doug and Cindy, who have supported me through all of my obstacles in life. Without your unconditional love, all of my success and goals I have achieved thus far would not have been possible.

Also, to my future wife Paulina who has always been loving, supportive and more than patient with me while I pursue my goals.

ACKNOWLEDGEMENTS

I wish to express my deepest gratitude to my advisors, Dr. Ming Zheng and Dr. Graham T. Reader, for their excellent guidance, compassion, patience, and providing me with an excellent environment for conducting research. I would also like to express my appreciation for Dr. Jimi Tjong for his support and for allowing me to learn from him and the rest of the members from the Ford Powertrain Engineering Research and Development Center at the Ford Motor Company Canada in Windsor, Ontario. I also express my appreciation to my other committee member Dr. Xiang Chen for his guidance and advice on different aspects on my research.

I express my sincere appreciation to the members of the Clean Diesel Engine Laboratory group; Dr. Meiping Wang, Dr. Shui Yu, Dr. Xiao Yu, Dr. Tadanori Yanai, Dr. Marko Jeftic, Dr. Prasad Divekar, Dr. Tongyang Gao, Shouvik Dev, Kelvin Xie, Zhenyi Yang, Qingyuan Tan, Geraint Bryden, Chris Aversa, Zhu Hua, Navjot Sandhu, and Divyanshu Purohit who supported me throughout the course of my master's program. I am utmost grateful for everyone's aspiring guidance, valuable feedback, and advice during my work. I am sincerely grateful to them for sharing their honest and illuminating views on some issues related towards the progress of my work. It has truly been a pleasure working with you all.

I would like to thank the faculty and staff including Mr. Bruce Durfy, who assisted in many technical areas both for my research and other areas of the lab.

I would like to thank the following organizations for their funding support: the University of Windsor, the Ford Motor Company Canada, the Natural Sciences and Engineering Research Council of Canada, AUTO21, and the Canada Research Chairs Program.

TABLE OF CONTENTS

LIST OF TABLES

LIST OF FIGURES

LIST OF ABBREVIATIONS

Uppercase

3D	Three Dimensional	[–]
A_t	Throat Area	[m^2]
AFR	Air Fuel Ratio	[–]
ATDC	After Top Dead Center	[–]
BDC	Bottom Dead Center	[–]
BTDC	Before Top Dead Center	[–]
CA	Crank Angle	[°]
CA5	Crank Angle at 5 % Cumulative Heat Released	[°]
CA50	Crank Angle at 50 % Cumulative Heat Released	[°]
CA95	Crank Angle at 95 % Cumulative Heat Released	[°]
CAI	California Analytical Instruments	[–]
CARB	California Air Resources Board	[–]
C_d	Discharge Coefficient	[–]
C_f	Flow Coefficient	[–]
C_s	Swirl Coefficient	[–]
CCEL	Clean Combustion Engine Laboratory	[–]
CI	Compression Ignition	[–]
CO	Carbon Monoxide	[–]
CO_2	Carbon Dioxide	[–]
COV	Coefficient of Variation	[%]
DI	Direct Injection	[–]

EGR	Exhaust Gas Recirculation	[–]
EPA	(US) Environmental Protection Agency	[–]
FPGA	Field Programmable Gate Array	[–]
LHV	Lower Heating Value	[MJ/kg]
NO_x	Nitrogen Oxides	[–]
NMOG	Non-Methane Organic Gases	[–]
P_{ind}	Indicated Power	[kW]
PM	Particulate Matter	[–]
SI	Spark Ignition	[–]
SR	Swirl Ratio	[–]
SCR	Selective Catalytic Reduction	[–]
SOC	Start of Combustion	[–]
TDC	Top Dead Center	[–]
THC	Total Hydrocarbon	[–]
TWCC	Three Way Catalytic Converter	[–]
UHC	Unburnt Hydrocarbon	[–]
US	United States	[–]

Lowercase

kg	Kilogram Mass	[kg]
$\dot{m}$	Mass Flow Rate	[kg/s]
p	Absolute Pressure	[Pa]
rpm	Revolutions Per Minute	[rpm]

Greek

λ	Excess Air Ratio	[–]
γ	Ratio of Specific Heats	[–]
θ	Crank Angle	[°]
η_{th}	Indicated Thermal Efficiency	[%]
ρ	Density	[kg/m^3]

CHAPTER 1: INTRODUCTION

This chapter presents the motivation for this thesis work and provides background information on the relevant challenges associated with present day internal combustion engines. The major objectives of this work will be defined along with the associated engineering challenges. An overall outline of the thesis is shown in Figure 1-9.

1.1 Research Motivation

The internal combustion engine has been used for more than 150 years primarily as a source to convert chemical energy into mechanical energy [1,16]. The extracted mechanical energy has been used for propulsion systems of automotive vehicles, water vessels, and airplanes as well as a means of electric power generation to name a few. The credit for the gasoline internal combustion engine is attributed to Nicolaus A. Otto (1832-1891) who developed a working engine prototype in 1876 which operated with four strokes of the piston (intake, compression, combustion, and exhaust) [1].

The next major development in internal combustion engines came from Rudolf Diesel in 1895 [2]. Diesel filed a patent which outlined his concept of a compression ignition engine commonly known today as the diesel engine. Traditionally, the diesel engine has had a higher efficiency than a gasoline engine, which is attributed to the higher compression ratio, lean operation, and the lack of intake throttling. The compression ratio of gasoline engines is limited by the fuel property of gasoline. The octane number of gasoline is a measure of resistance to knock. The larger the octane number, the higher the auto-ignition resistance of the fuel. Engine knocking occurs when

the air-fuel mixture is auto-ignited by the high temperature instead of by the ignition system, i.e. the spark plug.

The internal combustion engine has evolved in many different ways in the past century including, but not limited to, the fuel injection equipment and fueling strategy, ignition control, engine design and geometry, and metallurgy. These improvements have been made with the primary objectives of improving fuel efficiency and reducing harmful exhaust emissions.

In the passenger car segment, gasoline engines have typically dominated the North American market unlike Europe. For instance, diesel engine cars have maintained an approximately 50% share of the Western European passenger car market in the last twenty years [3]. This trend for diesel powered passenger cars in Western Europe is shown in Figure 1-1 from the year 1990 to 2016. A very rapid growth is shown from the year 1990 to 2016 with an increase of over 35% in diesel engine vehicles.

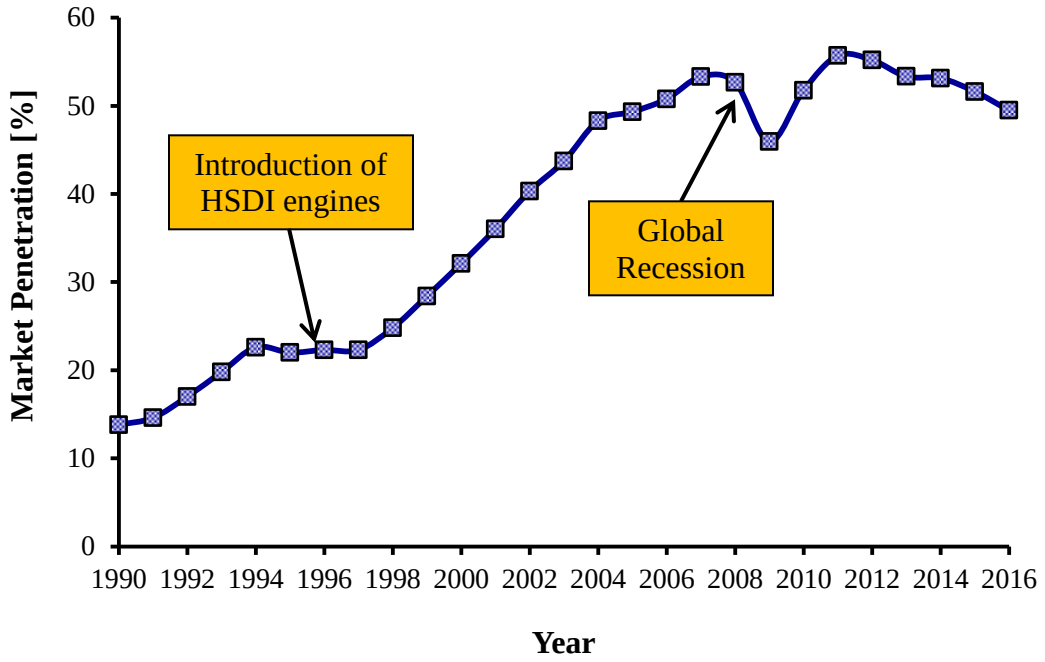

Figure 1-1: Diesel Engine Market Share in Passenger Cars – Western Europe [3]

In contrast, the diesel engine market in North America is mainly composed of medium and heavy-duty vehicles. This majority is shown by the data adapted from the United States Department of Transportation in Figure 1-2**.**

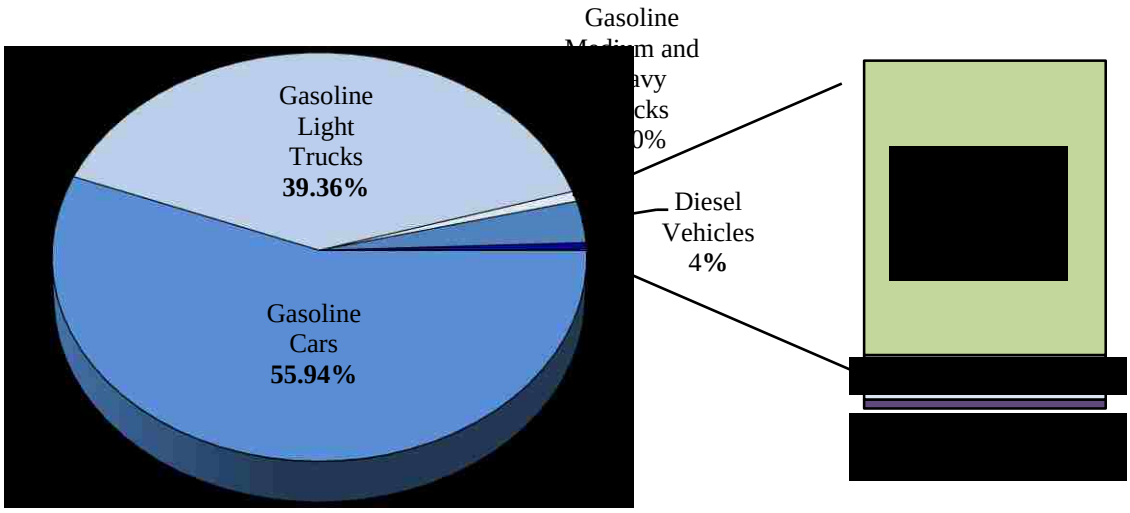

Figure 1-2: US Composition of Diesel and Non-Diesel Vehicle Fleet [6]

This data shows the registered on-road vehicle market share of 218 million vehicles total by engine type from 2014. Vehicles which are powered by gasoline engines occupy approximately 95.6% which equates to 201 million vehicles, the majority of which are gasoline powered passenger cars. Approximately 4% of the total vehicle market is comprised of diesel engine powered vehicles, the majority of which are medium and heavy-duty trucks. The diesel engine is an optimal choice for these applications due to better brake torque characteristics, durability, and fuel efficiency in comparison to gasoline engines.

The diesel engine market for passenger cars is substantially smaller in the U.S compared to Europe. One reason could be the significantly lower running cost of diesel engine cars in Europe compared with that of gasoline cars [4,5]. Recent international attention on the emissions of diesel engine powered passenger vehicles could also affect the growth of their market share. In the present scenario, the gasoline engine is expected to dominate the passenger cars and light duty trucks segment for the foreseeable future in North America until there is a shift in fuel prices and more vehicle options with diesel engines become available.

1.2 Current Emission Standards

In the late 1960's and early 1970's, the California Air Resources Board (CARB) and the United States Environmental Protection Agency (US EPA) were created. These were the first governing bodies which set the limits of air pollutants from the exhaust emissions of mobile sources (vehicles) into the atmosphere following the amendments made to the Clean Air Act (CAA) of 1970. These bodies were created due to the increased concerns about public health and environmental sustainability which arose in California due to the severe smog pollution and the energy crisis in the 1970's. Commonly regulated exhaust emissions from internal combustion engines are Nitrogen Oxides (NOx), particulate matter (PM), carbon monoxide (CO), and unburnt hydrocarbons (UHCs). Additionally, greenhouse gases (GHG's) such as carbon dioxide (CO_2) are regulated through fuel efficiency standards. The automotive exhaust emissions have been proven to cause severe health and environmental effects [7]. Therefore, CARB and EPA bodies have set increasingly stringent emission regulations in the past two

decades for both gasoline and diesel powered vehicles. The implementation of emission control equipment, such as three-way catalytic converters (TWCC) for gasoline engines and most recently selective catalytic reduction (SCR) systems for diesel engines, have assisted in meeting these regulations. The gasoline passenger car and light duty vehicle emission standards are shown below in Table 1-1 [9].

Table 1-1: U.S EPA Exhaust Emission Standards for Passenger Cars and Light Duty Vehicles up to 3856 kg (8500 lbs) [9]

Legislation	**Category/ Bin #**	**NMOG+ NOx [g/mile]**	**NMOG/ NMHC [g/mile]**	**CO [g/mile]**	**NO_x [g/mile]**	**PM [g/mile]**	**HCHO [g/mile]**
Tier 1 (1994-1997)	Passenger Cars	-	0.25	3.4	0.4	-	-
Tier 2 (2004-2009)	Bin 5	0.125	0.075	3.4	0.05	-	0.015
Tier 3 (2017-2025)	Bin 30	0.03	-	1	-	0.003	0.004

The emission limits are measured over a standard driving cycle when the vehicle is mounted on a chassis dynamometer. Three driving cycles exist; the Federal Test Procedure (FTP 75), the Supplemental FTP US06 and the SFTP SC03. The FTP 75 is the standard driving cycle used to evaluate the vehicle's emissions and is approximately 30 minutes in duration. The driving cycle simulates a distance of ~17 kilometers (km) which include three phases: a cold start phase, a stabilized phase, and a hot start phase [9]. The SFTP US06 was developed in 2008 to account for high acceleration and aggressive driving following engine start-up. The SFTP SC03 is another test which was adopted in

2008 that requires the air conditioning inside the vehicle to be turned on, attributing to engine load, while the exterior temperature is maintained at 95°F [9].

Tier 2 emission standards were more stringent than Tier 1, mandating an 87% reduction in NO_x. Additional changes in the Tier 2 regulations made the standards more stringent for larger vehicles. Passenger cars, vans, trucks, and sport utility vehicles (SUV) were required to meet the same criteria as passenger cars. The Tier 3 standards commissioned a 76% reduction in the combined non-methane organic gases (NMOG) and NO_x (0.125 – 0.03 g/mile) as well as a 70% reduction in carbon monoxide emissions (3.4 – 1 g/mile).

In addition to automotive manufacturers' striving to meet the emission standards, they also must consider the vehicle's fuel efficiency as well. The Corporate Average Fuel Economy (CAFE) standards were first introduced in the CAA by Congress in the 1975 Energy Policy and Conservation Act [10]. The act has set separate fuel economy targets for automakers' passenger car and light truck fleets since 1978. These regulations were established to reduce the energy consumption, and as a by-product, engine-out emissions, especially CO_2, was lowered since less fuel is combusted. The CAFE regulations require each manufacturer to meet specific fuel economy standards which are calculated by a sales based weighted average for an entire fleet. An overview of the previous CAFE standards, as well as the future projected standards, are shown in Figure 1-3 from the year 1980 through 2025, obtained from the U.S Department of Transportation [8]. The earliest standard was set to double fuel economy from 13.6 to 27.5 miles per gallon (mpg) by 1985. The standard remained at 27.5 mpg until 2010. In 2007, a mandate was made to increase fuel efficiency by 40% by 2025 and that CO_2 be regarded as a pollutant and

regulated by the EPA. Since 2007, the EPA with the National Highway Traffic Safety Association (NHTSA) has set progressively strict fuel efficiency standards for both passenger cars and light duty trucks.

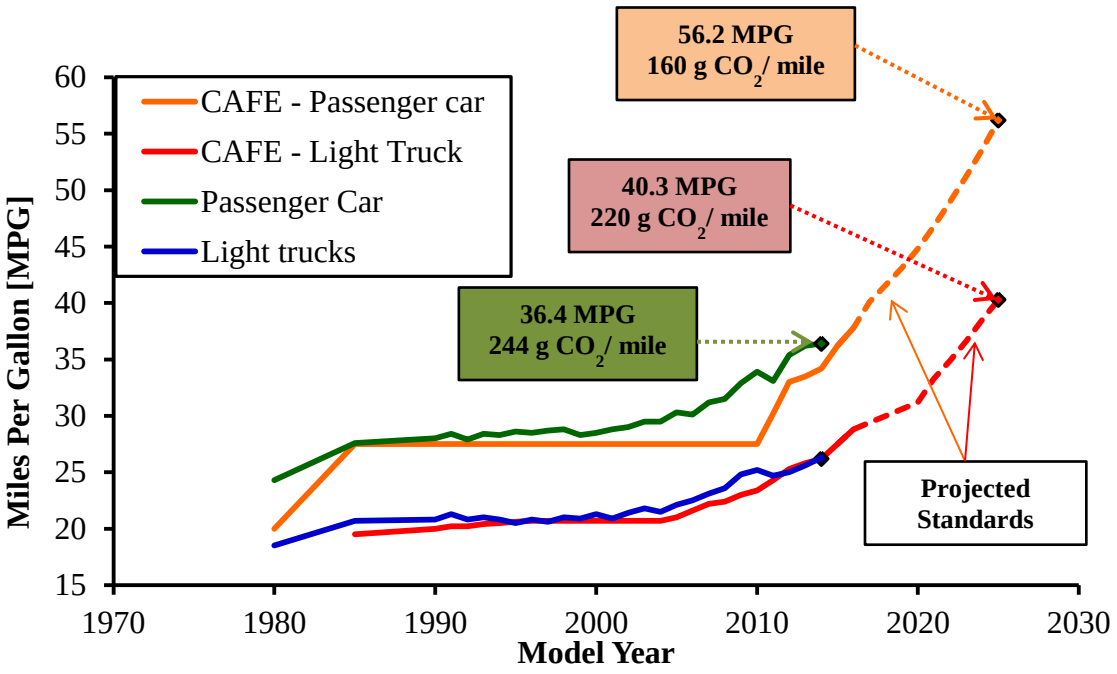

Figure 1-3: Historical Trend of U.S. Vehicle Fuel Economy and CAFE Standards [8]

The projected standards, for the model year 2025, require passenger cars to meet a fuel efficiency of 56 mpg or a CO_2 emission equivalent of 160 g/mile. That is a current increase in fuel efficiency of over 35% for passenger cars. The fuel efficiency standards for light duty trucks that include vans and sport utility vehicles (SUVs), are generally lower compared to the standards for passenger cars due to the increased vehicle size and weight. As shown above, the trend of actual passenger car fuel efficiency had been relatively higher than the standard limits, more so than light trucks. The offset is

attributed to the fact that the power requirement is much less for passenger cars and they have benefitted from engine downsizing and reductions in vehicle weight. Engine downsizing is one possible pathway to reach increased fuel efficiency because the overall displacement of the engine is decreased and the can potentially lower the throttling losses at partial loads. Fuel efficiency can also be increased by selecting lightweight materials for various components. This is quite common in modern vehicles today through the use aluminum body panels rather than steel. However, further development and different strategies must be investigated to meet these projected future regulations.

1.3 Thermal Efficiency of Spark Ignition Engines

The improvement of the thermal efficiency of an internal combustion engine is an effective method for reducing fuel consumption. The theoretical thermal efficiency of a spark ignition (SI) gasoline engine can be estimated using Equation 1-1, the efficiency of the Otto cycle:

$$\eta_{th} = 1 - \left(\frac{1}{r_c}\right)^{\gamma-1} \tag{1.1}$$

$$\gamma = \frac{C_p}{C_v} \tag{1.2}$$

where r_c is the compression ratio, γ is the ratio of specific heats, C_p [kJ/kg K] and C_v [kJ/kg K] are the specific heat at constant pressure and constant volume respectively of the working fluid.

Equation 1-1 shows that if the compression ratio were increased, a greater efficiency could be achieved. However, the compression ratio of current gasoline engines is limited for proper operations due to the ability of gasoline to auto-ignite easily under high temperature and pressure conditions. This auto ignition includes knock and pre-ignition combustion. Knock is undesirable because the auto-ignition of the mixture is unpredictable and can occur before the ignition of a spark plug, or before the arrival of the flame front. This pre-ignition can take place before the optimal crank positioning, reducing the efficiency and increasing the maximum in-cylinder pressure. The pre-ignition of the air/fuel mixture can also cause damage to engine components and can lead to engine failure [11].

The efficiency of the gasoline SI engine has slowly increased in the last 50 years through the development of different components and combustion strategies. Figure 1-4 shows the historical trend of SI engine's thermal efficiency.

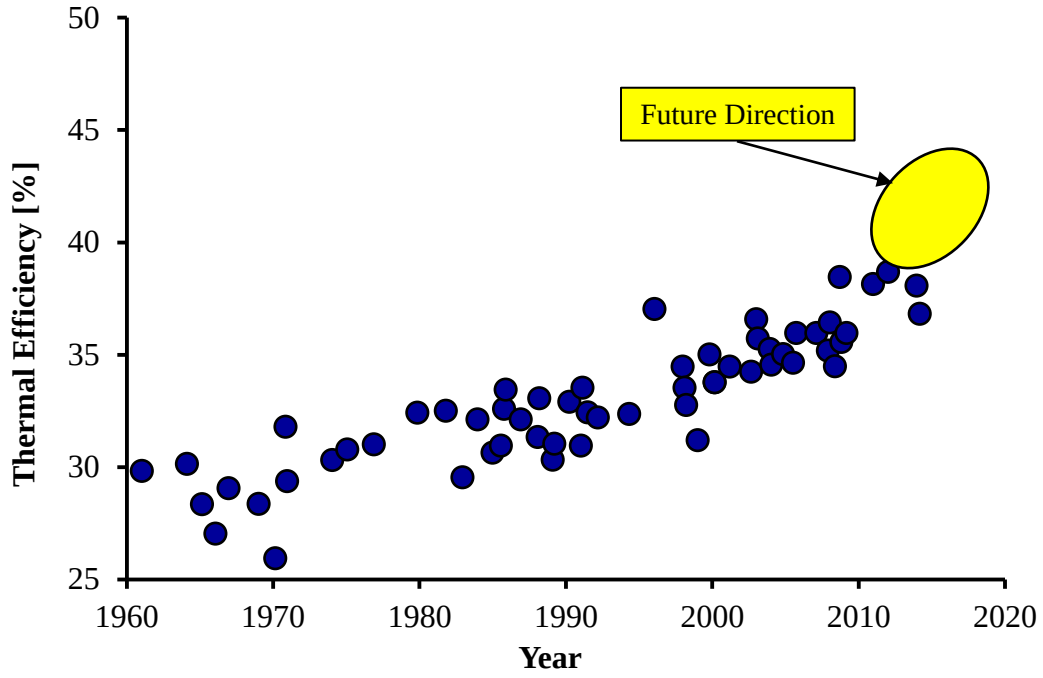

Figure 1-4: Historical Trend and Future Projection of Gasoline Spark Ignition Engines, Adapted from [12]

Current production gasoline engines have an efficiency of approximately 30-35% at full load. The trend shows that the thermal efficiency of the gasoline engine will only increase in the future years, driven by the increasingly stringent emission regulations and environmental sustainability.

1.4 Lean or Diluted Combustion

An effective method for increasing the efficiency of a gasoline SI engine is to use a lean or diluted the cylinder charge. Lean or diluted cylinder charges can assist in lowering the throttling losses incurred from the throttle body. Lean-burn or dilution can be accomplished by either increasing the amount of intake air inside the cylinder by increasing the opening of the throttle valve leaning the air-fuel mixture, or by using

exhaust gas recirculation (EGR). External EGR is a process where the exhaust gas of the previous engine cycle is routed back into the intake manifold and reused for the engine cycles to follow. Internal EGR is achieved mainly through the timing of the intake and exhaust valves. When the exhaust valve is kept open during the intake stroke, some exhaust gas is drawn back into the cylinder due to the negative pressure inside the cylinder. However, to have control of the amount of internal EGR, the exhaust cam profile must be completely variable [31]. This is a complicated task, and for that reason, external EGR has become widely adopted on modern engines. Two different external EGR loops, high and low pressure are shown in Figure 1-5 for a SI engine.

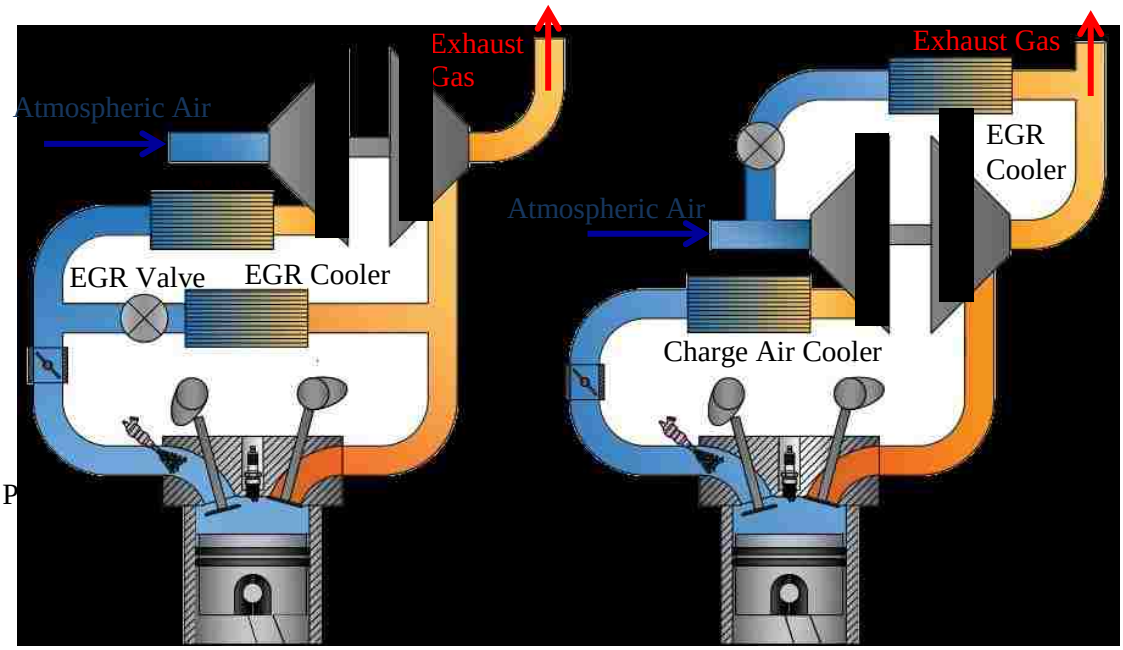

Figure 1-5: Schematic of High (a) and Low Pressure (b) EGR Loops for SI Engines

The application of EGR in port fuel injected (PFI) SI engines is used to reduce fuel consumption and reduce NO_x emissions [31]. Fuel consumption is reduced by

diluting the cylinder charge with exhaust gases, thus allowing a larger throttle opening for the same power and torque output which consequently reduces pumping/throttling losses. NO_x emissions are reduced due to the lowered in-cylinder combustion temperatures and the reduced concentration of oxygen available to oxidize with nitrogen.

Another method is to allow more air into the cylinder than would be required for stoichiometric combustion. This combustion concept is also referred to as lean-burn. As the air/fuel ratio increases, the overall charge becomes leaner than stoichiometric conditions. This method is quite effective in reducing fuel consumption because the throttle body is opened further to allow more air in the cylinder reducing the pressure drop. Furthermore, with the increased amount of excess air, the ratio of specific heats (γ) is increased due to the change in the cylinder charge composition [13]. An increase in efficiency is evident from Equation 1-1 with an increase in γ. In theory, the higher the level of dilution applied, the larger the increase in efficiency. However, in practice, the combustion of diluted mixtures is difficult due to the suppressed reactivity of the mixture [1,16].

Emission levels are also reduced when air dilution is applied. Dilution lowers the combustion temperature, since less fuel is combusted, which directly affects the formation of NO_x. In addition, the hydrocarbon (HC) emissions are lowered due to the increased amount of oxygen available for the oxidation of the fuel. A typical emission trend, adapted from [1], for a conventional SI engine is shown in Figure 1-6 with varying air/fuel ratio.

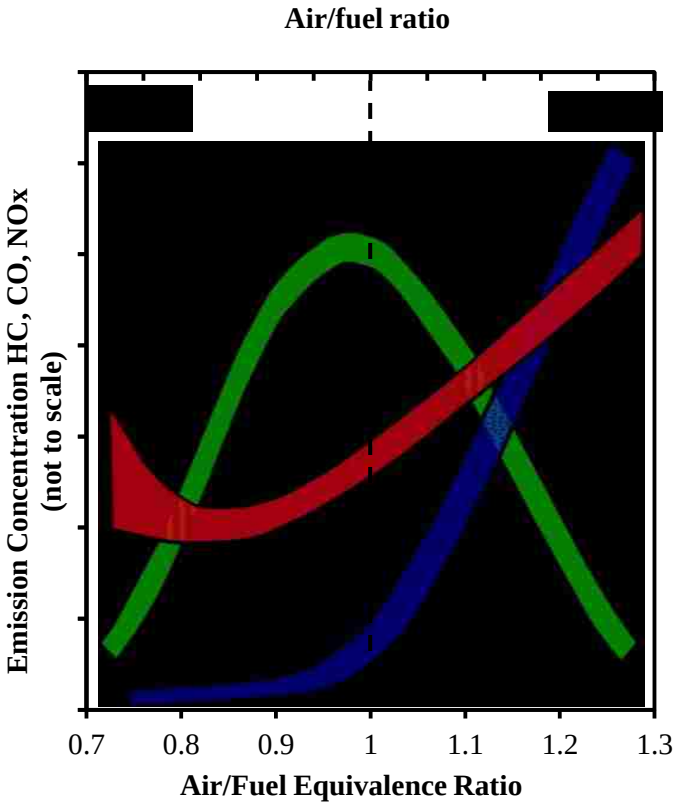

Figure 1-6: Variations of Emissions of Conventional Spark Ignition Engines with Varying Equivalence Ratio, Adapted from [1]

In practice, the combustion of diluted or excessively lean mixtures is difficult due to the suppressed reactivity of the mixture. In addition, the flame propagation speed is also slower [16]. Research has shown that increased dilution directly decreases the laminar flame speed [16]. The decrease in the flame speed can cause significant cycle-to-cycle variations which are undesired since this directly affects drivability of a vehicle [1]. It is also probable that the flame speed can become slow enough to the point that the combustion of the fuel is incomplete by the time the exhaust valve opens. At this point, the remaining UHCs are exhausted thereby reducing efficiency and increasing emissions. As the excess air or dilution level in the cylinder is further extended, the misfire limit is

reached at which the mixture fails to ignite. This increases the occurrence of misfires and reduces efficiency, increases UHC emissions, and produces large torque variations and roughness in engine operation.

To overcome the deteriorated ignitability of the diluted or lean mixture, some researchers have compensated by introducing increased amounts of spark energy from the ignition system as well as using a different type of ignition system [27,28]. The increased ignition energy and volume of ignition have proven effective in increasing the operable range of diluted combustion. Additionally, the period between when the command signal is given to the spark plug, and the combustion of the mixture begins, defined as the ignition delay, can be shortened using increased ignition energy or multiple ignition sites (two spark plugs). These ignition strategies have improved the control of combustion phasing which directly contributes to the efficiency increase.

Another strategy used to accelerate the flame speed and shorten the combustion duration is to enhance the charge air motion during the engine intake. This is typically accomplished through the design of the intake ports. Charge air motion controls the mixing and homogeneity of the air-fuel mixture. It also affects the in-cylinder turbulence during combustion, which subsequently affects the flame propagation speed.

1.5 Charge Air Motion – Swirl

It is well established that the air and fuel mixing process in SI engines is one of the most significant elements governing the combustion process and as a result, the engine performance and engine-out emissions. The in-cylinder air motion structure is predominantly dependent on the geometry of the intake ports [1,16]. The intake ports can

be helical shaped or placed tangentially along the cylinder in which air is ejected along the cylinder wall creating an organized rotation of charge about the cylinder axis. This organized rotation about the cylinder axis is defined as swirl motion which is shown in Figure 1-7.

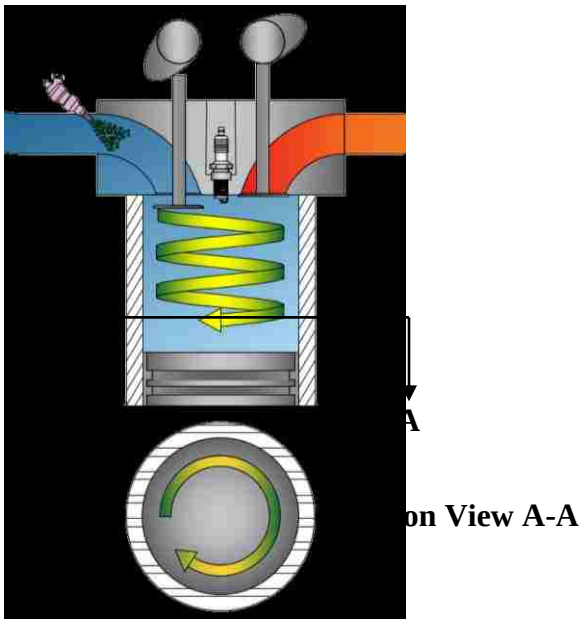

Figure 1-7: Swirl Charge Air Motion – Rotation about Cylinder Axis

Swirl motion is commonly used in direct injection (DI) engines to promote the mixing of the fuel spray with intake charge. Typically, a multi-hole injector is used for the injection of fuel into the cylinder. The swirling motion of intake charge passes through the fuel plumes to promote the mixing process. The swirl motion, depending on the strength, is initiated during the intake stroke, continued to the compression stroke, and can persist through the power stroke even to the exhaust stroke. The charge motion assists the burning and oxidation of any hydrocarbons remaining in the combustion chamber when oxygen reserve is avaliable. This lowers HC emissions and increases the combustion efficiency.

Swirl motion can also be used in port fuel injection (PFI) engines and DI SI engines to enhance the combustion process. The presence of swirl motion increases the turbulence, which hastens the combustion process by increasing the flame speed. Turbulence is generated by viscous shear forces between fluid motions. Turbulence can be increased when the piston is on the compression stroke, from the moving geometry of the piston in a combustion chamber. Turbulence present during ignition wrinkles the flame front (turbulent flame front). This wrinkling effect essentially increases the surface area of the flame front which is responsible for increasing the flame speed. This phenomenon is depicted in Figure 1-8.

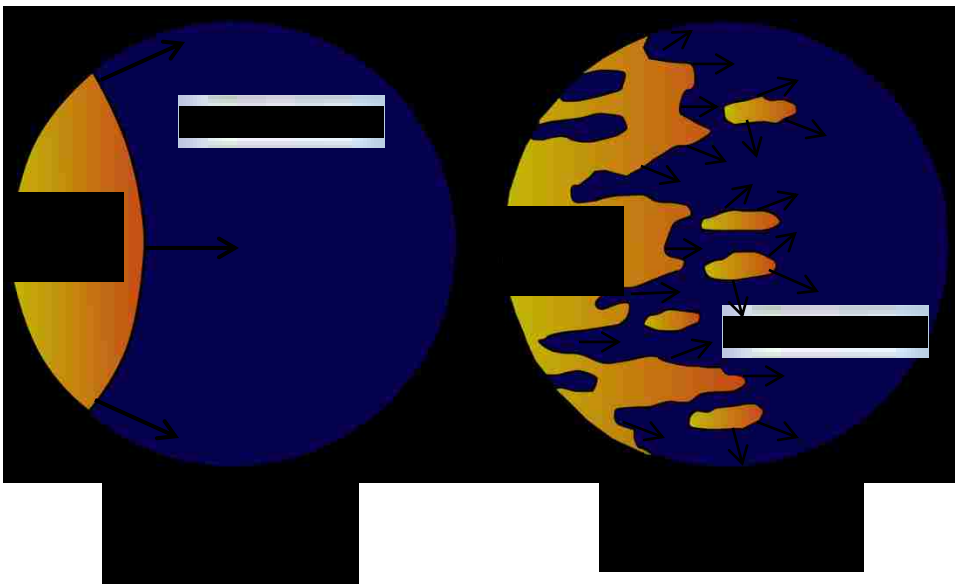

Figure 1-8: Comparison between Laminar Flame (a) and Turbulent Flame (b), Adapted from [16]

Typically, a four valve engine (two intake and two exhaust valves) will have two different shaped intake ports. One intake port is straight, providing a direct path to the cylinder, while the other can be helically shaped. This helically shaped intake port is used

to give the incoming intake charge angular momentum which shapes the bulk motion. Different levels of swirl are attainable due to the ability to send the intake charge to either the direct or the helical port, or both.

Two valve CI engines (one intake and exhaust valve), often employ a helically shaped port for the development of swirl. In this arrangement, the magnitude of swirl and turbulence can only be varied by changing the intake valve lift and/or duration or by placing an obstruction before the port to give the incoming flow some asymmetry for momentum.

1.6 Objectives of this Research

The main objectives of this research are to develop a flow bench research platform, capable of characterizing flow performance and swirl production, investigate different methods of enhancing the swirl speed, and to experimentally study the effect of increased swirl motion on engine combustion performance. This was accomplished by steady flow testing with a research engine cylinder head, to first obtain a baseline measurement. The results of the baseline measurement were then used to calibrate a computational fluid dynamics (CFD) model developed. In this research, after a satisfactory correlation was observed, different intake manifold insert geometries were simulated to enhance the air motion. The geometry which produced the largest increase in swirl motion was fabricated. The fabricated insert was tested on the flow bench to confirm the enhancement of the swirl. Finally, engine tests were conducted to investigate the effect on combustion with and without the use of the new insert.

1.7 Thesis Structure

This thesis consists of 7 chapters, and the details of each chapter are illustrated in Figure 1-9. Chapter 1 provides a brief introduction to the gasoline spark ignition engine and shows the trend of emission standards including future projected standards. Different combustion strategies are introduced, and their respective limitations are addressed. The significance of charge air motion is established, explaining how swirling air motion can potentially benefit the combustion process and thereby increase efficiency and reduce emissions. The objectives of this research are outlined at the end of the chapter. Chapter 2 provides a detailed literature review regarding charge air motion. The research tools used for this thesis work are discussed in detail and shown schematically in Chapter 3.

The main body of this thesis is presented in Chapters 4-6. The results performed on the flow bench are discussed in Chapter 4. Chapter 5 presents the results obtained from the numerical simulations. A comparison is made between the swirl speeds obtained from flow bench tests and the CFD modeled swirl speeds. The latter part of this chapter discusses the methods used to enhance the swirl air motion, and the tests conducted on the flow bench with the selected intake geometry. The results from the engine tests are presented in Chapter 6. Finally, Chapter 7 summarizes the overall results and conclusions from Chapters 4-6; and recommendations for future studies are provided. Further information regarding the references, appendices, and a list of publications are also provided to end the thesis.

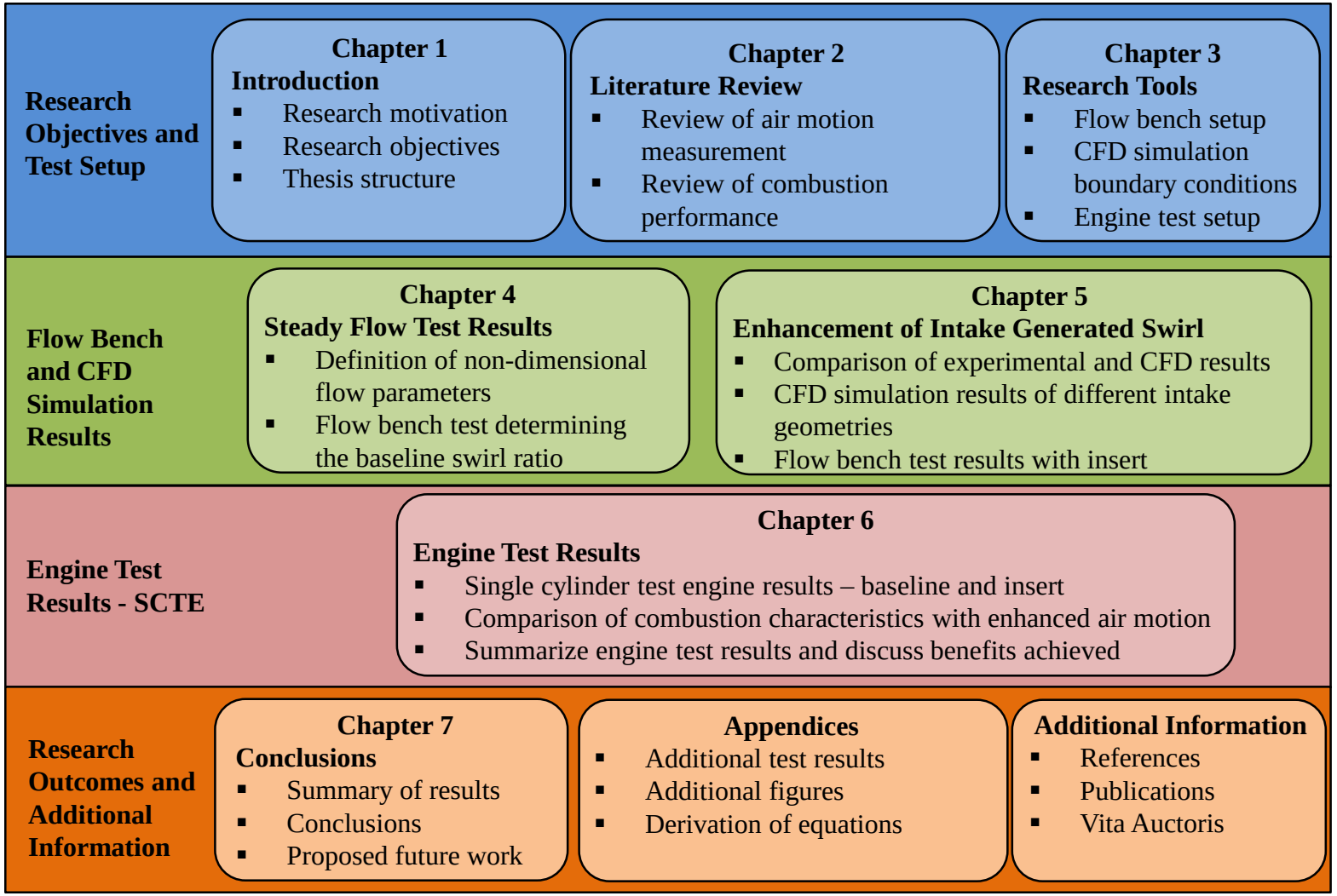

Figure 1-9: Thesis Structure Outline

CHAPTER 2: LITERATURE REVIEW

The in-cylinder charge air motion has proven to be effective to improve the combustion, and potentially the exhaust emissions [1,16,24]. With the increasingly stringent emission regulations and CAFE standards for fuel economy, the fuel-lean combustion may provide benefits over traditional stoichiometric combustion for SI engines. For these reasons, advanced combustion systems which utilize enhanced air motion to assist in increasing the burning rate are of interest to overcome the adverse effects of diluted combustion. This chapter provides a literature review on the measurement of charge air motion and the effect on combustion.

2.1 The Measurement of Swirl

The significance of charge air motion, and its influence on combustion, has been known for quite some time. Swirl was investigated in CI diesel engines as early as 1934 [17]. Alcock [17] investigated swirl motion by placing a rotating vane connected to a shaft inside the combustion chamber of a CI diesel engine. The shaft was sealed through the cylinder head using a sealing gland and allowed to rotate freely. The swirl speed was indicated mechanically by an external counting mechanism geared to the shaft. The engine was motored and the swirl speed was recorded. Another device, which contained only one vane, measured the torque exerted on the blade by the swirl. The swirl ratio was recorded while the engine was motored. Later, the swirl meter was removed and combustion tests were conducted. It was found that an optimal swirl ratio existed, the ratio of air swirl speed to the engine speed, which produced the largest brake mean

effective pressure (BMEP) and lowest brake specific fuel consumption (BSFC). A definite correlation between charge air motion and engine performance was presented.

Many researchers utilized the vane-type swirl meter for the measurement of swirl during steady flow tests [1,15,17-21]. The connection between steady flow tests and actual engine operation was made possible due to the flow characteristics common between the two. During engine operation, the intake flow is fully turbulent and since the flow experienced during flow bench tests is turbulent, the Reynolds numbers are similar [22, 29]. Since the Reynolds numbers are similar, non-dimensional flow parameters can be determined from steady flow bench tests since these parameters are independent of the mass flow rate and related to the flow during engine operation [22]. The vane-type swirl meter measures the swirl speed within the cylinder at each valve lift. The swirl ratio, which is a single metric for defining the air motion relative to the engine speed, is determined by obtaining the swirl speed at different values of valve lift from steady flow measurements. At the end of the induction process, the momentum is equal to the sum of the angular momentum experienced during the entire induction process [22, 29].

Another commonly used device for measuring swirl is the impulse-torque swirl meter originally proposed by Tipplemann in 1977 [23]. This device encompassed a flow straightening device, or a honeycomb core, which was used to arrest the angular momentum from the flow. The restraining torque required to arrest the swirl is measured by a reaction torque device and recorded at each valve lift. This type of device has been used quite often for the steady flow testing of cylinder heads in literature [15,19].

Heim at al [15] compared the performance of a vane-type swirl meter and an impulse-torque swirl meter. They conducted steady flow tests on two different cylinder

heads using both types of swirl meters. It was shown that the impulse-torque swirl meter produced a larger swirl coefficient relative to the value obtained from the vane-type swirl meter. The authors also devised a method of calibrating the swirl meters by inducing a known quantity of swirl into the cylinder and measuring it with both devices. It was found that the impulse-torque swirl meter responded better, obtaining a closer value to the known input. However, the authors used a flow straightener, a honeycomb shaped device, as the "paddle-wheel", and not the typical two-bladed vane style.

A similar trend had been observed by Kawashima et al [21] in 1998 for steady flow tests conducted with the vane- and impulse-torque type swirl meters. A four-valve engine was used which utilized a direct port and a helical port for the induction of intake charge to the cylinder. Different values of the swirl ratio were obtained by a swirl control valve, which was placed in front of the direct port. The position of the valve was changed to either allow or restrict the flow into this port. It was found that very small differences in the calculated swirl ratio were present between the two methods of measuring swirl at low swirl values. However, as the swirl ratio was increased above 2, it was found that the vane-type swirl meter produced lower swirl speeds resulting in a lowered swirl ratio than the swirl ratio obtained from the impulse-torque swirl meter.

Other non-intrusive methods of measuring swirl have been devised which include particle image velocimetry (PIV) and laser Doppler anemometry (LDA) measurements of the velocity field both on the flow bench and in motoring engines with optical access [16]. The main advantage of these types of measurement methods is that there is no artificial disturbance to the flow field, and more detailed information on the flow field can be extracted. However, the overall system complexity may be greater.

Nordgren et al [25] conducted in-cylinder flow experiments using PIV measurement in an optical engine and compared the results with CFD simulations. The CFD results were also compared with conventional steady flow test rig swirl measurements made with an impulse-torque swirl meter. The overall trend of the swirl speed development determined from the in-cylinder PIV experiments was in good agreement with the CFD results. A close agreement was noticed for the predicted swirl between the results of the CFD simulation and the impulse-torque swirl meter.

Wang et al [30] investigated the effect of variable valve lift on the production of in-cylinder air motion. An optical engine with PIV equipment was used to obtain velocity data while the engine was motored. The maximum intake valve lift was varied to obtain enhanced air motion within the cylinder. The swirl ratio was calculated by obtaining the tangential velocities of the seeding particles from the high-speed images. It was found that lowering the maximum intake valve lift increased the swirl ratio and air motion effectively, from measurements in different planes throughout the intake and compression stroke.

There are different methods used for the measurement of the air motion in internal combustion engines. Measurements which are conducted on a flow bench provide a fairly inexpensive and reliable method of measuring the in-cylinder air motion induced during induction, in comparison to the optical engine methods discussed [29].

2.2 **Effect of Diluted Combustion in SI Engines**

The application of EGR is an effective in-cylinder method to reduce the engine-out NOx emissions for SI combustion engines [31]. The other added benefit of the

application of EGR in SI engines is the reduction of throttling losses in the low to mid-range engine loads [1,32,33]. Throttling losses are created from the pressure differential across the throttle valve when the engine is operated in mid- to low-range loads. At these conditions, energy is consumed to draw charge air into the cylinder resulting in negative work from the engine cycle. The application of EGR assists to minimize these losses by allowing an increased opening of the throttle valve and diluting the cylinder with exhaust gasses from previous cycles [31]. Therefore, the engine load is maintained by fixing the fueling rate and managing the amount of available oxygen by controlling the amount of EGR dilution.

Cha et al. [32] studied the effect of EGR on combustion performance of a four cylinder port-injection gasoline engine. Standard engine test conditions from the Federal Test Procedure (FTP-75) were used and the baseline engine performance was measured. The EGR rate was increased until an acceptable level of engine cycle-to-cycle variation was exceeded. In this study and other literature, the acceptable level of engine cycle-to-cycle variation (COV_{IMEP}) was 10% [1]. It was found that the EGR reduced the NO_x emissions from 25% to 89% compared with the base engine results. The brake specific fuel consumption (BSFC) also decreased with the addition of EGR as the spark timing was advanced. It was also found that the burning rate and burned gas temperatures decreased.

Xie et al. [33] investigated the effect of hot EGR dilution on the combustion performance of a gasoline direct injection (GDI) engine. In this work, the exhaust gasses were not routed through a heat exchanger before being supplied to the intake. Similar in other researches, it was found that the BSFC and NO_x emissions were decreased while the

brake thermal efficiency increased with the application of EGR. At an EGR ratio of 20%, it was shown that the fuel savings reached 7% with a decrease in NO_x emission of 36% when compared with the base measurements at the same load conditions. In addition, the flame development time was increased and the flame speed was decreased, evident from the increase in combustion durations.

Alternatively, lean-burn combustion is another method of interest which has shown some benefit over EGR dilution. The lean-burn combustion strategy dilutes the cylinder charge with excess amounts of air which benefits the engine cycle efficiency by increasing the opening of the throttle valve thereby reducing the pumping losses of the engine.

Hacohen et al. [34] compared the combustion performance of lean-burn and EGR in a spark ignition engine. Different EGR dilution levels and equivalence ratios were investigated. It was found that at full load and wide open throttle (WOT) conditions, lean-burn combustion exhibited higher indicated thermal efficiencies at all equivalence ratios.

Lumsden et al. [35] investigated the possible advantages of lean-burn over EGR in a PFI four-cylinder gasoline engine. In both cases, the diluent mass was increased and the engine performance characteristics and emission data were compared. It was shown that the diluent mass ranges were extended for the lean-burn case, allowing higher levels of dilution over EGR. It was also proven that lean-burn operation could achieve lower BSFC at the same dilution level as EGR. When compared to lean-burn combustion, the EGR diluted combustion had lower NO_x but greater HC emissions.

More recently, Tang et al. [36] compared the combustion characteristics and performance of EGR and lean-burn in a four cylinder, port fuelled, 1.6L gasoline engine.

It was found that the indicated specific fuel consumption (ISFC) was reduced further for lean-burn combustion than the EGR diluted combustion, at low load conditions of 2 bar BMEP and an engine speed of 2000 rpm. The lean-burn combustion strategy also showed shorter combustion durations and higher combustion efficiencies for all levels of dilution compared with EGR. The advantage that the EGR dilution showed over lean-burn combustion was a lowered NO_x emission. However, the emission concentrations of hydrocarbons (HC) and carbon monoxide (CO) were consistently lower for the lean-burn combustion.

The lean-burn combustion strategy has shown potential for the increase in engine efficiency as well as the reduction of fuel consumption. However, the combustion duration is typically increased due to the lowered flame speeds. Lowered flame speeds have a profound effect on increasing the cycle-to-cycle variations [32,35,36], which essentially limits the amounts of excess air. However, to counter this phenomenon to increase efficiency, enhanced in-cylinder motion can increase turbulence levels which assist in the mixing of the charge, increasing the homogeneity, and possibly increase the flame speeds.

2.3 **Enhanced Swirl Motion in SI Engines**

In-cylinder turbulence plays a major role in increasing the flame speed during combustion in an engine. In addition, large scale air motion generated from the intake port geometry during the induction stroke increases the level of turbulence during the compression stroke. The turbulence present during ignition can assist in shortening the flame kernel development time and can increase the flame speed, consequently

shortening the combustion duration. This is advantageous for the thermal efficiency since a greater amount of heat can be released in a shorter period of time thereby increasing the work output of the cycle.

Whitelaw et al. [38] investigated the cyclic variations in a single cylinder research engine under lean-burn conditions with and without swirl. The optical engine provided access for LDV measurements to be made while the engine was motored to produce the high speed imaging of the air flow during operation. It was found that the turbulence intensity and mean flame speed were higher with swirl which resulted in an increased burning rate and higher in-cylinder pressures. The addition of swirl showed a decrease in the cycle-to-cycle variations in both load conditions. Overall, it was found that the combustion duration was reduced by 10-16% in the equivalence ratio range of 0.61 to 0.9, and the combustion stability was improved with swirl.

Matsuki et al. [39] explored the effect of swirl in a prototype lean-burn, four-cylinder engine for the improvement of fuel economy at low to medium engine loads. A lean mixture of $\lambda = 1.7$ was achieved with a swirl ratio of 2.5. This engine configuration was able to generate an approximate 40% increase in power output over the prior lean-burn model.

Hill et al. [37] also published a review on the effects of rotating flow on combustion in premixed spark ignition engines including the potential benefits of swirl. It is reported that swirl assists in increasing the turbulence intensity which increases the flame propagation speed and can result in a reduced burning duration and increased thermal efficiency, especially for combustion of lean mixtures.

2.4 **Chapter Summary**

The literature review highlighted the effect of dilution on combustion and discussed the positive effects on increasing the thermal efficiency and lowering engine-out emissions. The issues associated with both EGR and lean-burn combustion were presented, which included longer combustion duration as a result of lower flame speeds, increased cycle-to-cycle variations, and limitations on the amount of dilution before misfire is encountered. In addition, the advantages of lean-burn over the application of EGR were also addressed. The in-cylinder swirl charge air motion can assist in combatting some of these issues by increasing the mixing and turbulence. As a result, the objective for this research work was to investigate the effect of swirl on diluted combustion and investigate the effects on efficiency and emissions. The research equipment used for achieving this objective is presented in the following chapter.

CHAPTER 3: RESEARCH TOOLS

The research tools used in this study are described in this chapter. Details are provided for the flow bench system, the CFD simulation parameters, and the set-up of the engine test platform. These details, including the schematic diagrams of the equipment, include sensors and physical measurement devices. Further details are given in Appendices B-C for the in-house fabricated equipment. The descriptions of the research tools are given in the order in which they were applied to this research.

3.1 Steady State Air Flow Bench

All of the swirl measurements were conducted on an in-house designed and fabricated steady flow test bench. A schematic diagram of the flow bench test set-up is shown in Figure 3-1. The air flow is generated by four commercially available blower motors (Ametek Lamb 115923) which are powered by 120 V AC. Each blower has an independent power switch that enables the flexibility to set the desired amount of air flow by turning on a specific number of blowers. Details outlining the air box design and fabrication are shown in Appendix B. The air box is designed in such a way that it can create either a negative or positive pressure flow by physically rotating the air box and reversing the connections. In this way, both the intake and exhaust ports on an engine cylinder head could be tested and evaluated. However, only the intake port was of concern for this research, and the air box was only used to generate positive pressure flow.

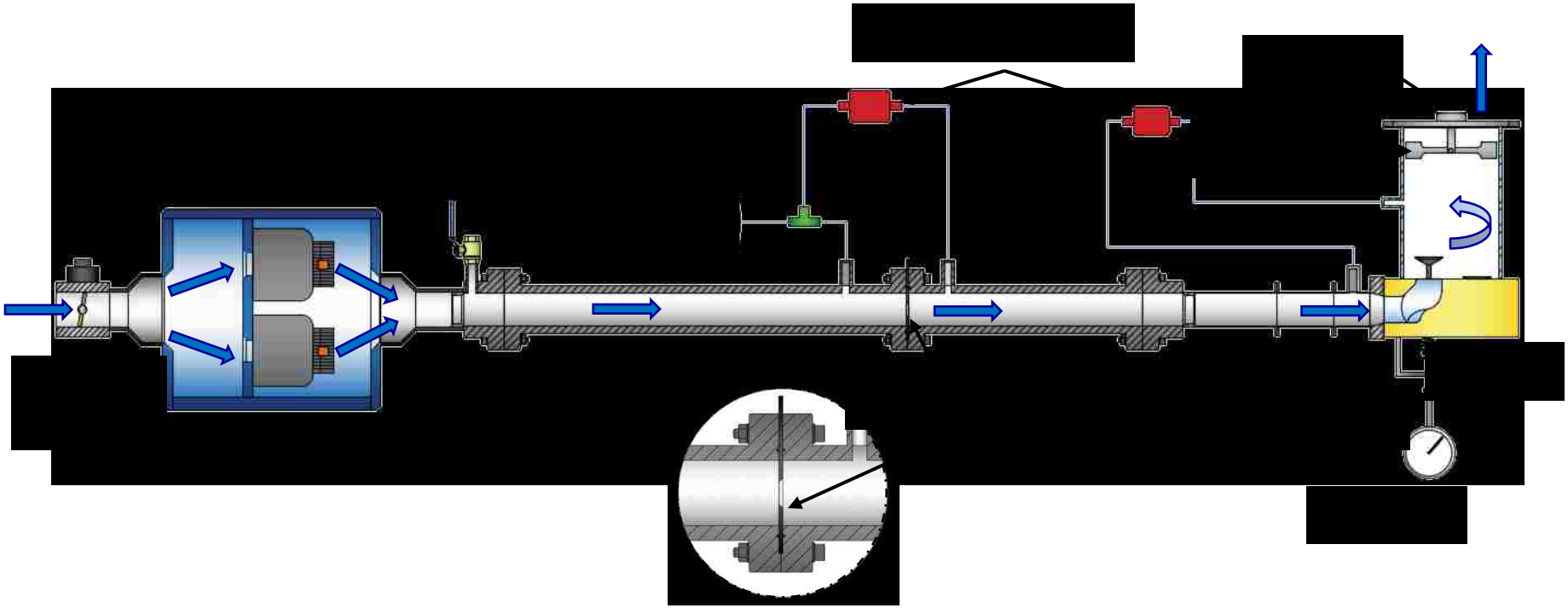

Figure 3-1: Schematic Diagram of Experimental Flow Bench Setup[1]

[1]Drawing is not to scale

The flow rate of the air generated from the air box was measured by an orifice flow meter. The sharp-edge orifice flow meter was designed and manufactured according to ISO 5167-1:2003 standards [41]. Details outlining the geometric dimensions of the orifice flow meter are provided in Table 3-1. The pressure difference across the orifice plate was measured and recorded using an NXP USA MXPV7025 digital differential pressure sensor. A U-tube manometer, which was filled with water with added colour dye, was utilized to provide a reference measurement in addition to the readings obtained from the differential pressure sensors. A correlation between both of the measurements was created to obtain a calibration function (details in Appendix A). An Ametek SPT0100X140 (0-100 psi) pressure transducer was incorporated in the upstream piping to indicate the upstream pressure of the orifice plate (p_1). This upstream pressure was required for the iterative calculation of the mass flow rate. A 28 mm orifice plate was inserted in the orifice flow meter due to its suitability to produce a desired range of pressure differences across the orifice, with a relatively high resolution with low pressure differences. The flow was directed to the intake port via a fabricated intake manifold which was attached to the cylinder head from a Yanmar NFD170 engine. The internal shape of the manifold was designed to transition from the circular cross-section of the pipe to the rectangular cross-section of the original intake port of the cylinder head.

Table 3-1: Orifice Flow Meter Specifications

Description	Unit	Value
Inside Diameter	mm	55.8
Upstream Length	mm	781.2
Downstream Length	mm	390.6
Pressure Tapping – Distance Upstream from Orifice	mm	55.8
Pressure Tapping – Distance Downstream from Orifice	mm	27.9

An additional differential pressure sensor was used to measure and record the pressure difference across the intake port. In this thesis, the pressure difference across the intake port is referred to as the test pressure. To the best of the author's knowledge, there is no global industry standard regarding the operating test pressure for such flow bench tests. However, it is understood that the pressure must be sufficient to produce turbulent flow (with a Reynolds number greater than 4000). This is required to replicate the induction of turbulent gas flow into the cylinder during the intake stroke in an operating engine [22,29].

The stock valve springs were replaced with soft springs. This was done to ease the effort required to depress the valve during steady flow tests. The retainers and keepers were utilized on the setup to ensure that the flow would not affect the valve lift. The intake valve lift was varied using a fine threaded bolt and a fixture to depress the valve and soft spring. The amount of valve lift was measured using a dial indicator, which was fixed into position on the fixture, with the plunger in contact with the head of the bolt. The resolution of the dial indicator was 0.001 inches or 0.0254 mm. The valve lift was varied at 0.5 mm increments. This resolution was deemed suitable for identifying trends in the swirl speeds and flow performance.

An acrylic cylinder, 4 inches or 101.6 mm inside diameter, was used as a surrogate that replaced the engine cylinder. The length of the cylinder and vertical positioning of the swirl meter was determined by calculating the time between the maximum intake valve lift and when the piston reaches TDC on the compression stroke. The equivalent length of the acrylic cylinder and axial position of the swirl meter were determined by calculating the time between the maximum intake valve lift and the piston reaching TDC on the compression stroke to the time required for a particle of air, during steady flow tests, to pass from the intake valve to the measurement location. The equivalent length of the cylinder was used to represent the equivalent time that the swirl would be affected by the skin friction from the cylinder wall [22]. This calculation resulted in a distance of 120 mm (1.18 times the cylinder bore).

An electronic throttle body was placed upstream of the air box to control the overall flow in the system. The throttle plate position was controlled by a LabVIEW 2010 based control program which was developed in-house. In addition to the throttle body, additional flow range adjustments were made via a ball valve placed upstream of the orifice plate in the orifice flow meter. This valve acted as an air bleeder, creating an alternative pathway for upstream air to exhaust to the ambient and allowed finer resolution adjustments to be made.

3.1.1 Swirl Meter

The device used to measure the speed of the rotational flow was an in-house built vane-type swirl meter. This type of swirl meter has been commonly used for the measurement of swirl in steady flow test benches and in engines for some time, as early

as 1934 [1, 15,17-21]. According to the literature, the vane-type swirl meter has also been placed inside the combustion chamber and implemented for the indication of the swirl speed during the motoring of a diesel engine [17].

Although commonly used, there is no well-established standard for the design parameters of the geometry of the blade of the swirl meter. The geometry of the blade and the design of the swirl meter used for this work is presented in Appendix D. A photo of the swirl meter is shown in Figure 3-2.

Figure 3-2: In-house Fabricated Vane-Type Swirl Meter

The components of the swirl meter were made from aluminum in comparison to steel, to reduce the inertia incurred during rotation of the device, which increases the accuracy of the swirl measurements. A CUI Inc AMT102-V capacitive encoder was mounted to the base of the swirl meter to determine the rotational speed of the vane. The encoder has an adjustable resolution from 48 – 2048 pulses per revolution when the rotational speed is below 75000 rpm. The negative or positive index signal feedback indicated the clockwise or counter clockwise direction of rotation respectively. The shaft was attached to the blade via a press fit pin. The shaft is supported by an NICE 1602-

DCTNTG18 ball bearing. In an effort to reduce friction in the bearing itself, between the inner and outer races, the dust shields of the bearing were removed. A groove, the same outer diameter and thickness as the acrylic cylinder, was machined in both the base plate of the swirl meter and cylinder head. This assisted in accurately locating the swirl meter on the acrylic cylinder and cylinder on the cylinder head in order to ensure that they were concentric.

3.1.2 Data Acquisition

The feedback electronic signals acquired from the pressure sensors, position sensor on the throttle body, and encoder were sampled by a National Instruments (NI) PCI-6229 Data Acquisition (DAQ) card. The flow was deemed to be steady when the real-time readings from the pressure sensors were stable. The in-house developed LabVIEW program was also used to record 500 data samples of the encoder signal through the DAQ card once the air flow was steady. The arithmetic mean of the sampled data is calculated and used to obtain the average swirl speed at each valve lift. The readings obtained from the pressure sensors are averaged in a similar manner.

3.2 Numerical Simulation

The numerical simulations were performed using Converge^{TM} Computational Fluid Dynamics (CFD) software. The software uses automatic grid meshing and user defined grid refinement features to increase the resolution and accuracy of the fluid velocity domains. CEI Ensight 10.1 was used for the post processing of the numerical results to provide visualization of the fluid motion.

Since the author does not have access to the original CAD design of the cylinder head and intake port, a polyurethane foam mold has been casted to duplicate the internal geometry of the intake port. The foam mold was made from Foam-iT® 5 series which is a two-part expandable foam. Due to the fact that the port is helically shaped, it was necessary to select a flexible mold in order for it to be retrieved without destruction. The mold was scanned using a three-dimensional scanner made by NextEngine at the University of Windsor, and a digital surface file was produced. This process was done to obtain a geometrically accurate model for the later simulations. Figure 3-3 below shows the molded geometry of the intake port (left) and the scanned model of the intake port (right).

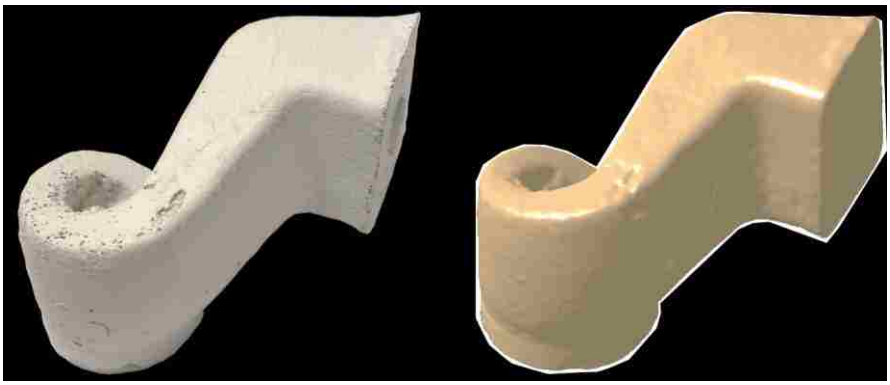

Figure 3-3: Molded and Scanned Intake Port Geometry

A model of the steady flow test bench was constructed for the CFD simulations. The model includes the intake manifold, upstream piping of the intake manifold, intake port geometry, cylinder head deck surface, intake and exhaust valves, as well as the cylinder. The mass flow rates recorded during the flow bench tests were used as inputs for the simulations. Similar to the test conditions, the valve lift in the numerical

simulations were set from 0.5 to 10.5 mm in 0.5 mm increments for a total of 21 different cases and deemed suitable for identifying trends in the swirl speed.

The numerical model had a base grid mesh consisting of 4 mm edge cubes to decrease the total simulation time. The grid was later refined in three steps during the simulation in defined areas to increase the resolution of the velocity and other parameters such as angular momentum, and moment of inertia by utilizing the fixed embedding feature. The simulation time was set to 15,000 seconds, which was determined through trials, for the flow to reach a steady state apparent by the convergence of the mass flow rate. The first 2,000 seconds of the simulation had a grid count of 2,000 cells which was then scaled for the next 1,000 seconds to 270,000 cells. From 3,000 to 7,000 seconds, the grid was scaled again producing a total of approximately 2 million cells. The final embedding occurred at 7,000 seconds where the total cell count was approximately 3.18 million. Figure 3-4 shows the complete numerical model and the boundaries. The areas where the mesh refinement was applied to are outlined in Figure 3-5. The coordinate system of the numerical model is orientated such that the center of the cylinder is $x = 0$ and $y = 0$; the top of the cylinder head, when looking from the open end of the cylinder, is $z = 0$ as depicted in Figure 3-4.

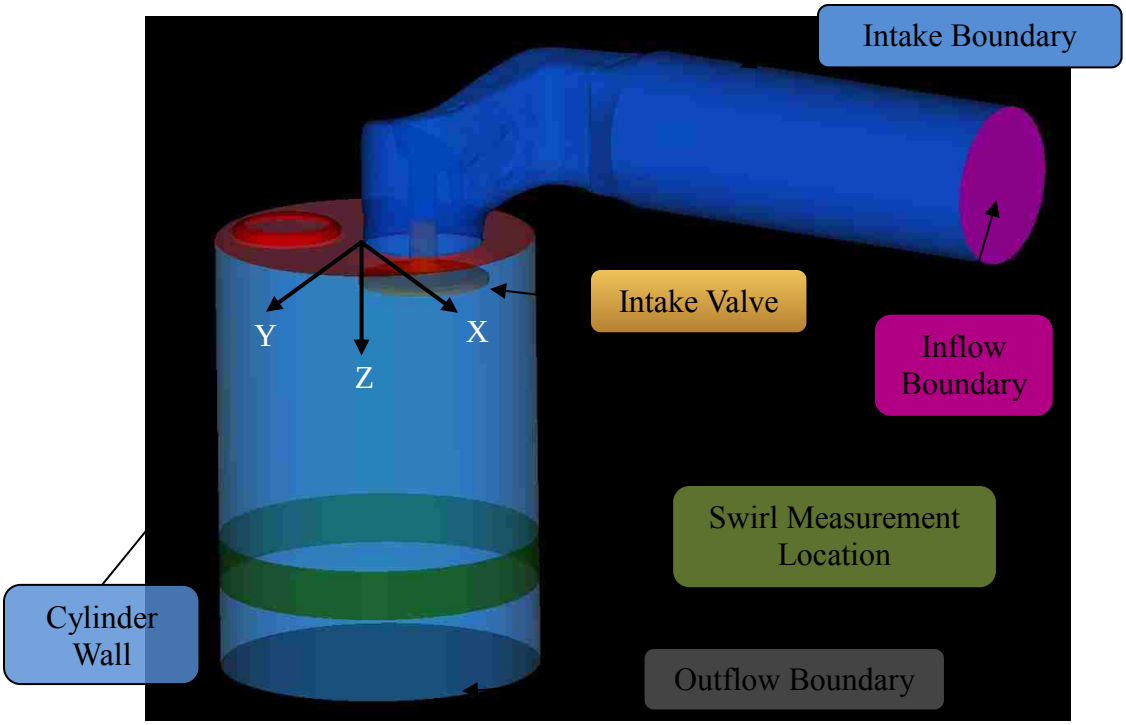

Figure 3-4: Numerical Model Boundaries

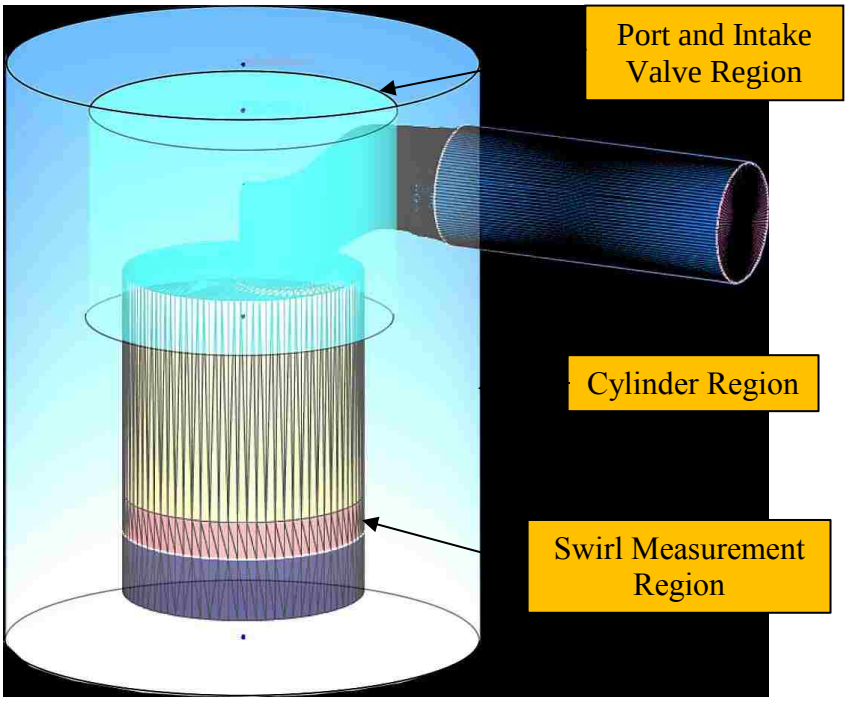

Figure 3-5: Numerical Model with Mesh Refinement Regions

The velocities in the valve lip area are, at times, larger than Mach 0.3 [16]. A density-based steady solver was used since this solver was recommended for flow simulations that experience Mach numbers greater than 0.3 [42]. The pressure-based solver is more efficient than the density-based solver when the Mach number is less than 0.3 [42].

A renormalized group theory (RNG) k-ε model was used to simulate the turbulence. This model is a two-transport-equation model which solves for the kinetic energy k and the turbulent dissipation ε. The RNG k-ε model differs from the original k-ε model in that it accounts for smaller scales of motion [43]. Also, this turbulence model is recommended for IC engine simulations when using Converge^{TM} [42]. Another factor contributing to the selection of the turbulence model was the available computing time and computing power.

3.3 Engine Test Set-up

The engine tests were carried out on a Yanmar NFD170 which is a four-stroke, single-cylinder, two-valve, direct-injection, stationary diesel engine. A Gurley optical encoder is mounted to the crankshaft and provides the information of the angular position of the crankshaft with a resolution up to 0.1°.

The engine has been modified to operate with gasoline port fuel injection and spark ignition. The original piston has been changed to lower the compression ratio for the spark ignition research. The engine was coupled to a General Electric DC motoring dynamometer, model: 26G215. The engine specifications are given in Table 3-2, and a schematic diagram is provided in Figure 3-6. In order to simulate boost, clean and dry

intake air was supplied from an oil-free compressor with desiccant filters. The air supply pressure was controlled by an electronic pressure regulator. A gate valve, placed upstream of the engine intake manifold, was used to throttle the intake air. The fuel injection duration, fuel injection timing, spark duration, and spark timing were controlled through a National Instruments (NI) Real Time – Field programmable Gate Array (RT-FPGA) controller. Further details of the subsystems of the test setup are given in the following sections.

Table 3-2: Engine Specifications of Yanmar Engine

Engine Parameter	**Unit**	**Value**
Displacement	[L]	0.857
Bore	[mm]	102
Stroke	[mm]	105
Connecting Rod Length	[mm]	165
Compression Ratio	[-]	13.1:1
Intake Valve Closing (IVC)	[CAD]	-135°ATDC
Exhaust Valve Opening (EVO)	[CAD]	45°BBDC
Combustion System	[-]	Port Fuel Injection
Fuel Injection System	[-]	External Pump
Injection Pressure	[Bar]	4

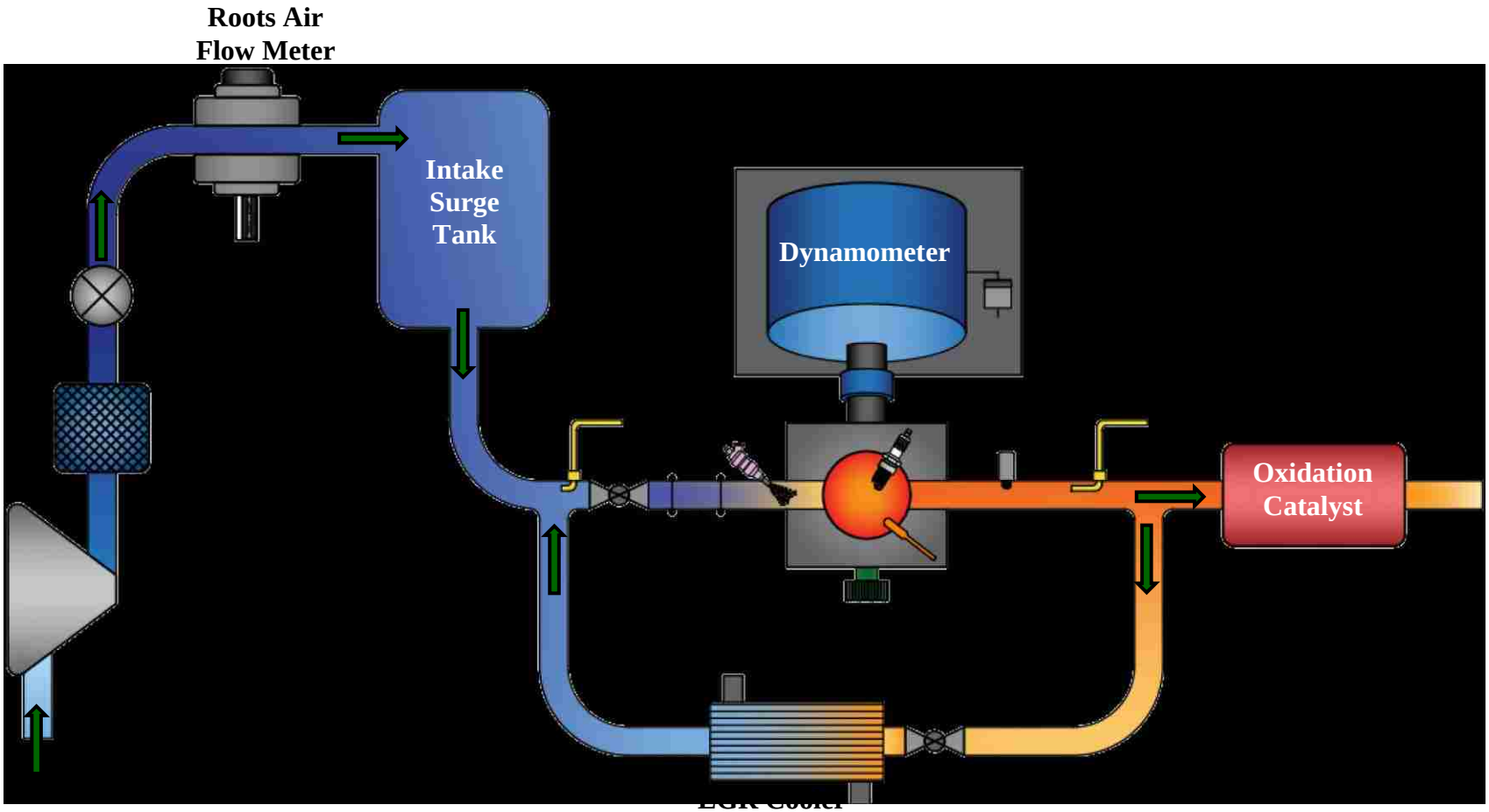

Figure 3-6: Schematic Diagram of the Single Cylinder Engine Used for Engine Test

3.3.1 Intake Air System

A new intake manifold was fabricated in-house to incorporate the port fuel injector. The fuel injector, a Bosch BR3E-E5A 36lb/hr, was placed at an inclined angle on the intake manifold to reduce the amount of liquid fuel impingement on the bottom of the intake port. The intake pressure was recorded using a Kistler piezoresistive pressure transducer, model: 4075A10. The recorded intake pressure was utilized for the pressure pegging of the in-cylinder pressure curve during the post data processing. The intake manifold had a removable insert holder section where different inserts, of various geometries, could be placed inside to modify the intake flow. The insert holder section is shown in Figure 3-7. Two V-band clamps were used to attach and seal the section with the intake manifold. The intake mass air flow measurement was recorded via a roots style air flow meter, (model 5M175) manufactured by ROOTS. The different levels of charge dilution were produced by changing the opening of the intake throttle valve while maintaining the same fuel flow rate and injection duration.

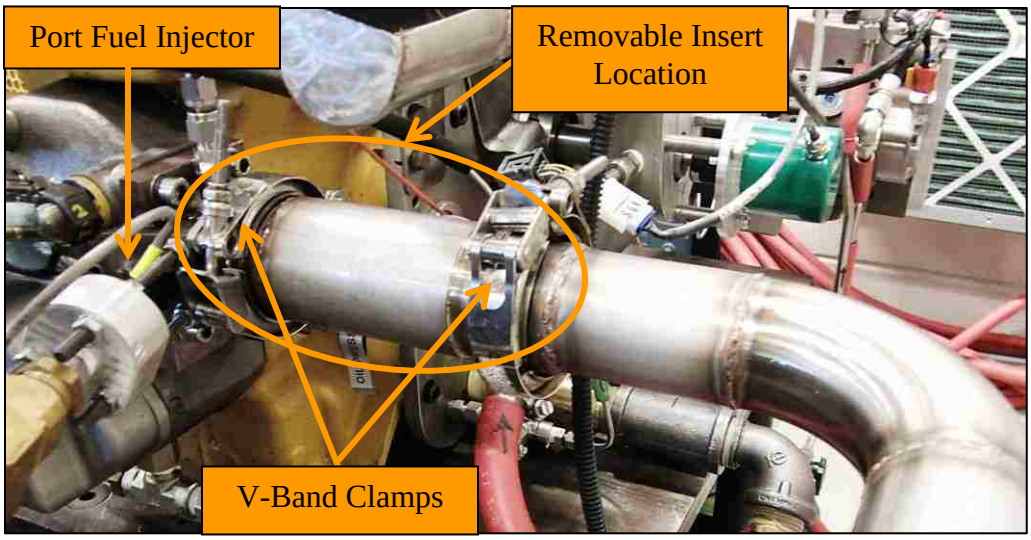

Figure 3-7: Removable Insert Location and Attachment

A patented three pole igniter is used to ignite the charge. More information regarding the three-pole igniter can be found in [27]. The igniter was mounted centrally on the engine cylinder head at the location where the former DI injector was located.

3.3.2 Fuel System

The fuelling system for the single cylinder test engine is shown in Figure 3-8. The fuel was supplied from an external fuel cell unit using a low-pressure in-line fuel pump. The fuel was pressurized to 4 bar and maintained at this pressure during the engine tests. The excess fuel was pumped through a heat exchanger before it was returned to the fuel tank to control the temperature of fuel and remove any heat added by the pump. After the pressure regulator, the fuel was plumbed through a 5 μm fuel filter to remove impurities. After the filter, the fuel was pumped to the injector via a flexible braided stainless steel line. A piston-type fuel flow meter (Ono Sokki FP-213) was used to determine the fuel

flow rate during the experiments so adjustments could be made to obtain the desired fuel flow rate. The fuel used for the engine tests was gasoline with a pump octane number of 89.

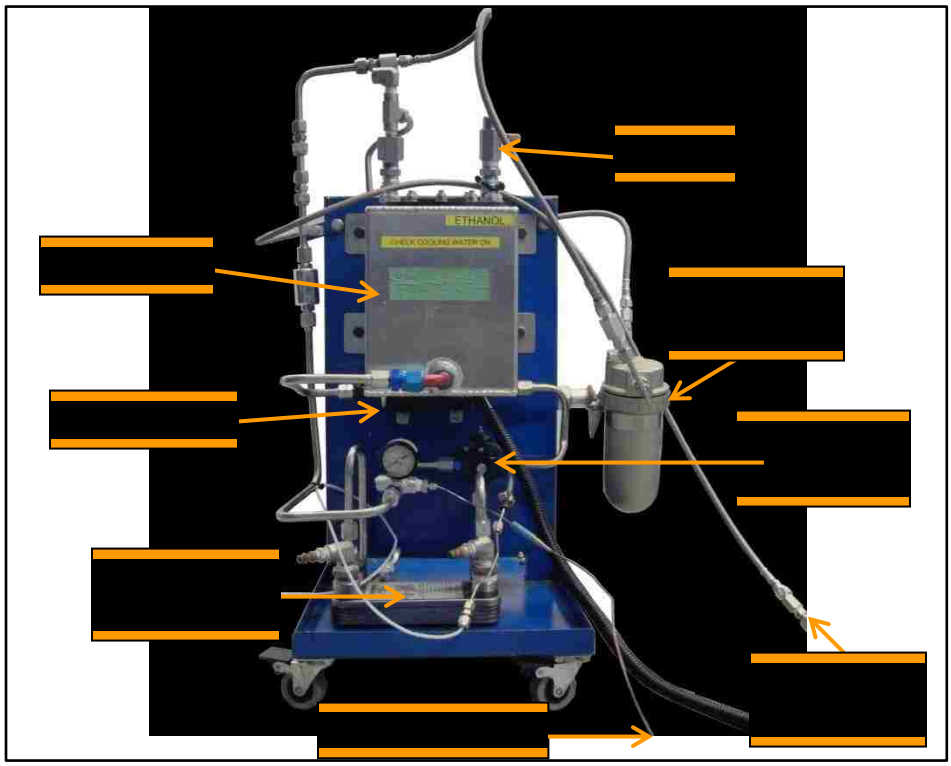

Figure 3-8: External Fuel Supply System for the Engine Tests

3.3.3 Cylinder Pressure Acquisition and Processing

The in-cylinder pressure was recorded for 200 consecutive engine cycles at each operating condition. The purpose of averaging 200 consecutive cycles was to ensure, with a 99.9% confidence interval limit, that the population mean differed from the sample mean by no more than 3% [46,47]. The pressure sensor for in-cylinder pressure recording was a piezo-electric pressure transducer from Kistler, model 6043A60. The signal from

the pressure transducer was sent to a Kistler charge amplifier, model 5010B, for the conditioning of the signal. The conditioned pressure signal was recorded by both a NI DAQ (PCI-6229) and a NI PXI RT-FPGA setup. More information regarding the single-cylinder engine set-up can be found in [26].

3.3.4 Emission Analyzers

The intake gases were sampled downstream of the EGR loop and the exhaust gasses were sampled upstream of the EGR loop, shown in the schematic diagram in Figure 3-6. The gases were supplied to different emission analyzers to determine the composition of the gas mixture. A gas conditioning unit was installed prior to the emission analyzers for the purpose of removing water from the sampling line via a chiller. A paper filter was installed which removed any solid particulates from the sampled gas. A list of the emission analyzers and their respective model numbers is provided in Table 3-3.

The intake sample gas was plumbed to a Non-Dispersive Infra-Red (NDIR) and Paramagnetic Oxygen analyzer for the measurement of carbon dioxide and oxygen respectively. The applied EGR ratio was determined by the measurements of O_2 and CO_2 from the intake gas sampling. The exhaust gasses were also routed to another NDIR-Paramagnetic analyzer unit to determine the O_2, CO_2, and CO concentrations to separate it from the intake gases. A Chemiluminescence detector was used to measure the NOx emissions. The Hydrocarbon emissions were measured by a Heated Flame Ionization Detector (FID). Figure 3-9 shows the dual bank CAI emission analyzers. A Ford Motor Company oxygen sensor, model 8F9A-9Y460, was placed in the exhaust manifold

downstream of the exhaust valve. The oxygen sensor was used mainly as an indicator of the in-cylinder air-to-fuel ratio during the experiments. The air-fuel ratios were later calculated based on the mass air flow and fuel flow rates.

Table 3-3: Emission Analyzer System Details

Measurement Type	**Species**	**Range**	**Model**
Non-Dispersive Infra-Red (NDIR)	CO_2	0-2% & 0-10%	CAI 602P
	O_2	0-25%	
Chemiluminescence	NO_x	0-3000 ppmV	CAI 600 HCLD
Heated Flame Ionization Detector	THC	0-3000 ppmV	CAI 300M-HFID

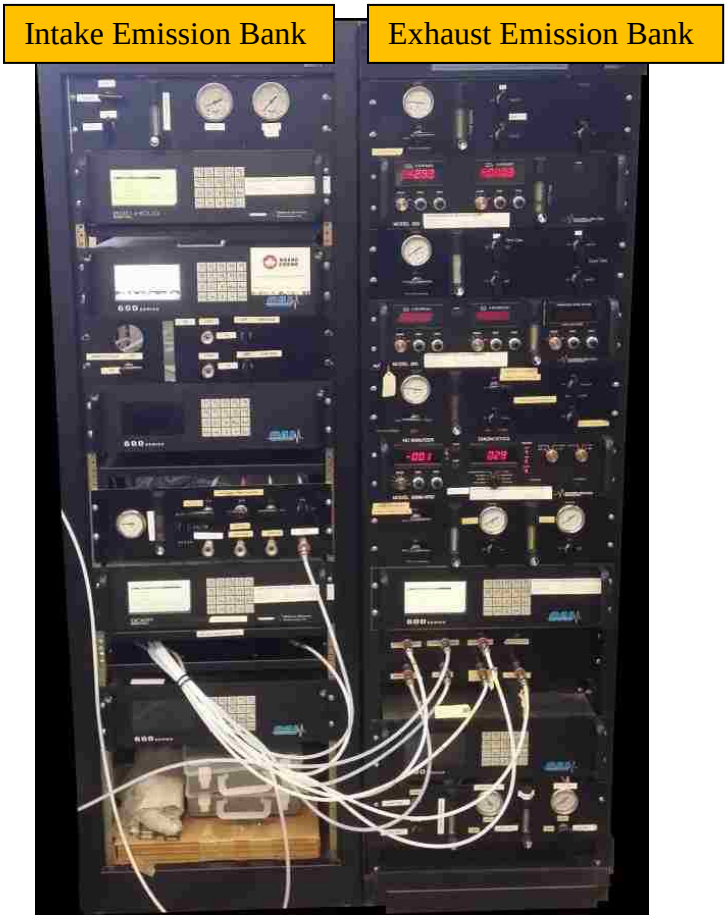

Figure 3-9: Intake and Exhaust Emission Analyzer Bank for Emission Measurement

CHAPTER 4: STEADY FLOW TEST BENCH RESULTS

` In this chapter, the steady flow bench tests performed with the cylinder head are described. The purpose of these tests was to obtain a baseline measurement of the flow characteristics of the stock cylinder head. In addition, the non-dimensional flow parameters are introduced and defined in this chapter, which were then used for the evaluation of the flow performance. The experimental data collected during these tests were thereafter used as boundary inputs for the CFD model in Chapter 5. Finally, the baseline intake generated swirl ratio was determined.

4.1 Introduction

To obtain the baseline intake flow parameters of the engine cylinder head, tests were conducted on the steady flow bench discussed in section 3.1. The flow inside of the intake port of an engine in operation had been measured in previous studies and was found to be fully developed turbulent flow [29]. Therefore, to obtain the intake flow parameters that were relatable to an engine in operation, the flow rate during flow bench tests must be set to ensure that fully developed turbulent flow is present. This was verified by calculating the Reynolds number of the flow in the intake port, valve, and cylinder. Turbulent flow produces a Reynolds number of greater than 4000. The Reynolds number was calculated using Equation 4.1:

$$Re = \frac{\rho V d}{\mu} \tag{4.1}$$

where ρ is the air density [kg/m^3], V is the average flow velocity [m/s], d is the diameter of the pipe [m], and μ is the dynamic viscosity [kg/m·s].

In order to test the cylinder head on the flow bench, the maximum intake valve lift must be known. For this reason, the intake and exhaust cam profiles were measured on the engine. The valve cover was removed, and a dial indicator was placed in line with the push rod in contact with the rocker arm. The engine was rotated while the signal from the encoder (resolution of 0.01° CA) indicated the relative crank position. The intake and exhaust profiles that were measured are shown in Figure 4-1.

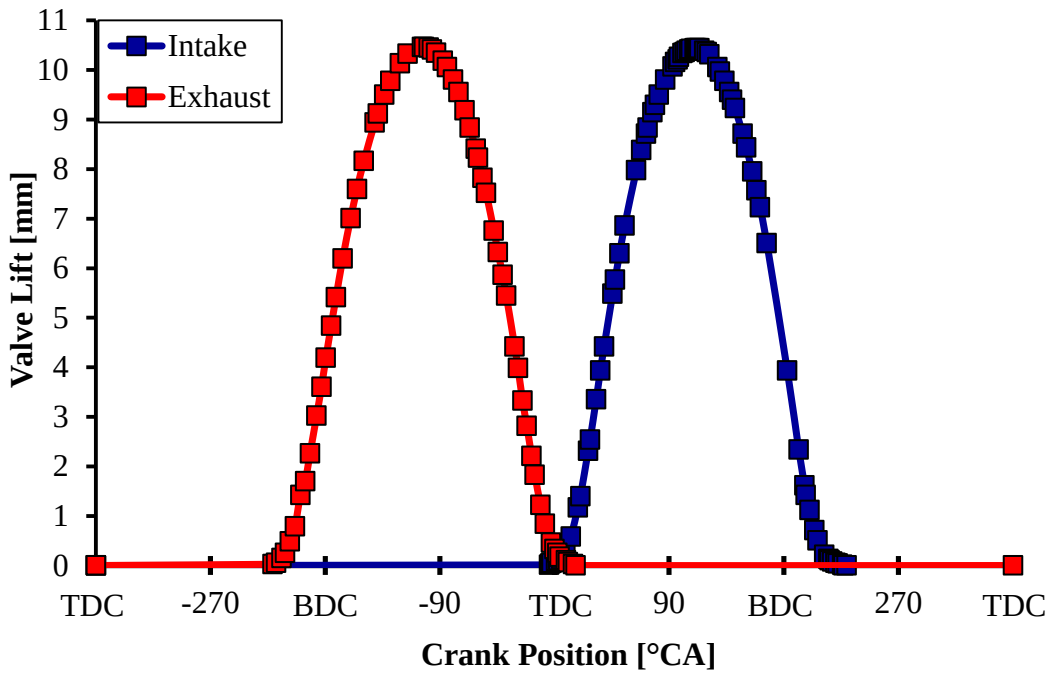

Figure 4-1: Measured Intake and Exhaust Valve Lift Profiles

The maximum valve lift measured was 10.46 mm, and therefore, the largest valve lift set on the flow bench was 10.5 mm. The measured intake and exhaust camshaft specifications are listed in Table 4-1.

Table 4-1: Measured Intake and Exhaust Valve Specifications

Event	**Unit**	**Value**
Intake Valve Opening IVO	° BTDC	10
Intake Valve Closing IVC	° ATDC	225
Intake Valve Duration	° CA	235
Exhaust Valve Opening EVO	° BBDC	45
Exhaust Valve Closing IVC	° ATDC	14
Exhaust Valve Duration	° CA	235
Valve Overlap	° CA	24

4.1.1 Non-Dimensional Flow Parameters

The intake flow performance of an engine can be characterized by non-dimensional parameters [29]. In this way, different geometries such as the intake port shape, valve lift, and intake systems, can be compared irrespective of their actual sizes.

The flow coefficient, C_f, is a measure of the intake port flow efficiency. It is a ratio of the experimentally measured mass flow rate to a theoretical maximum amount of air flow rate if the air is assumed incompressible. The equation used to calculate the flow coefficient is shown below in (4.2).

$$C_f = \frac{\dot{m}}{\rho\, A_t\, V_B} \tag{4.2}$$

where ṁ is the experimentally measured mass flow rate, ρ is the air density [kg/m^3], A_t is the simplified cross-sectional area of the valve throat [m^2] shown in Figure 4-2 [29], and V_B is the Bernoulli velocity [m/s] and is shown in (4.3):

$$V_B = \sqrt{\frac{2\,\Delta p}{\rho}} \tag{4.3}$$

where Δp is the pressure difference [Pa] across the intake port.

The flow coefficient utilizes that valve throat area as the reference. The flow coefficient will increase as the valve lift is increased and reflects the restrictions by the intake port geometry [1,29].

The discharge coefficient, C_d, is defined similarly as the flow coefficient except that it reflects the restriction to flow at low valve lifts. This is due to the valve curtain area used in the equation.

$$C_d = \frac{\dot{m}}{\rho\, A_c\, V_B} \tag{4.4}$$

where V_B is the Bernoulli velocity [m/s] in Equation 4.3, Ac is the valve curtain area [m^2] and is calculated by Equation 4.5:

$$A_c = \pi\, d\, l \tag{4.5}$$

where d is the valve throat diameter [m] and l is the valve lift [m].

The representative areas are illustrated below in Figure 4-2**.**

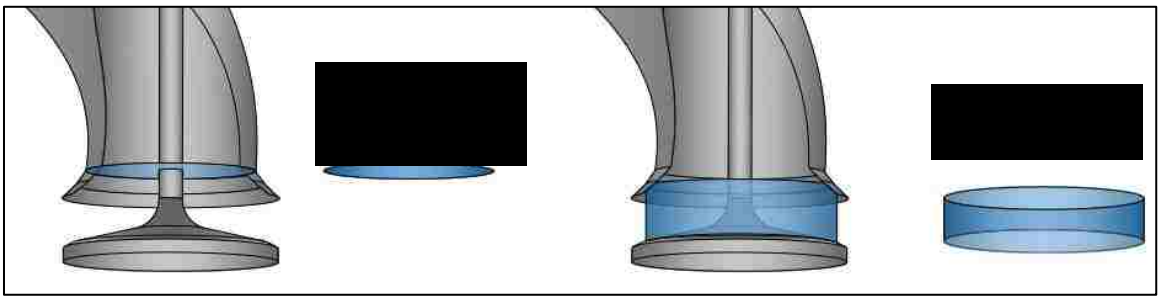

Figure 4-2: Areas for the Calculation of Flow & Discharge Coefficients

Another non-dimensional flow parameter commonly used for the characterization of the swirl is the swirl coefficient [4-6]. The swirl coefficient is defined as a ratio of the angular momentum of the rotating flow to the axial momentum in the cylinder assuming solid body flow [15,29]. The swirl coefficient, C_s, used for vane-type swirl meters is defined in Equation 4-6:

$$C_s = \frac{\omega\, B}{V_B} \tag{4.6}$$

where B is the cylinder bore [m], and ω is the rotational speed of the swirl meter [rads/s].

These non-dimensional parameters were used to calculate the overall intake generated swirl ratio, R_s. The intake generated swirl ratio is a single parameter which is a measure of the total angular momentum flux and takes into account the flow and swirl coefficients at each valve lift [14,15,29]. The swirl ratio is a much needed parameter for

the characterization of the ability to produce swirl motion in an engine. Equation 4.7 was used for the calculation of the swirl ratio. This swirl ratio definition has been used previously by Ricardo [29].

$$R_s = \frac{B\ S}{D^2} \frac{\int_{\alpha_{IVO}}^{\alpha_{IVC}} C_f\ C_s\ d\alpha}{\left[\int_{\alpha_{IVO}}^{\alpha_{IVC}} C_f\ \ d\alpha\right]^2} \tag{4.7}$$

Where *B* and *S* are the bore and stroke respectively [m], *D* is the valve inner seat diameter [m], α is the crank angle while the subscripts, IVO and IVC, refer to the opening and closing of the intake valve respectively [rad].

4.2 Steady Flow Baseline Measurements

The flow testing for the baseline measurement of the cylinder head was conducted under a test pressure of 10 inches of water gauge (2.48 kPa gauge). This test pressure was selected due to the lowered demand on the blower motors; only two were required to be turned on until larger valve lifts were reached. The valve lift was varied from 0.5 mm to 10.5 mm in 0.5 mm increments totaling 21 data points for each test. A total of five different tests were conducted to investigate the repeatability and also to obtain an average of all values measured.

The mass flow rate was calculated directly from the recording of the pressure difference across the orifice plate and the upstream pressure. Figure 4-3 presents the mass flow rate results of the five different steady flow tests conducted. The figure shows that the mass flow rates were similar for all five tests. The mass flow rate increased as the valve lift was increased; however, the trend is not linear. At a valve lift of 5 mm, the slope starts to decrease. For further increases in valve lift up to 9 mm, there was a

noticeable increase in the mass flow rate. However, no substantial increase in the mass flow rate was noticed for a valve lift beyond 9.5 mm. This could be due to the change in the flow area. At 9.5 mm valve lift, the valve curtain area was the same as the valve throat area.

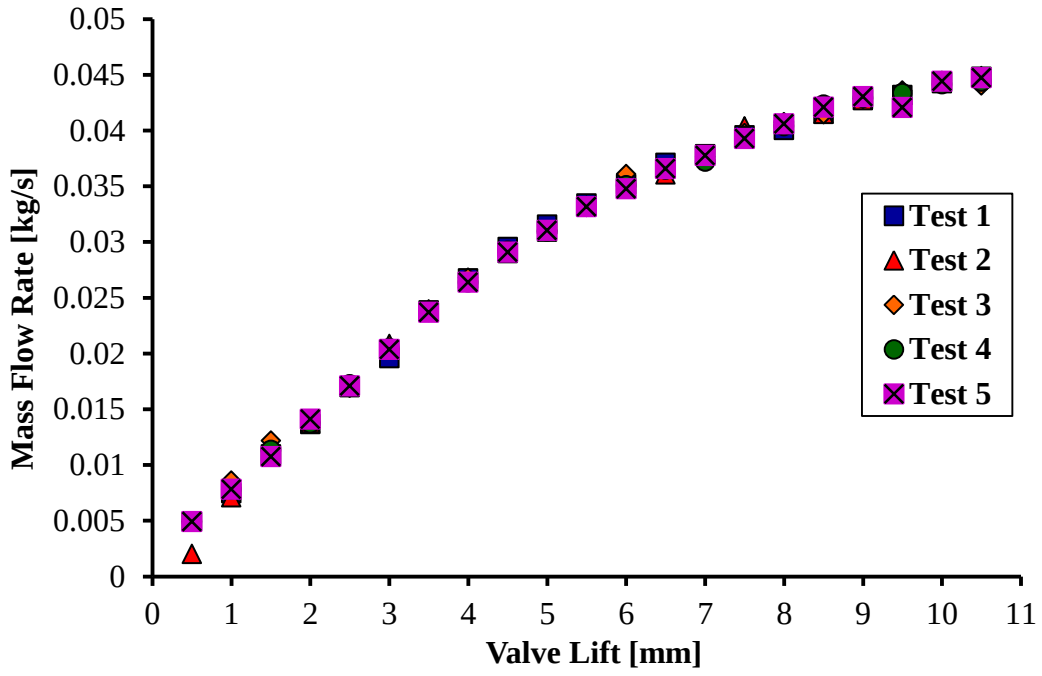

Figure 4-3: Mass Flow Rates of Baseline Steady Flow Test

The flow through the intake port was limited by the valve lift and corresponding valve curtain area until such valve lift when the valve curtain area was greater than the valve throat area. At this point the throat area was the restrictor and no further increases in valve lift had a major increase in the mass flow rate. This transition position of valve lift defines the full valve opening. The mean values of the mass flow rate, calculated from the five sets of tests, are shown in Figure 4-4.

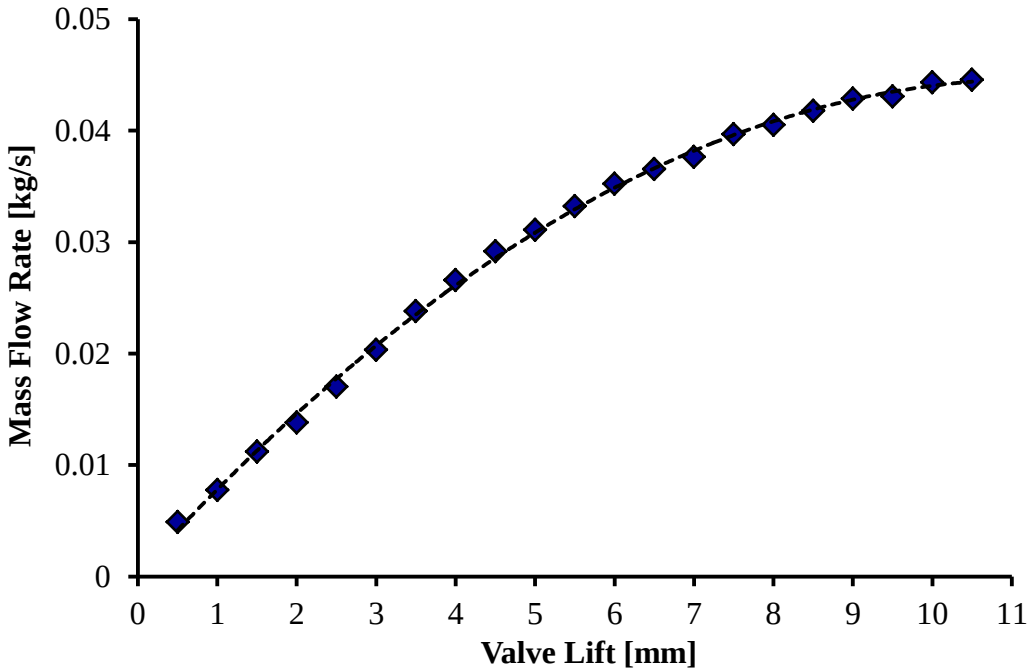

Figure 4-4: Average Mass Flow Rate of Baseline Measurement

The flow coefficient is calculated from the average mass flow rate at each valve lift. The flow coefficient results are displayed in Figure 4-5 from the five tests. As mentioned above, the flow coefficient reflects the flow performance at larger valve lifts due to the reference flow area that was used in the calculation. For all five tests, there were minimal variations in the flow coefficient at each valve lift. The largest deviations occurred only at lower valve lifts. The average of the flow coefficient at each valve lift was calculated along with the standard deviation. This is shown in Figure 4-6 with the standard deviation indicated by the error bars.

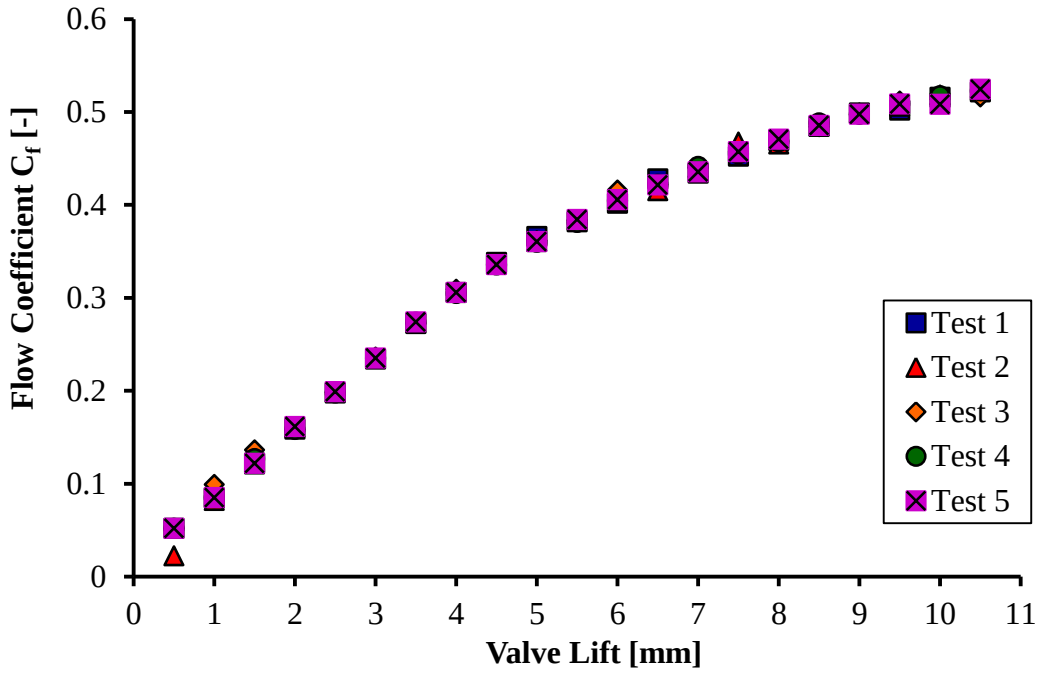

Figure 4-5: Flow Coefficients from Five Baseline Measurements

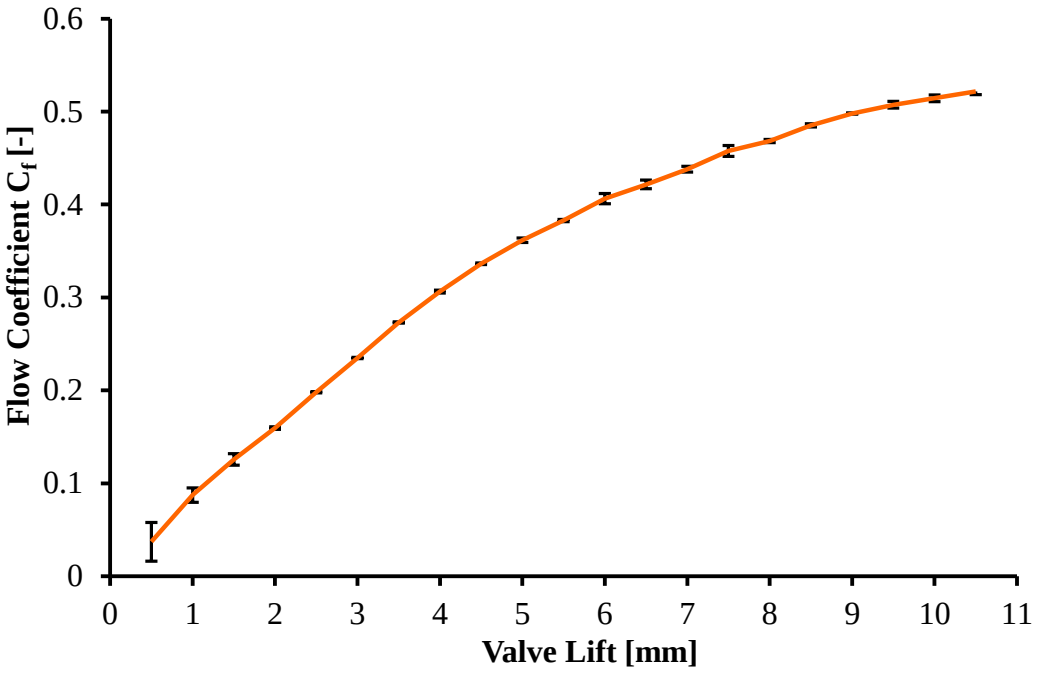

Figure 4-6: Average Flow Coefficients from Baseline Measurement

The standard deviation in the flow coefficient at small valve lifts, up to 1mm, was of the same order as the calculated flow coefficient. However, for large valve lifts, the standard deviation was two to three orders of magnitude lower than the measured values. This indicated that the results had acceptable consistency.

The average values of the discharge coefficients from the five tests are presented in Figure 4-7. The resultant profile of the discharge coefficient is not as smooth as the flow coefficient. The profile begins with an abrupt decrease from 0.5 to 1 mm of valve lift. From 1 to 2 mm, the values decrease in a linear fashion until another sudden change in the slope at 2 mm occurs, and continues with a gradual decrease. It was noticed that the value of the discharge coefficient at 0.5 mm of valve lift was quite large (0.98). This could be caused by pressure waves formed at the valve lips in the intake port at small valve lift [50]. The large flow efficiency is also attributed to the helical design of the intake port which has a larger peripheral flow path than a typical straight intake port and typically, larger discharge coefficients are produced [1,16]. Beyond 4 mm of valve lift, the discharge coefficient decreased almost linearly. The decrease in the discharge coefficient was caused by the increase in the flow area that was used to calculate it. As the valve lift was increased, the valve curtain area became less restrictive than the port throat area.

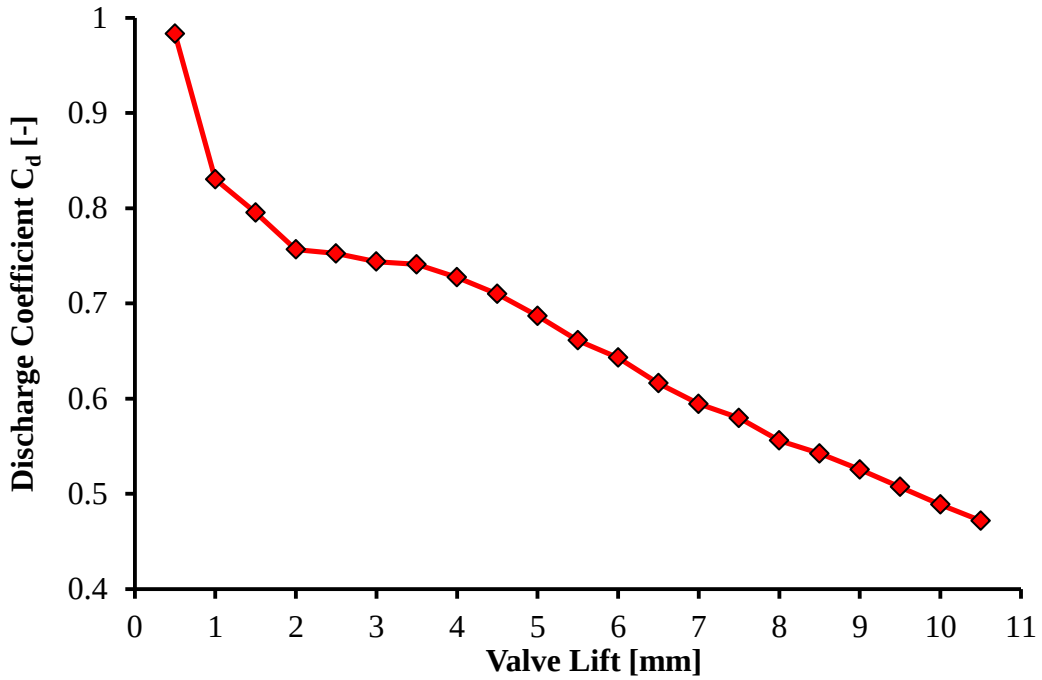

Figure 4-7: Average Values of Discharge Coefficient from Baseline Measurements

The Reynolds number was calculated to ensure that the flows in the port (RE_{port}), valve throat (Re_{valve}), and cylinder (Re_{cyl}) areas were turbulent. As mentioned earlier, no universal industrial standard exists for the test pressure across the intake port, although it is universally acknowledged that the flow must be turbulent in order to correlate the non-dimensional flow parameters (measured on the flow bench) to actual engine operation [29].

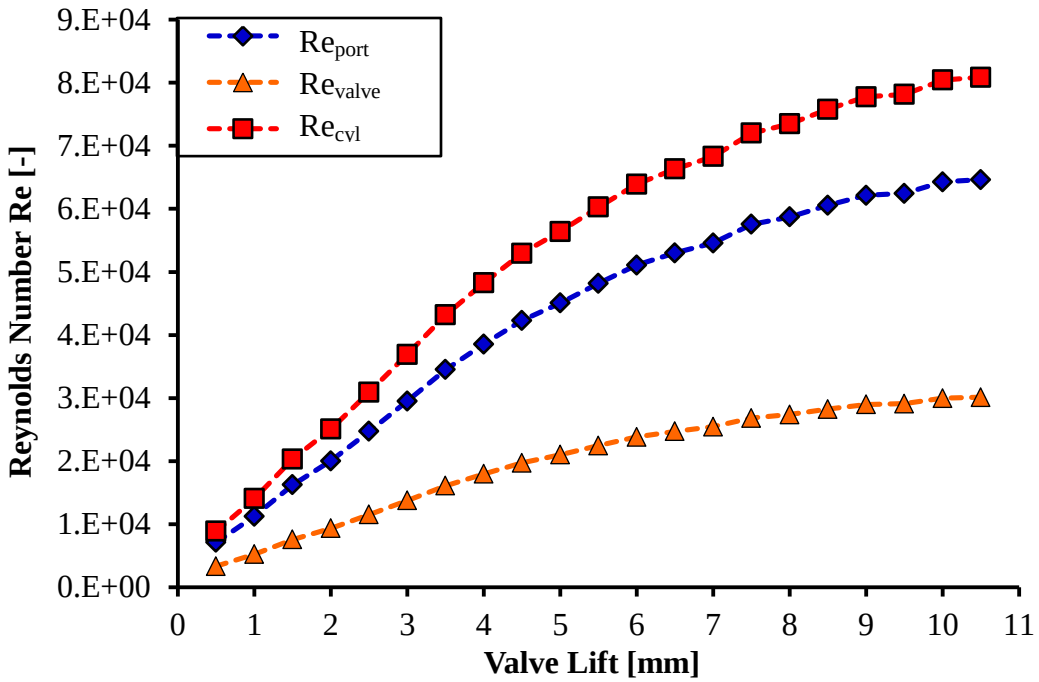

Figure 4-8: Reynolds Number in Different Flow Areas from Baseline Measurements

As illustrated in Figure 4-8, the calculated Reynolds number in the different respective flow areas are above 4,000. This indicated that fully developed turbulence existed in the valve, intake port, and cylinder flows, which confirmed that the test pressure of approximately 10 in H_2O was sufficient for the flow bench tests.

The recorded average swirl meter speed with varying valve lift is shown in Figure 4-9. The swirl speed is required for the calculation of the swirl coefficient (C_s) and the overall intake generated swirl ratio (R_s) given by Equations 4.6 and 4.7 respectively.

The swirl meter rotated in a counter clockwise direction when observed through the open end of the cylinder, and remained rotating in the same direction at each different valve lift. This orientation is defined as the positive vector direction throughout this work.

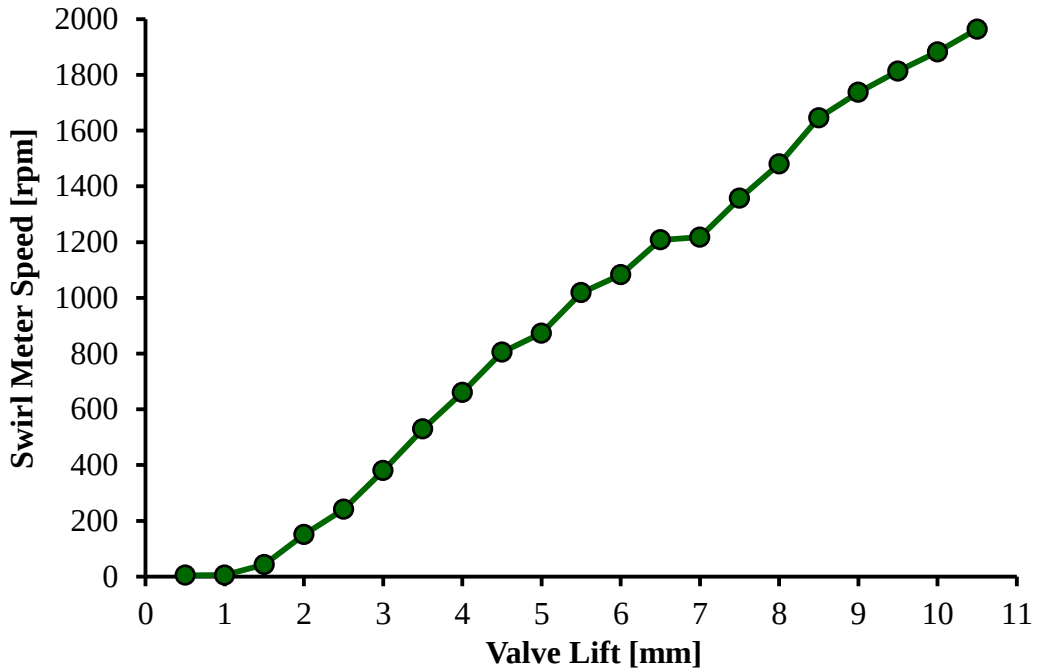

Figure 4-9: Average Swirl Speed from Baseline Measurement

The swirl speed increased in a linear manner as the valve lift was increased. This was attributed to the helical geometry of the intake port which shaped the rotational motion of the charge before the charge entered the cylinder. In the low valve lift range, 0.5 and 1 mm, the measured swirl speed was relatively low due to the small area available for the flow into the cylinder. Also, due to the low mass flow rates at these valve lifts, the measurement of the swirl made by the vane-type swirl meter may have some disadvantages. It has been found that the measurement with vane type swirl meter may under predict the swirl at low flow rates due to the air slip occurring on the blade, friction in the bearing and inertial effects [15]. However, as the valve lift increased and the flow area increased, the swirl speed increased in a linear fashion.

The swirl coefficient, defined by Equation 4-6, was calculated at each valve lift and is presented in Figure 4-10.

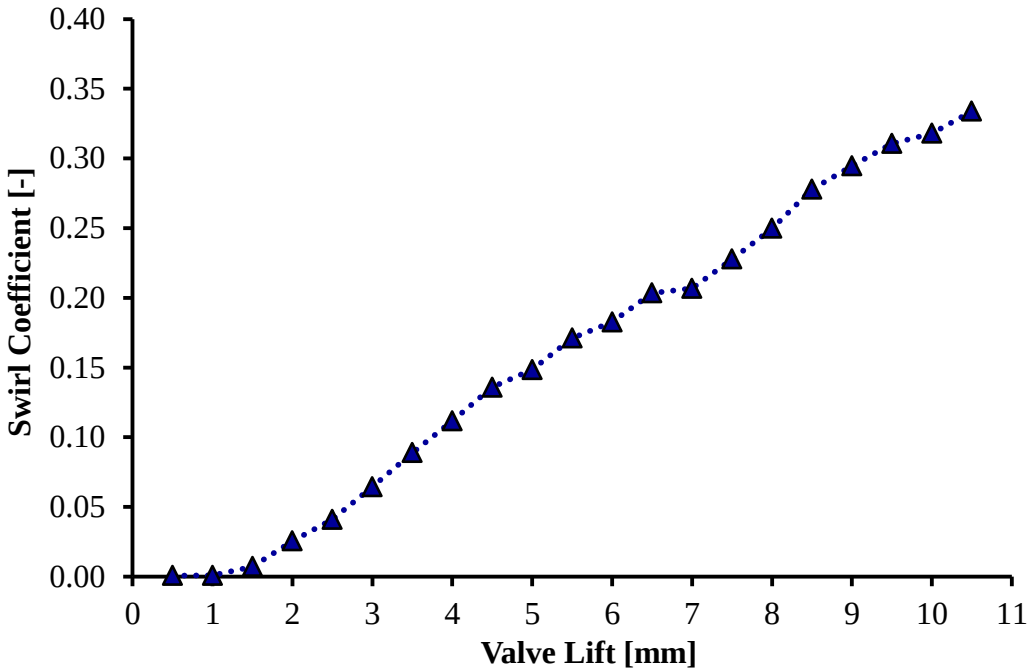

Figure 4-10: Average Swirl Coefficient from Baseline Measurements

The swirl coefficient showed the same trend as the measured swirl speed since it is merely a ratio of the angular momentum to the axial momentum. The swirl ratio (Rs), defined by Equation 4.7, was calculated to obtain a baseline reference of the overall intake generated swirl. The equation was integrated numerically using a Matlab Code. The calculated global swirl ratio for the baseline measurements was 1.34.

4.3 Chapter Summary for Baseline Steady Flow Results

Baseline steady flow measurements of the cylinder head were conducted on the steady flow test bench. The flow parameters, defined at the beginning of the chapter, were used for the evaluation. A series of five tests were conducted to obtain average values. A swirl ratio of $R_s = 1.34$ was obtained from the baseline results.

CHAPTER 5: ENHANCEMENT OF SWIRL MOTION

The results of the numerical simulation are presented in this chapter. The baseline measurements presented in Chapter 4, are compared with the CFD simulation results to determine whether the model is acceptable to represent the characteristics of the flow in the cylinder during induction. The angular momentum, which is defined later in this chapter by Equation 5.1, was determined at the same location where the swirl meter was positioned. After the CFD model was tuned, different insert geometries for the intake manifold were simulated to predict a possible increase in the angular momentum/swirl speed.

The insert which was produced the largest increase in the swirl speed was fabricated and tested on the flow bench. The flow parameters of the baseline case were compared with the insert.

5.1 Introduction

The CFD simulations were conducted using Convergence CFD Simulation Suite developed by Convergence Science [42]. The geometric boundary of the intake port was generated by a 3D scanned mold. The model replicated the experimental flow bench setup, with a tubular section placed before the cylinder head as the inlet, and the opposing end of the cylinder as the outflow boundary layer (Figure 3-4). The results from the experimental flow bench tests, mainly the mass flow rate and pressures, were used as inputs for the inflow and outflow boundaries. The experiments were conducted at room temperature therefore, the input temperature was assumed to be 300 K for all cases. The numerical simulations were conducted from a valve lift of 0.5 to 10.5 mm in increments

of 0.5 mm. The purpose was to develop a tuned model which could match the empirical results from the flow bench. This model was then used to predict the swirl production capabilities of different inserts of different geometries placed upstream of the intake port.

5.2 Numerical Model Validation

The mass flow rates measured at each valve lift during the steady flow bench tests were used for the inlet boundary conditions in the numerical model. The output of the Converge simulation was analyzed using the post-processing software, CEI Ensight 10.1. The data for each individual cell within the swirl measurement region, indicated in Figure 3-4, was extracted and used for the calculation of the swirl speed. To calculate the swirl speed, the angular momentum about the z-axis of all the cells contained within the swirl measurement region was obtained using Equation 5.1 [42, 43]:

$$L_z = \sum_{n=1}^{total\ cells} \rho_n V_n [(x_n - x_c)v_n - (y_n - y_c)u_n] \tag{5.1}$$

where ρ_n is the density, V_n is the volume, x_n and y_n are the x- and y-coordinates of each cell respectively, x_c and y_c are the coordinates of the center of mass, and v_n and u_n are the x and y components of velocity.

The moment of inertia about the z-axis of each cell was then calculated using Equation 5.2:

$$I_z = \sum_{n=1}^{total\ cells} \rho_n V_n [(x_n - x_c)^2 + (y_n - y_c)^2] \tag{5.2}$$

Finally, the swirl speed was obtained by dividing Equations 5.1 by 5.2 [42,43].

$$\omega_{swirl} = \frac{L_z}{I_z} \tag{5.3}$$

The swirl measurement location contained approximately 175,000 cubic cells of 1 mm edge length, and the whole model contained a total of approximately 3.2 million cells. Figure 5-1 shows the volume of cells within the swirl measurement location used for the swirl speed calculations which corresponds to the same physical location and thickness where the swirl meter was positioned. This cell size was determined to be sufficient, after trials, to represent the swirl speed accurately.

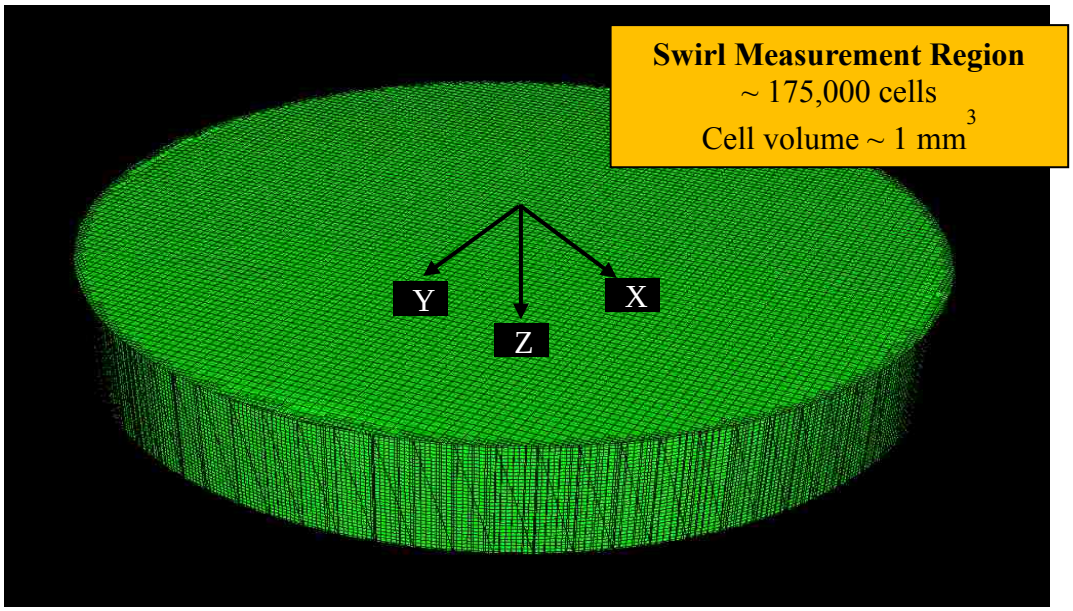

Figure 5-1: Swirl Measurement Region

The results of the numerically calculated swirl speed are shown compared with the flow bench test results of the baseline measurement in Figure 5-2. The results of a coarse grid (cubic cells of 8 mm edge length) are shown for comparison.

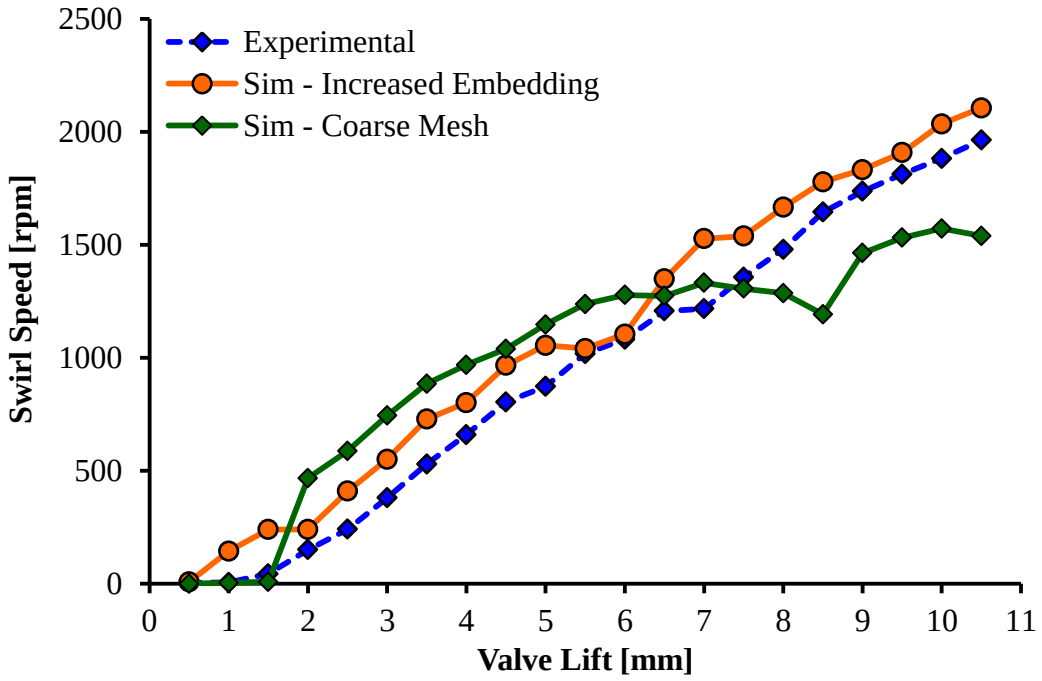

Figure 5-2: Comparison of Numerical and Experimental Swirl Speed Results

The results from the model with the course grid over-predicted the swirl speed at low to medium valve lifts (2–6 mm) and under-predicted the swirl speed at large valve lifts (8-10.5 mm). The results of the refined grid model, which featured the increased embedding, followed a very similar trend to the experimental results. The swirl speed at low valve lifts was slightly higher than the experimental results. This could possibly be a result of the losses associated with the vane-type swirl meter which include friction from the bearing, air slip on the blade, and rotational inertia effects [15]. However, at larger valve lifts, these losses may only have a minor effect on the overall swirl speed. As the

valve lift increased, the difference in swirl speeds between the simulation and experimental results decreased.

At the largest valve lift of 10.5 mm, the difference between the experimental and numerical results with the increased embedding was only 7.3% compared to 21.6% for the coarse grid results. Although the finer mesh produced a better result, the simulation time increased by a factor of 14 compared to the coarse mesh, which made this computationally expensive.

The flow and discharge coefficients were calculated for the increased embedding results and compared to the empirical values at each valve lift (Figure 5-3).

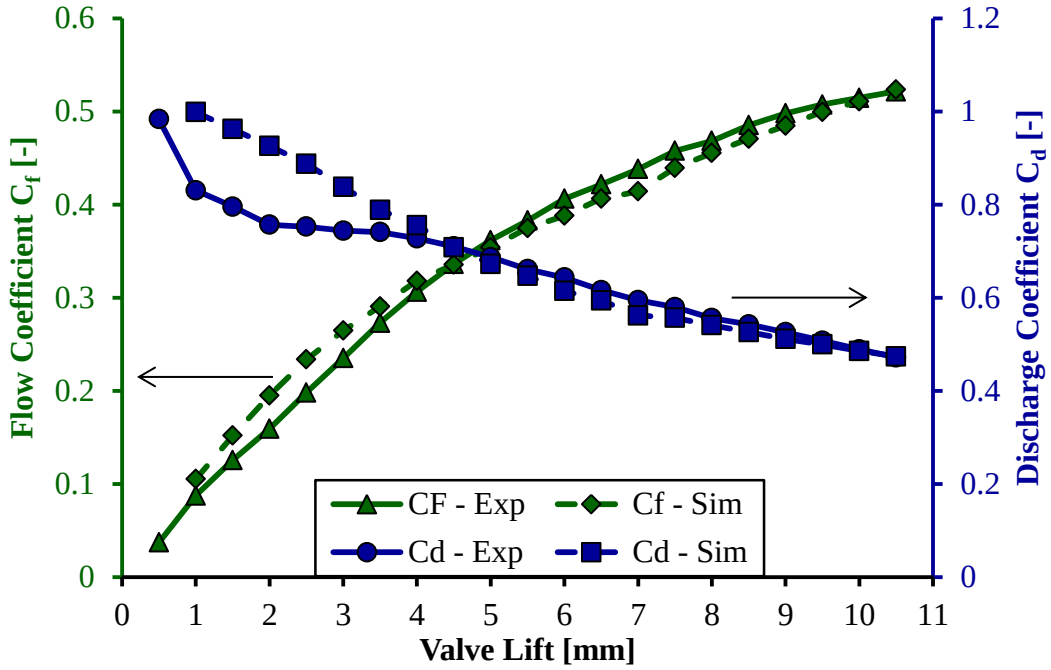

Figure 5-3: Comparison of Flow and Discharge Coefficients from Experimental and Numerical Results

The flow coefficient obtained from the numerical results matched the measured results quite well from mid to high valve lifts. At low valve lifts, 0.5 to 4 mm, over predictions were noticed in the flow coefficient. Similarly, larger differences were noticed in the discharge coefficient at the same range of valve lifts (0.5 - 4 mm). At low valve lifts, the flow velocity and structure are dependent upon the geometries of the intake valve and the valve seat. This could be an indication that the geometries in the model may not be completely accurate. Since much of the induction flow process consists of valve lifts greater than 4mm, lower accuracy in this region was deemed to be acceptable. The simulated results of the discharge coefficient matched the empirical results well for valve lifts greater than 4 mm. Therefore, the model was considered acceptable to be used for subsequent simulations to evaluate different intake manifold inserts with the objective to increase the swirl speed.

5.3 Enhancement of Swirl Motion

The enhancement of swirl in a four-valve engine can be accomplished by blocking one of the adjacent valves [21]. This allows the total amount of the intake flow to enter one port and the air is ejected tangentially along the cylinder wall. However, this method is not possible for engines with two valves (one intake and one exhaust valve). This can be even more challenging if the intake port is helically shaped as the flow structure is mainly dependent upon the port shape and positioning.

For these reasons, different designs of intake manifold inserts, placed just upstream of the intake port entrance, are investigated numerically with the intention of increasing the swirl speed and the overall swirl ratio. The inserts are designed in such a

manner as to either increase the velocity or the angular momentum of the incoming air before entering the intake port. Figure 5-4 shows the sketches of the different inserts tested in the simulations.

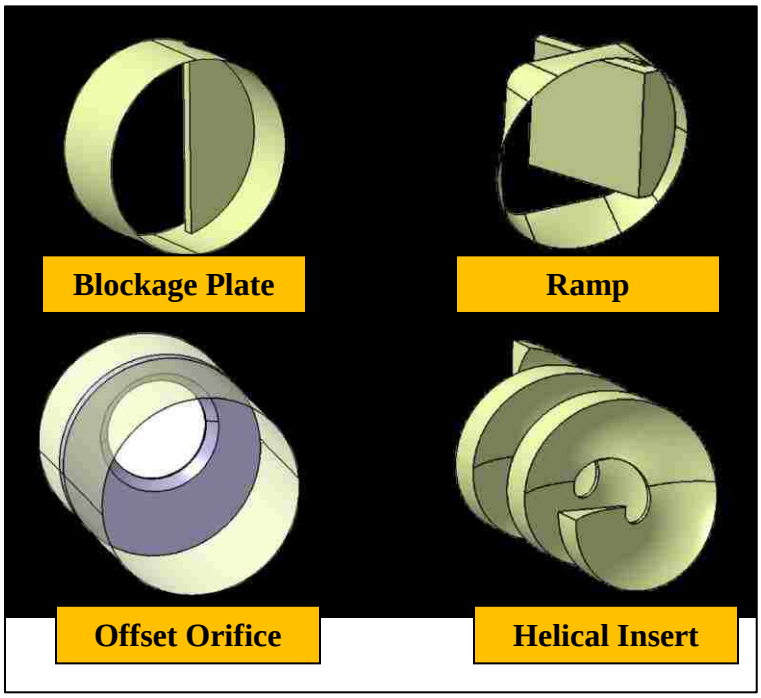

Figure 5-4: Intake Pipe Insert Geometries Evaluated in Simulations

Both the blockage plate and the ramp inserts share a similar strategy to increase the swirl speed. A portion of the flow area is blocked and more of the intake air can be directed tangentially along the inside wall of the intake port thereby providing the air more time to develop a vortex in the intake port. The offset orifice insert increases the velocity of the air entering the intake port. The dependence of the radial positioning of the offset orifice relative to the intake port is also investigated. The helical insert aims to increase the rotational motion of the charge before entering the intake port, and increases the velocity as well by creating a restriction. This design concept is similar to Schelkin

spirals which are often used in shock tube experiments to increase the flame speed by the generation of turbulence [48].

The swirl generation ability of the above-mentioned intake inserts are evaluated through CFD simulations. The valve lift is set to 10.5 mm since this valve lift produced the maximum swirl speed during the flow bench tests. The mass flow rate is also fixed for all cases and set to the same value that was calculated for the experimental measurements at a valve lift of 10.5 mm

The spatial mean tangential swirl velocity produced within the cylinder is calculated using Equation 5-4. The tangential swirl velocity is calculated to investigate the development of the swirl velocity within the entire cylinder.

$$Mean\ Tangential\ Swirl\ Velocity = \frac{\sum V_i\ A_i}{A_T} \tag{5.4}$$

where V_i and A_i are the tangential swirl velocity [m/s] and two-dimensional area [m^2] of each cell respectively and A_T is the total two-dimensional area [m^2] of the plane which contained the cells.

The mean tangential swirl velocity is calculated at different axial planes starting from the cylinder head surface to the swirl measurement region. These results are plotted for the different intake manifold inserts as shown in Figure 5-5.

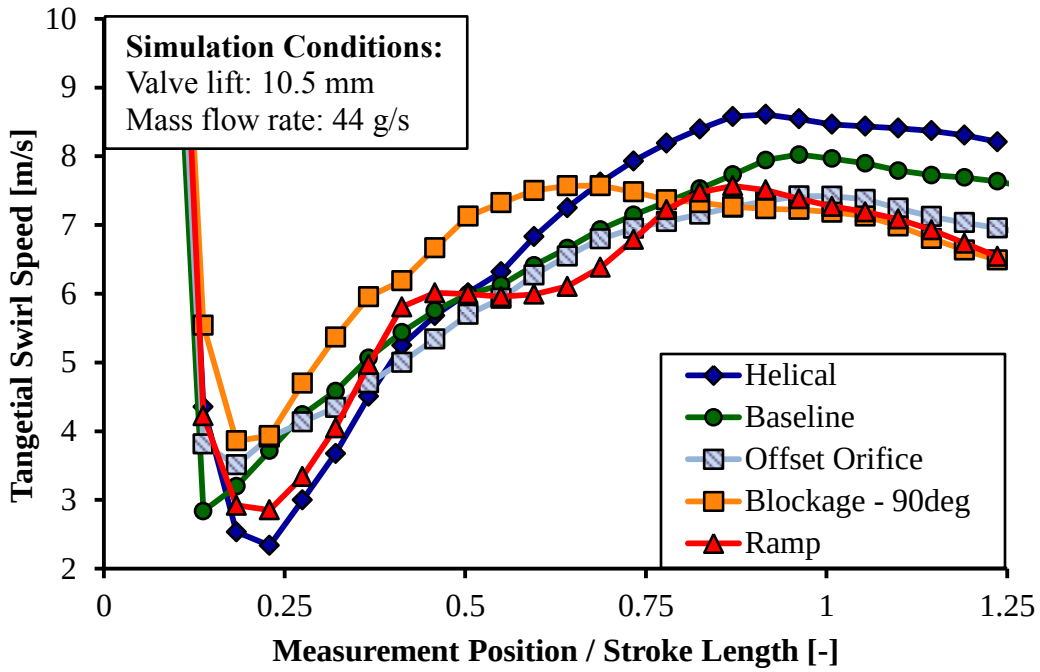

Figure 5-5: Effect of Intake Geometry on the Production of In-Cylinder Swirl

From the results shown in Figure 5-5, it is clear that the helical insert produces the largest swirl velocity above 75% of the stroke length and in the swirl measurement region. The initial swirl velocity, produced by the blockage plate, is greater than all of the other inserts. However, the swirl velocity begins to decay past 60% of the stroke length and results in the lowest swirl speed in the measurement location. The ramp and offset orifice designs also produce lower swirl speeds compared to the baseline case along the cylinder axis.

The swirl angular velocity is determined in the region where the swirl meter measurements were made for the baseline experimental tests. The angular velocity is determined by the method described in Section 5.2 in which the angular momentum and the inertia of each individual cell within the swirl measurement region is calculated. The swirl angular speed of the different intake inserts is presented in Figure 5-6.

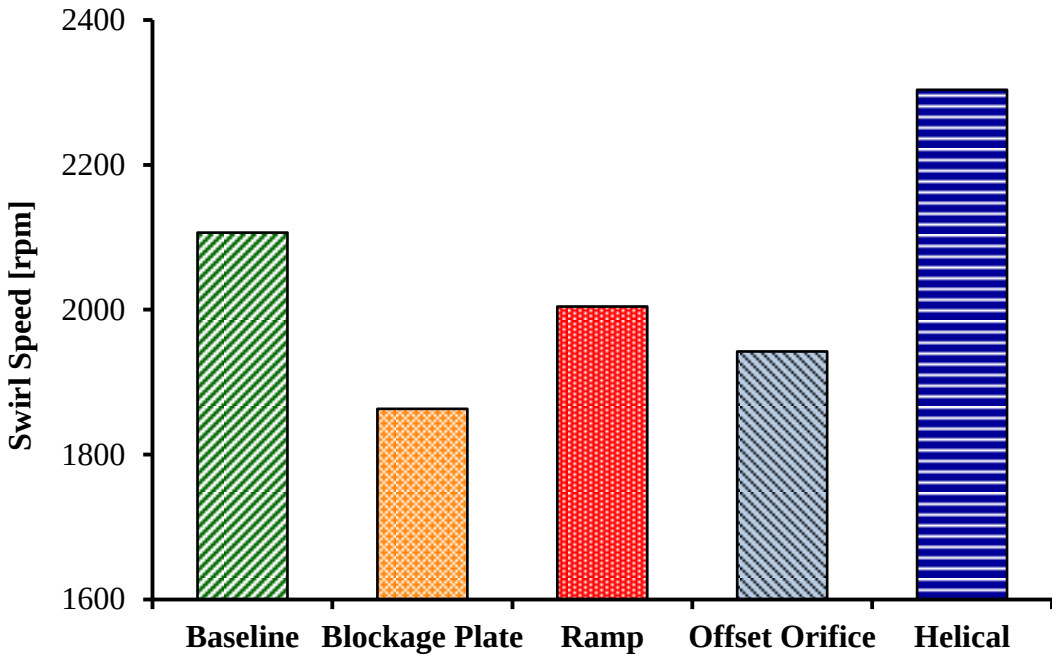

Figure 5-6: Numerical Results of Swirl Speeds Produced by Different Intake Runner Geometries

The results of the calculated swirl speed in the swirl measurement region follow the same trend displayed in Figure 5-5. The blockage plate produces the lowest swirl speed of all the different intake designs followed by the offset orifice and ramp design. The helical insert produced the highest swirl speed, relative to the baseline, and increased the swirl speed by approximately 10%.

Since the helical intake design showed the best ability to increase the swirl speed in the CFD simulations, it was selected for manufacturing and testing on the flow bench.

5.4 Steady Flow Investigation of Insert

Based on the results from the simulations, the helical insert was selected for manufacturing based on the prediction of increased the swirl speed. A picture of the

helical insert, after manufacturing and before modifications were made to cut and welded inside the intake tubing, is shown in Figure 5-7.

Figure 5-7: Helical Insert after Manufacturing

After the helical insert was set up on the flow bench, tests were conducted to investigate whether an increase in the swirl ratio over the baseline could be obtained. The effect of the radial orientation of the insert was investigated to determine the position that generated the highest swirl. For these tests, the valve lift was set at 10.5 mm, since the highest swirl speed was obtained at this lift. The mass flow rate was set at 49 g/s for all the orientation tests. The insert was rotated by 90° for each different test. The physical orientation, viewed from the intake manifold, and the swirl speed test results of the different orientations are shown in Figure 5-8 and Figure 5-9 respectively.

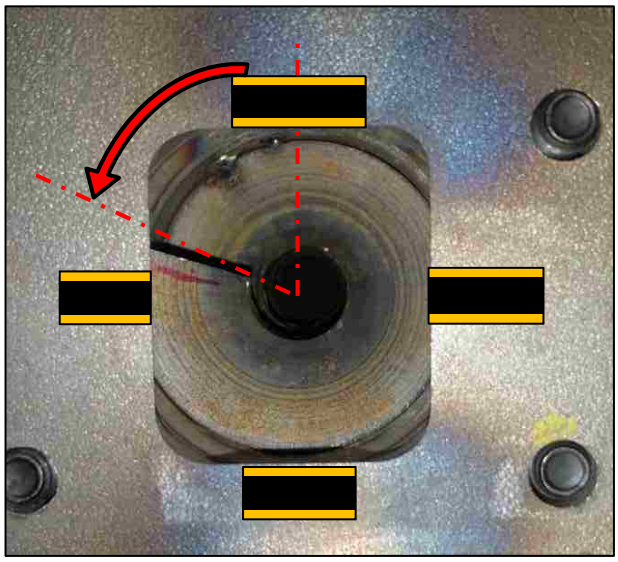

Figure 5-8: Rotational Orientation of Helical Insert

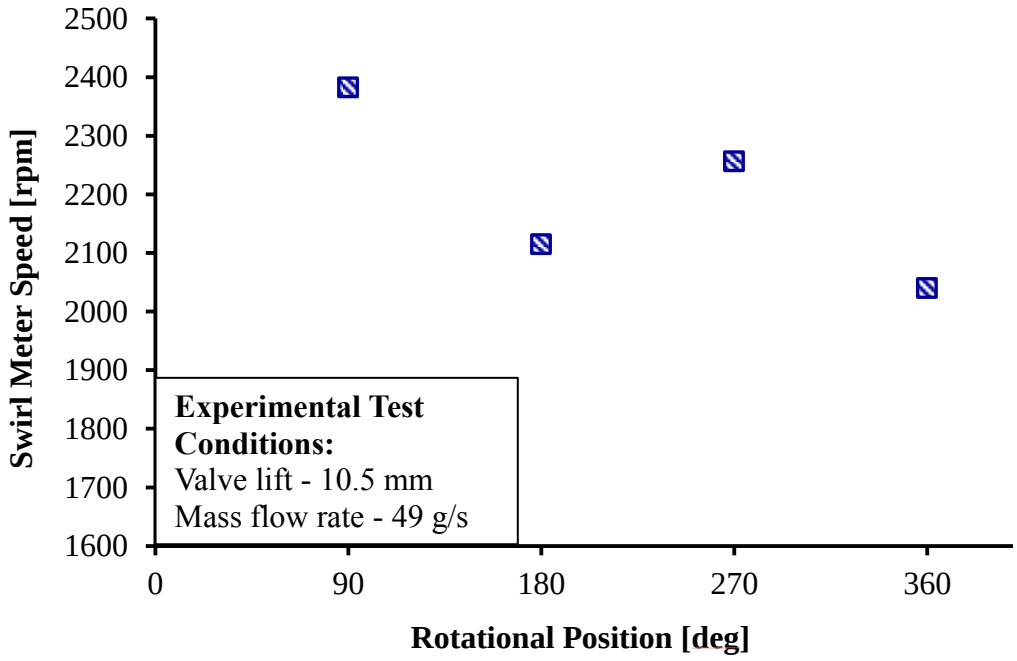

Figure 5-9: Effect of Insert Rotational Position on Swirl Speed

The results of the swirl speed for the different rotational positions showed a fairly strong dependence on the orientation with a maximum swirl observed at the 90° position.

When the insert was positioned at 180°, the swirl speed dropped significantly by more than 250 rpm, approximately 11%. The lowest swirl speed recorded occurred at the 360° position producing a speed of 2040 rpm which was a reduction of 14% compared to the maximum speed obtained at the 90° position. Thus, the helical insert was positioned at the 90° orientation for the flow bench test for the measurement of swirl at each valve lift.

Figures 5-10 through Figure 5-13 show the comparison of the flow bench tests with the helical insert and the baseline measurements. The flow data presented for the insert are the average values from five different sets of test conducted, similar to the baseline measurements. The mass flow rates from the flow bench tests were matched since the intake air pressure on the engine test setup could be increased, accounting for any flow losses that would be incurred using the insert. The flow bench test results of the mass flow rate at each valve lift between the baseline and insert are shown in Figure 5-10.

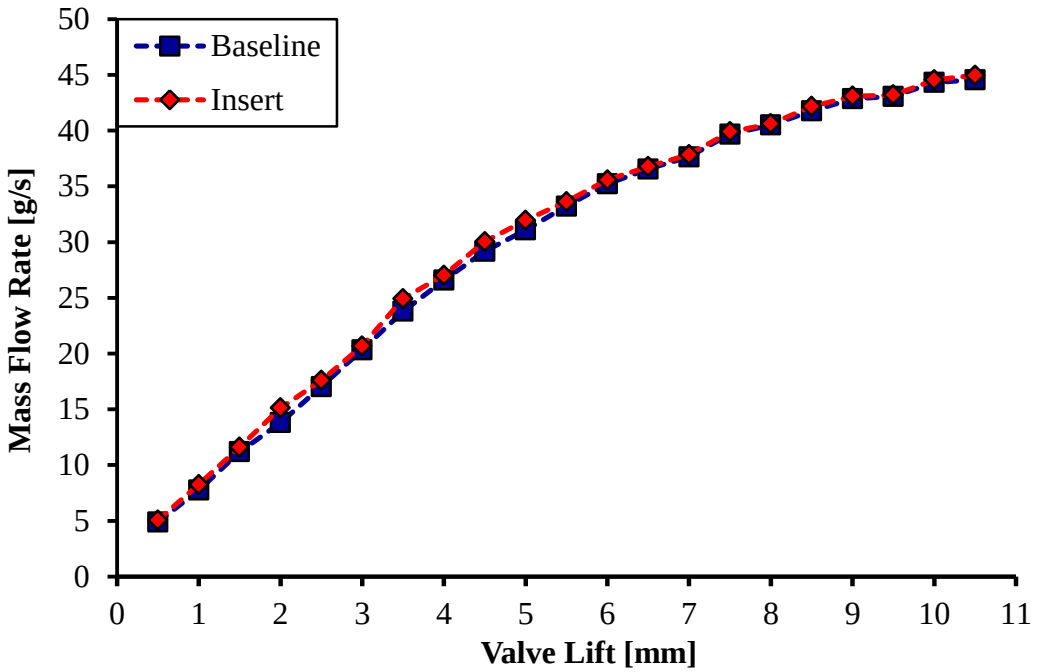

Figure 5-10: Comparison of Mass Flow Rates from Flow Bench Tests from Baseline and Insert Measurements

It is shown, in figure 5-10, the average values of mass flow rate from the five sets of tests at each valve lift were very similar to the baseline measured mass flow rate. The largest differences occurred at 1 and 2 mm of valve lift with a higher mass flow rate for the insert – 8.18% and 8.78% respectively over the baseline. The difference in mass flow rate from 2.5 – 5 mm was less than 5% and from 5.5 – 10.5 mm was less than 1%.

The flow coefficient and discharge coefficient are shown in comparison with the baseline values in Figure 5-11.

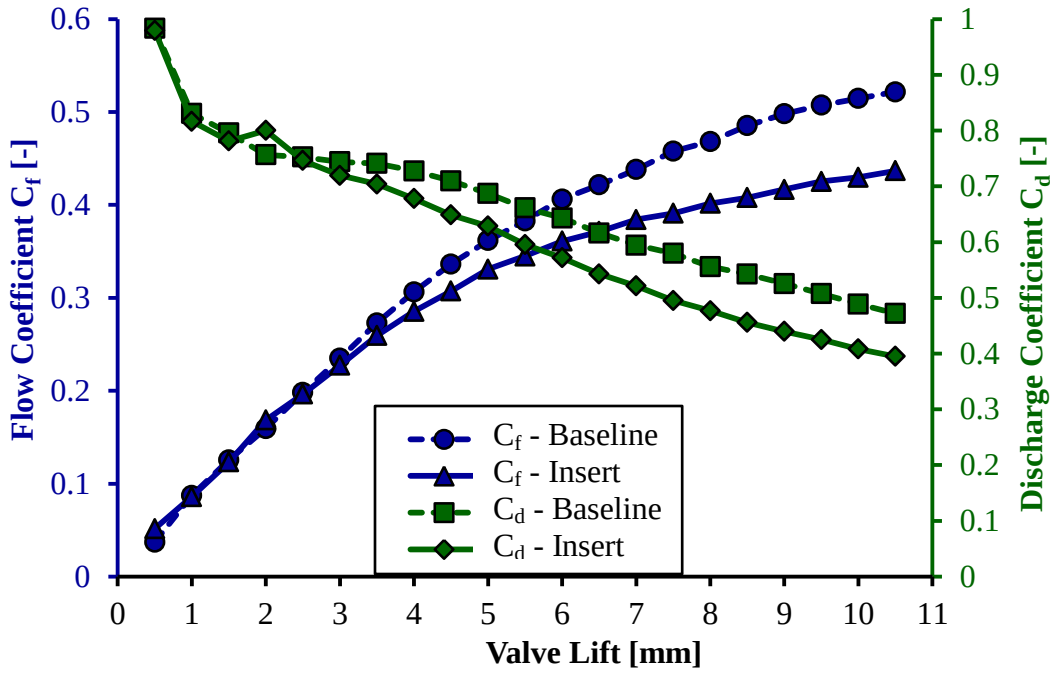

Figure 5-11: Effect of Insert on Flow Characteristics

From the comparison of the flow coefficient, it was found that in the valve lift range of 0.5 – 3 mm, there not much difference between the baseline and insert values. This was due to the fact that, by definition the flow coefficient outlines the flow performance at large valve lifts, therefore, the restriction of the insert may not be as evident at low valve lifts [29]. For valve lifts greater than 3 mm, the restriction caused by the insert lead to a reduction in the flow coefficient. At 10.5 mm, the reduction in the flow coefficient was more than 16%. The discharge coefficient also reduced beginning from 3 to 10.5 mm of valve lift. The insert introduced a restriction to flow and as a result, the C_f and C_d were reduced. This is not as apparent at very low valve lifts, which suggests that the restriction is mainly contributed to the low valve lift. Therefore, as the valve lift was increased, the use of the insert leads to greater flow losses and the flow efficiency is decreased.

The effect of the insert on the swirl coefficient is shown in Figure 5-12. The swirl coefficient, calculated from Equation 4.6, was compared with the baseline swirl value. It can be seen that increases are present in the low, medium, and large valve lift ranges. The insert provided modest improvements in the swirl coefficient throughout the entire valve lift profile.

The effect of the insert geometry on the generated swirl speeds, obtained from the swirl meter, is shown in Figure 5-13. The results showed large increases beginning at 5.5 mm up to the maximum valve lift. At 10.5 mm of valve lift, the swirl speed is increased by 20%. There were negligible changes in the speeds form 2.5 – 5 mm of valve lift while the swirl speed was significantly increased at 1.5 and 2 mm valve lift by 190% and 31% respectively. Using Equation 4.7 and the flow data obtained from the insert, a swirl ratio of 1.54 (R_s = 1.54) was calculated for the insert. The insert provided an increase of 15% over the baseline swirl ratio.

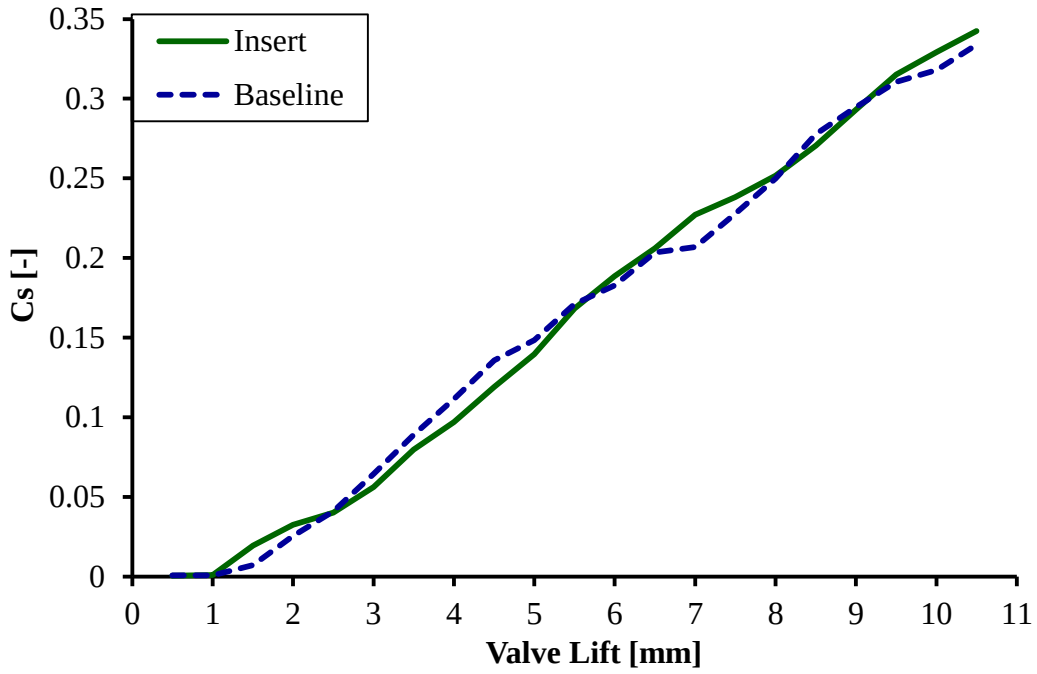

Figure 5-12: Effect of Insert on the Swirl Coefficient

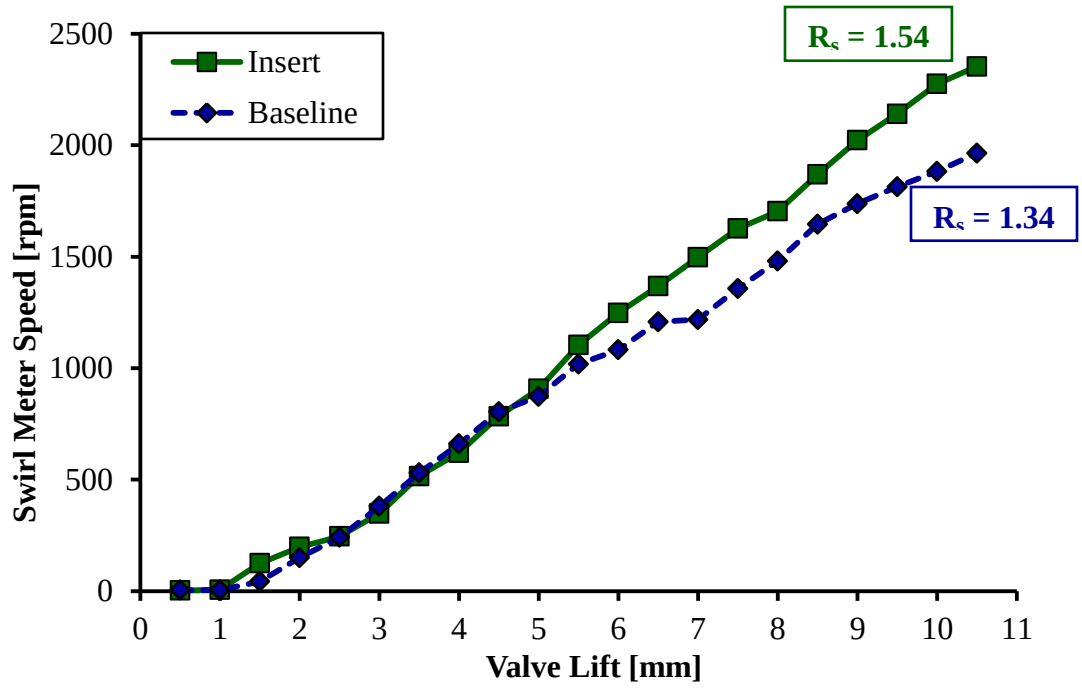

Figure 5-13: Effect of Insert on Measured Swirl Meter Speed

5.5 Chapter Summary for Enhancement of Intake Generated Swirl

In this chapter, the results from the numerical model of the flow bench set-up were compared with the experimental baseline results. The model which featured a refined grid produced a closer agreement in the swirl speed trend to that of the experimental results. In addition, the absolute differences in the swirl speed at each valve lift were lower for the finer meshed model. This model was then used to evaluate different intake insert designs numerically, to determine which design produced the largest increase in the swirl speed. The helical insert design displayed the highest effect of increased swirl speeds and was manufactured. The manufactured insert was evaluated on the flow bench platform from five different tests at the same mass flow rates calculated from the baseline measurements at the corresponding valve lifts. An increase in the swirl speed and swirl coefficient was noticed while the flow and discharge coefficients were reduced due to the geometrical restriction by the insert. A swirl ratio of $R_s = 1.34$ was obtained from the baseline results. The swirl ratio obtained with the insert was $R_s = 1.54$ which was an increase of approximately 15%. The following chapter presents the results of the single cylinder engine tests carried out with and without the insert attached to the intake manifold under lean-burn conditions.

CHAPTER 6: ENGINE TEST RESULTS

This chapter presents the experimental tests conducted on the single cylinder research engine. Baseline tests were performed without the insert. A lambda sweep was performed during the engine tests, by increasing the dilution level with excess air. Engine tests were also performed with the helical intake manifold insert. The mass flow rates of air and fuelling rates were maintained constant. A spark timing sweep was conducted with the onset of knock as the limitation of advancing and the exhaust temperature as the limitation on spark retarding. A comparison of the engine test results was made, more specifically analyzing the exhaust emissions and indicated thermal efficiencies.

6.1 Low Load Engine Test Results with Enhanced Swirl

Engine tests were conducted at 3 bar and 6 bar IMEP, which will be defined as the low load and the high load respectively throughout this thesis. The low load engine tests, with and without the insert, were conducted on the same day. The mass air flow rate and fuel amount were fixed while the spark timing was advanced and retarded to find the optimal timing which produced the maximum break torque (MBT). The limitation on the spark timing advancement was engine knock, whereas the spark timing retardation was ceased when a substantial drop was noticed in the IMEP as well as high COV_{IMEP} and HC emissions indicating incomplete combustion. The conditions for the low load engine tests are shown in Table 6-1. The mass air flow and fueling rate were held constant, as shown in Figure 6-1, for the low load engine tests.

Table 6-1: Low Load Engine Test Conditions

IMEP	[bar]	~ 3
Engine Speed	[rpm]	1300
Start of Injection	[°CA]	-350°ATCD
Spark Timing	[°CA]	Sweep
Ignition Charging Duration	[ms]	5
Lambda	[-]	Sweep
Fuel Injection Type	[-]	Port Injection
Combustion Chamber Shape	[-]	Offset Bowl

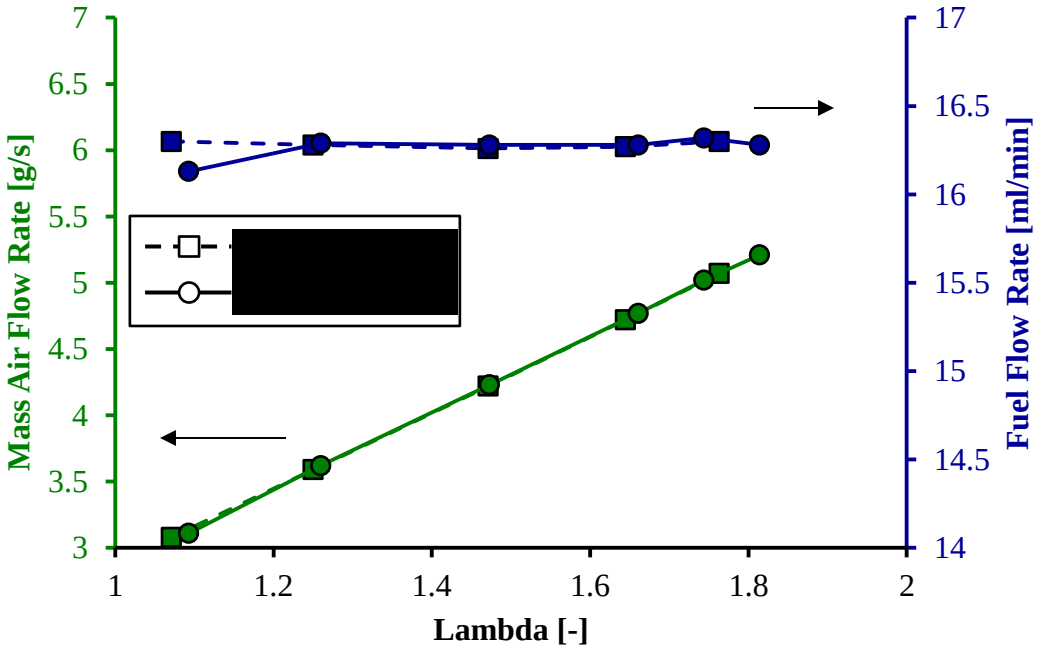

Figure 6-1: Mass Air and Average Fuel Flow Rate Results - Low Load Engine Tests

An overall summary of the engine tests with and without the insert are shown in Figure 6-2. Initially, there was no significant difference in the IMEP for an excess air ratio (denoted by the symbol λ) of 1 to 1.4. When the air/fuel ratio was increased further,

without the insert, there was a slight drop in load at λ=1.6, and a significant drop in the load at λ=1.8.

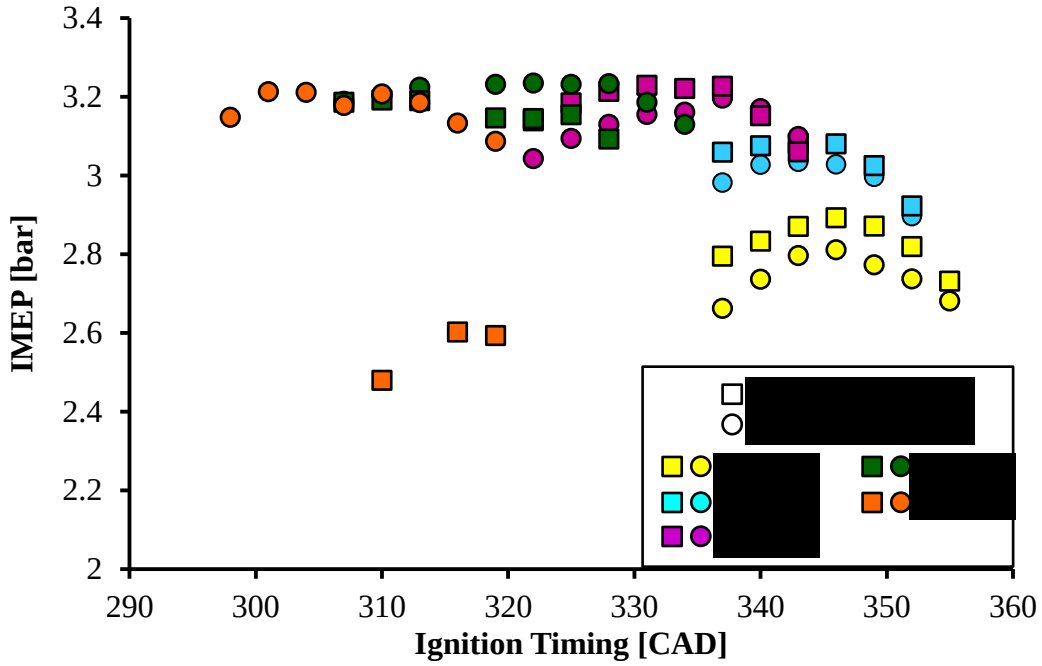

Figure 6-2: Overview of Low Load Engine Tests

From the data above, the MBT timing data points at the different lambda values were collected and analyzed. Figure 6-3: shows the results of the IMEP and the COV_{IMEP} for the MBT timing.

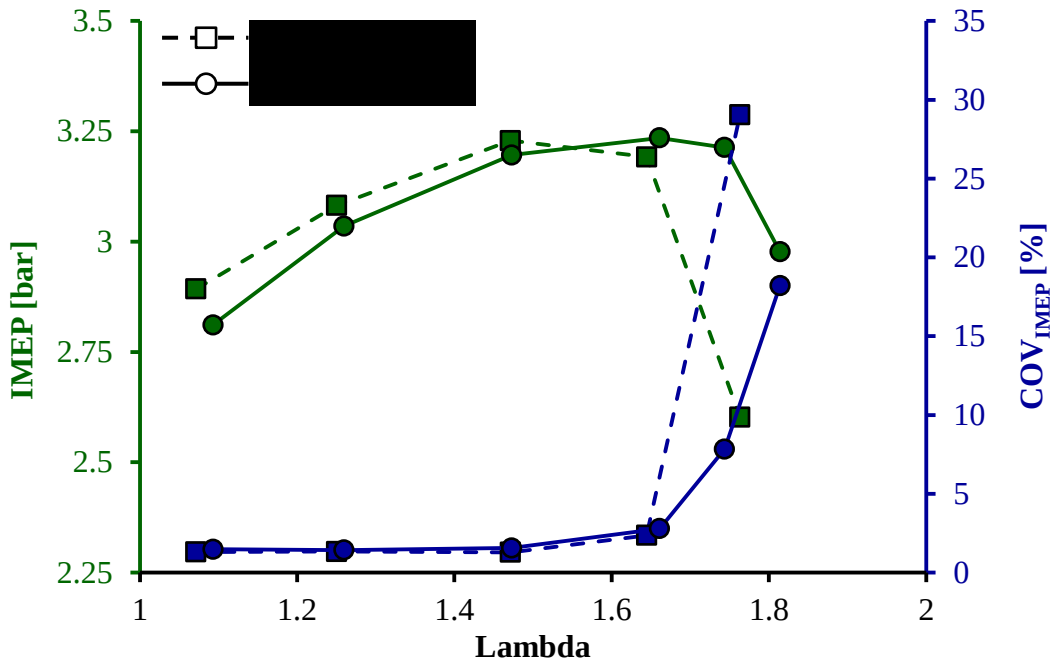

Figure 6-3: Low Load Engine Test MBT Results – Baseline and Enhanced Swirl

At the low load conditions, it was observed that there was no significant difference in the IMEP and COV_{IMEP} until λ=1.7. Beyond λ=1.7, the IMEP dropped significantly without the insert. The COV_{IMEP} also increased significantly, to approximately 30%, at this excess air ratio. However, with the insert, the IMEP was maintained and a lower COV_{IMEP} was produced at λ of 1.7 and above.

Figure 6-4 shows the effect of swirl enhancement on the combustion timing at different excess air ratios at low load. It is shown that the ignition delay was consistently lower with the insert throughout the lambda sweep with the maximum of 8°CA difference with respect to the without insert case at λ of approximately 1.6. The combustion duration was also decreased which indicated that the increased swirl motion increased the mixing and flame propagation speed which resulted in a faster, more

complete combustion. This also indicated by the emission data shown in Figure 6 -5 through Figure 6-7.

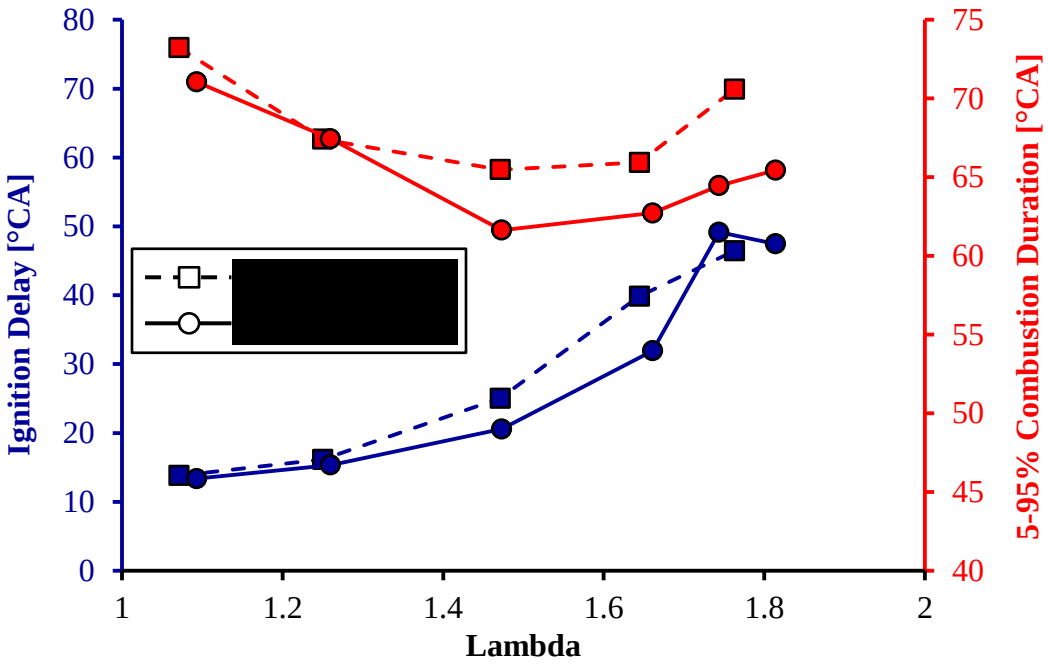

Figure 6-4: Effect of Swirl Enhancement on Combustion Duration at Low Load

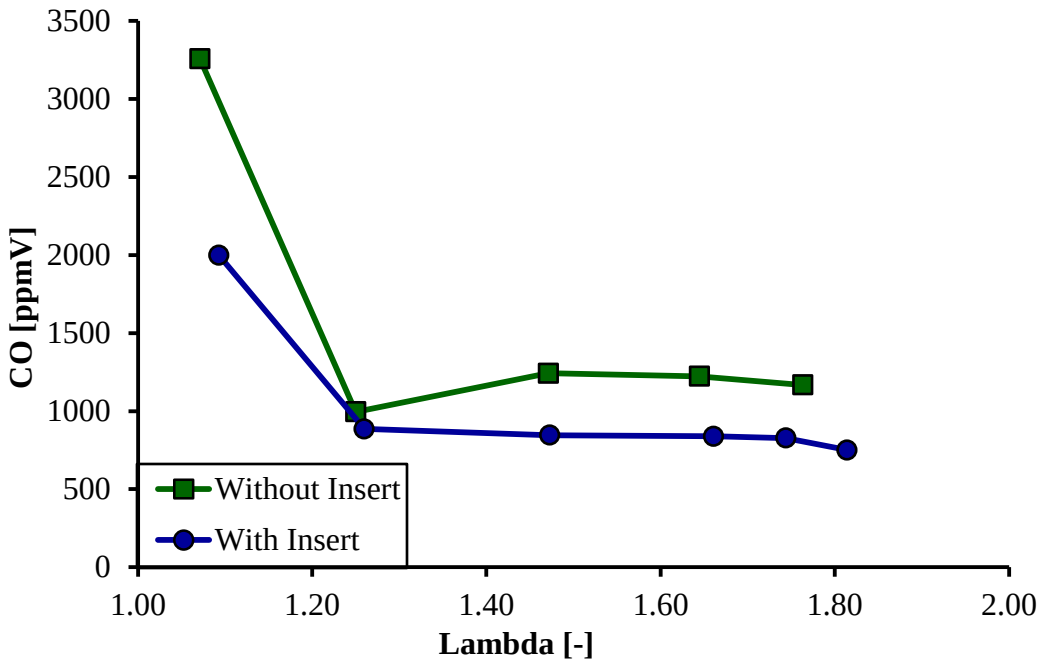

Figure 6 -5: Effect of Enhanced Swirl on CO Emissions at Low Load

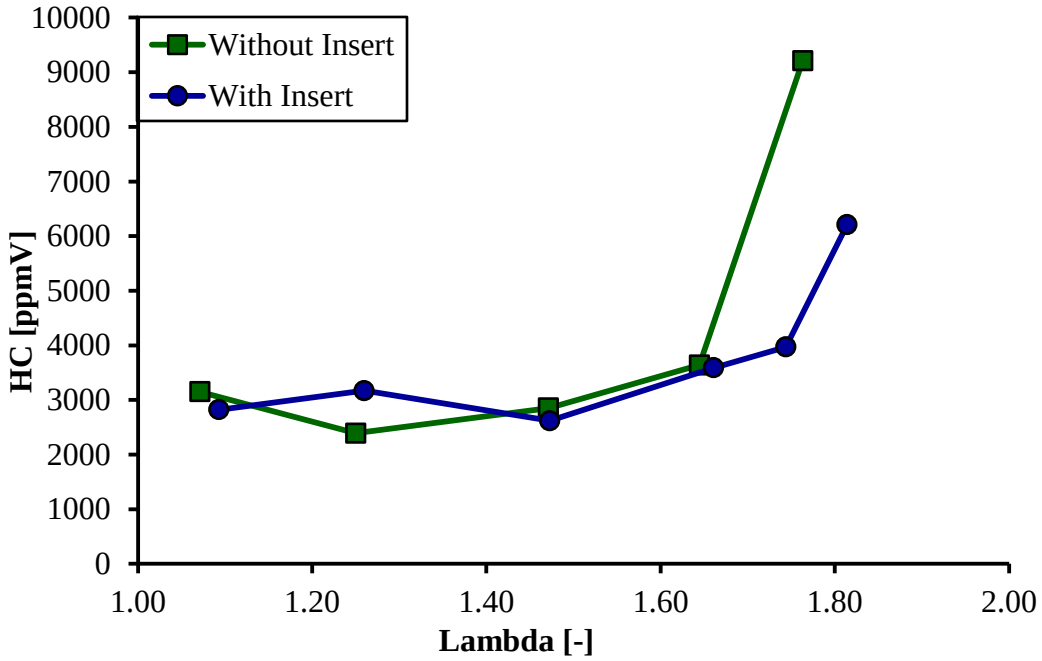

Figure 6-6: Effect of Enhanced Swirl on HC Emissions at Low Load

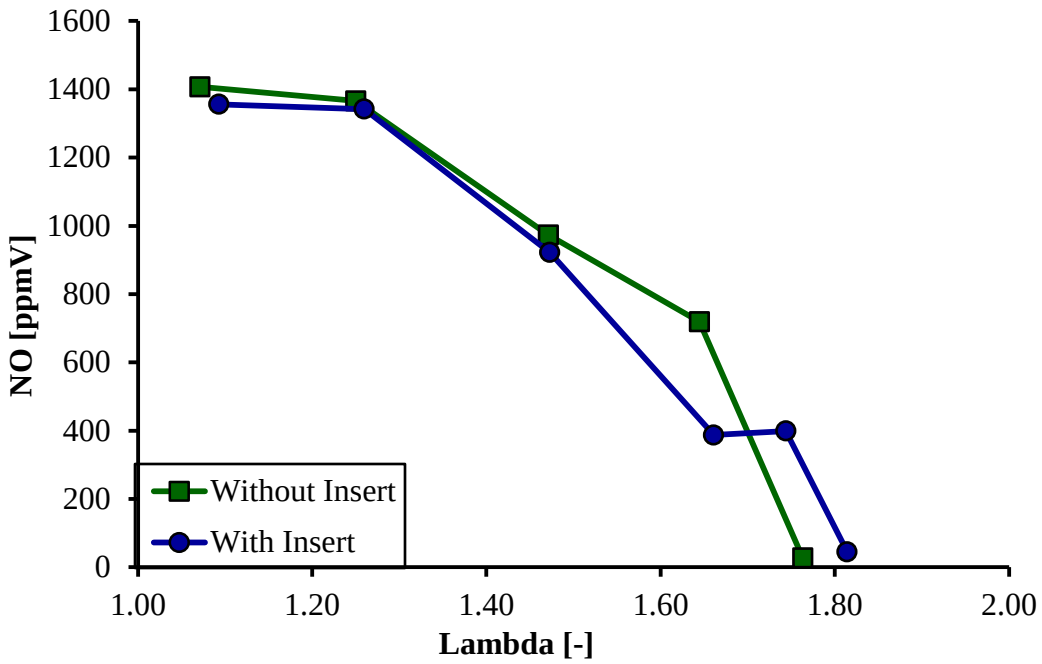

Figure 6-7: Effect of Enhanced Swirl on NO_x Emissions at Low Load

From the emission data in Figure 6 -5, it was shown that at each excess air ratio, the CO emission results of the insert were much lower than the baseline. At λ=1, the reduction was more than 38% with the increased swirl. However, as the dilution level was increased to give an equivalent excess air ratio of λ=1.25, the difference in the concentration of CO with the introduction of increased swirl was much less. Nevertheless, as the charge was made leaner (λ = 1.5 - 1.7), the reduction in the CO emission remained at around 30%. This reduction could be attributed to the increased mixing of the in-cylinder charge, reducing the fuel rich regions and increasing the oxidation of CO into CO_2 [49]. A similar trend was observed in [34], where a large initial decrease in CO emissions was observed followed by similar concentrations at λ = 1.2, and further decreases for λ > 1.3 with increased in-cylinder air motion.

The THC emission concentrations for both cases showed similar trends with initially higher THC concentrations at λ=1, followed by a slight decrease as the excess air ratio was increased (λ=1.25 – λ=1.5), and an eventual increase for leaner conditions. The increased swirl could have helped to oxidize the hydrocarbons at λ = 1 and λ = 1.5 - 1.7 indicated by the lower THC emission of the insert cases. The largest difference was observed at λ = 1.7, with a 56% reduction in the THC concentration. This reduction was mainly due to the combustion instability experienced at that λ without the insert, indicating that the cycles misfired. In addition, as the excess air ratio was increased, the combustion temperature was lowered, which was a favorable condition for the formation of HC emissions. However, the increased intake swirl showed the ability to produce a more stable combustion at λ=1.7 (COV of ~ 7% compared to ~30%) with a large reduction in the HC emission.

The NOx emissions were greatest at λ=1 and continued to decrease as the mixture became leaner and the maximum combustion temperature reduced. The concentrations were similar at the two different levels of swirl except at λ=1.7, where the combustion was unstable for the case without the insert. It was expected that the higher level of swirl would see an increase in the NOx emissions due to the higher combustion temperatures caused by the increased combustion rate. However, others factors such as heat transfer, may have caused a decrease in the in-cylinder temperature thereby reducing the NOx generation [51].

6.2 Engine Test Results - High Load with Enhanced Swirl

Tests were conducted on the single cylinder research engine similar to the low load tests with increasing levels of dilution. A target IMEP of approximately 6.5 – 7 bar was sought as the excess air ratio (λ) was increased. The mass flow rates for the tests conducted with the enhanced swirl were set to the same as the baseline measurements without the insert. The mass flow rate was maintained by supplying higher intake boost pressures via the compressed air supply. The fuel flow rate was also maintained similarly. The results of the mass flow and fuel flow rates for the two different tests are shown in Figure 6-8**.**

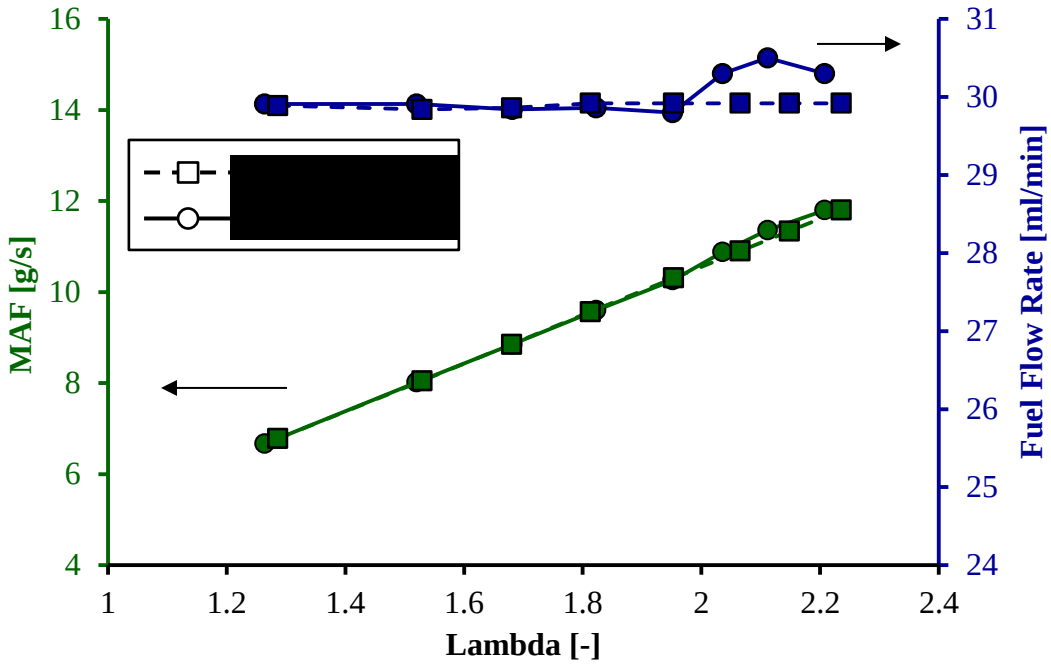

Figure 6-8: Mass Air and Average Fuel Flow Rate Results - High Load Engine Tests

The high load engine test conditions are provided in Table 6-2**.** The engine speed was maintained at 1300 rpm for all tests conducted. As shown in Figure 6-8, the fuel flow

rate and injection duration were maintained as the throttle valve opening and boost pressure were increased to increase overall air-fuel equivalence ratio. A spark timing sweep was performed at every excess air ratio to obtain the timing which produced the maximum brake torque (MBT). Similar to the low load tests, the spark ignition timing was advanced until either the knock limit was noticed or the COV_{IMEP} was increased and retarded until there was a substantial drop in the engine load and a high level of COV_{IMEP} was reached.

Table 6-2: High Load Engine Test Conditions

IMEP	[bar]	~6-7
Engine Speed	[rpm]	1300
Start of Injection	°CA	
Spark Timing	°CA	Sweep
Ignition Charging Duration	[ms]	5
Lambda	[-]	Sweep (1.2-2.2)

An overview of the baseline and enhanced swirl engine tests are shown in Figure 6-9. The IMEP and corresponding spark timings are shown at different lambda values.

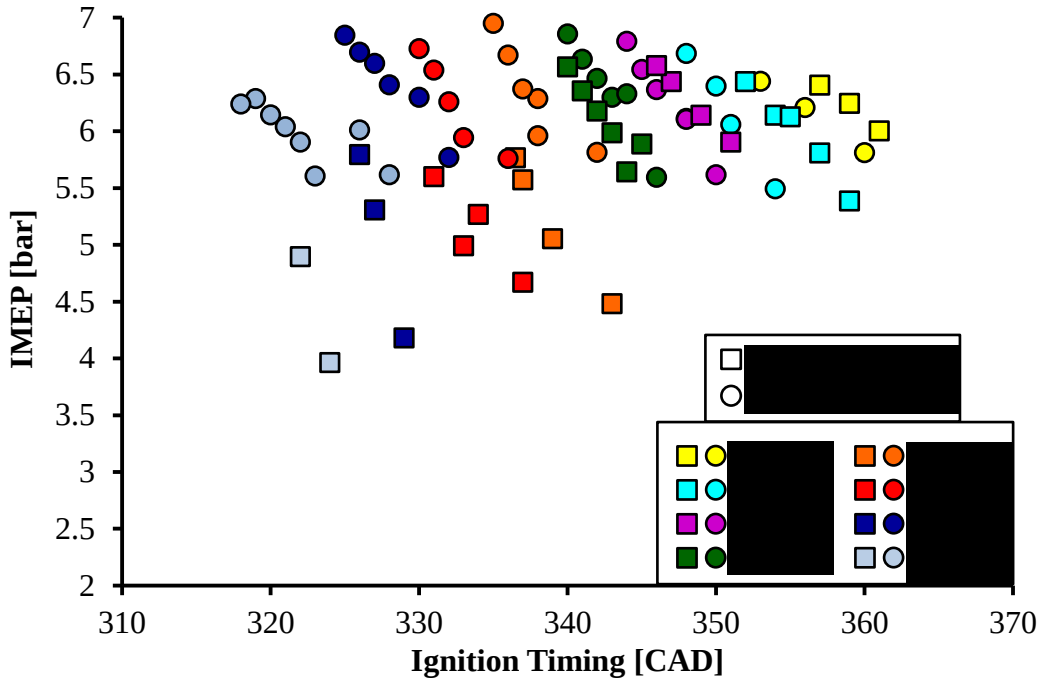

Figure 6-9: Overview of High Load Engine Tests

A preliminary indication from the high load engine tests was that with the enhanced swirl, a higher load level could be maintained even as the charge dilution was increased. This was especially true for the cases with the same ignition timings. Figure 6-10 illustrates the comparison of the MBT data points from the baseline and enhanced swirl test results at the different levels of charge dilution.

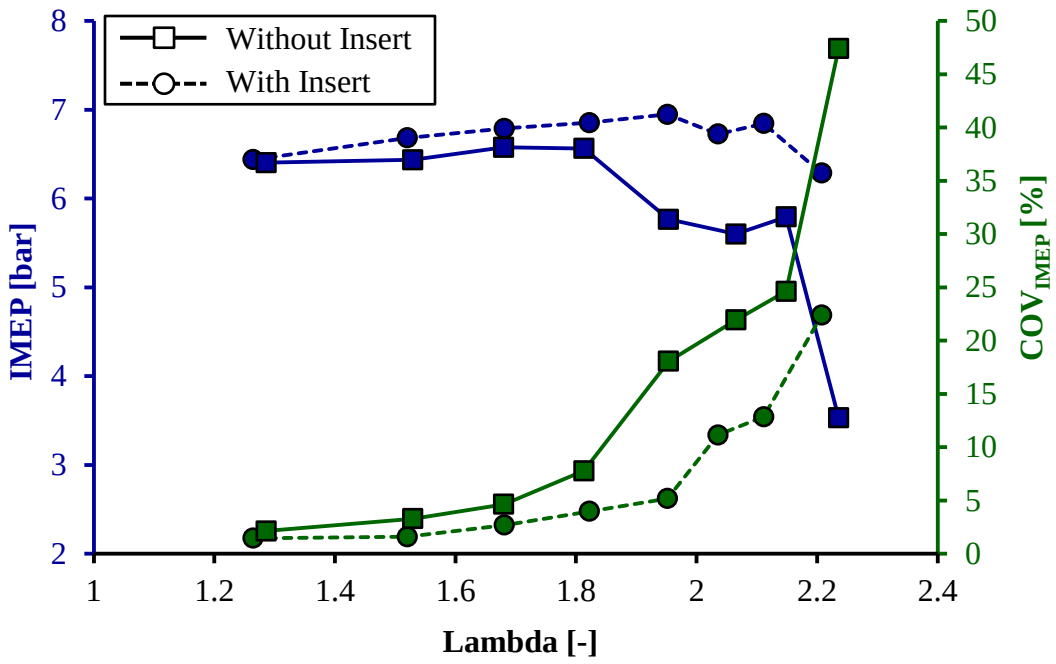

Figure 6-10: High Load MBT Results – Baseline and Enhanced Swirl

The results with the enhanced swirl showed a more stable IMEP across all excess air ratios. The trend showed an initial increase of up to λ=1.95, where a maximum load of 6.95 bar IMEP was produced, followed by a slight decrease until reaching a minimum of 6.29 bar at λ=2.2. The baseline results showed a maximum IMEP of 6.58 bar at λ=1.68 and the trend then decreased for further increases in the dilution level. In addition to the increase and sustainment of the IMEP, the cycle-to-cycle variations were consistently lower than the baseline results indicated by the COV_{IMEP}. For both cases, the COV_{IMEP} progressively increased as the lambda was increased. However, the COV_{IMEP} of the baseline increased very sharply to 18% at λ=1.9 while the swirl enhanced result still remains at an acceptable 5%. The cycle-to-cycle variations continued to increase at λ>2, although the variability was approximately half that of the baseline. Thus, the results in Figure 6-10 indicated that the enhanced swirl could help retain the engine load

and assist in lowering the cycle-to-cycle variations by increasing the mixing and flame propagation of highly diluted charges.

To further investigate the effect of the enhanced swirl, the combustion timing and phasing of the MBT data points were analyzed. The combustion duration, defined as the crank angle between when 10% to 90% (CA10 – CA90) of the mass fraction of fuel is burned, is presented in Figure 6-11.

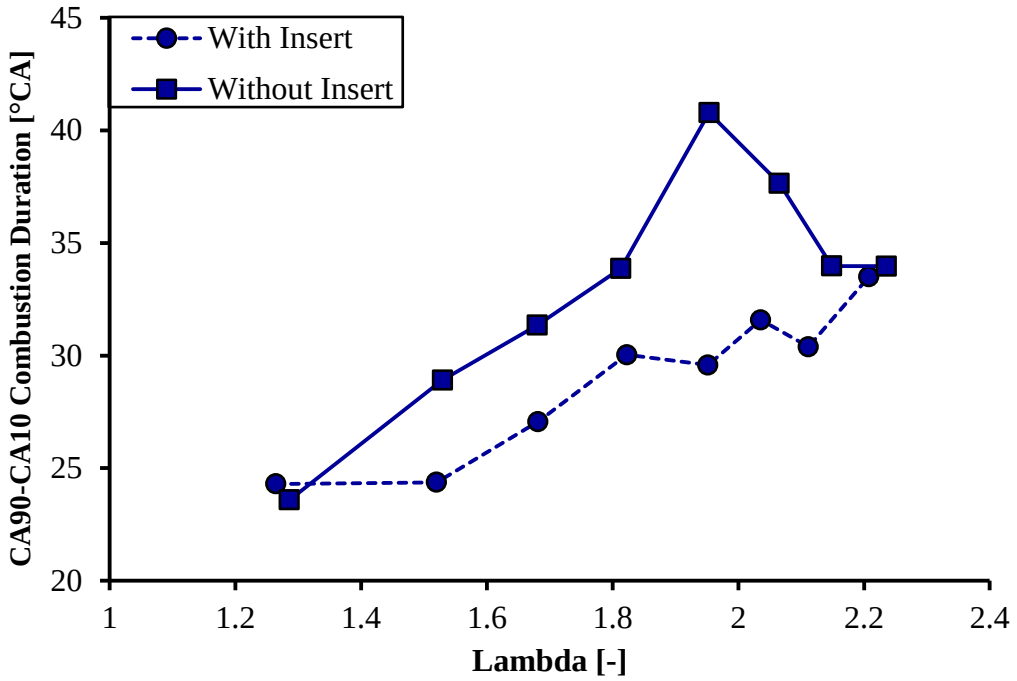

Figure 6-11: Effect on Enhanced Swirl on the Combustion Duration with Different Excess Air Ratios

The combustion duration increased as the dilution level was increased for both the baseline and the enhanced swirl cases. The combustion durations for all excess air ratios were reduced with the enhanced swirl. A negligible difference in the combustion duration at λ=1.25 was noticed for the enhanced swirl. However, as the mixture became leaner, the

enhanced swirl decreased the combustion duration with respect to the baseline almost linearly up to λ=1.8. The combustion with the enhanced swirl achieved a maximum reduction in the combustion duration at λ=1.95 of more than 11.3 °CA. As the dilution level was further increased, the combustion duration began to decrease for the baseline engine results. The decrease in the combustion duration at this excessively lean condition was probably caused by the extinguishing or quenching of the flame front which resulted in incomplete combustion. As a result, the combustion duration for the baseline results was decreased as the combustion efficiency decreased.

The THC emission results are displayed on Figure 6-12, which highlights the combustion inefficiency of the baseline results. The HC emissions from the enhanced swirl were consistently lower than the baseline for λ>1.7. This indicated that the increased swirl assisted the more complete combustion of the fuel when the air to fuel equivalence ratio was increased; and as a result, the engine load level was maintained (shown earlier in Figure 6-10) caused by the increased mixing and increased flame speed.

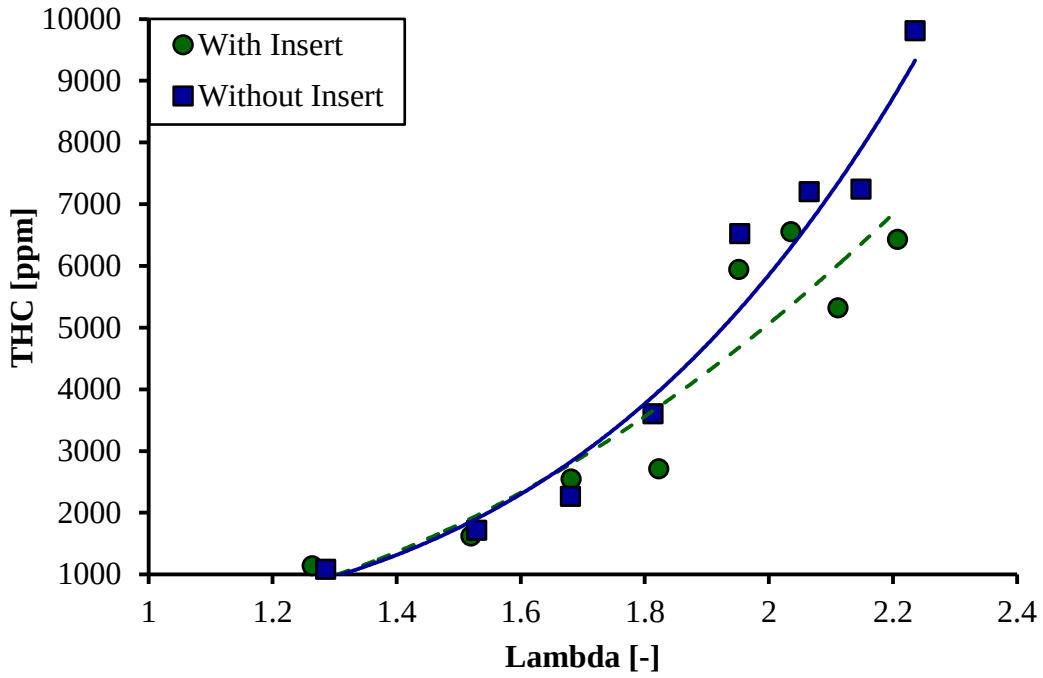

Figure 6-12: Effect of Enhanced Swirl and Excess Air Ratio on HC Emissions

To further investigate the effect of enhanced swirl on the combustion characteristics, the in-cylinder pressure and heat release rate were examined. Figure 6-13 & Figure 6-14 show the results of the MBT timing of the enhanced swirl that produced the highest engine load and the baseline results at λ=1.95. The comparison of the other MBT data points at different excess air ratios can be found in Appendix D. As shown in Figure 6-13, the enhanced swirl advanced and increased the total heat release rate (HRR). This enhanced swirl motion in the cylinder could lead to an increase in the in-cylinder turbulence intensity. As a result, the flame speed would increase which could explain the increase in the HRR and the cylinder pressure.

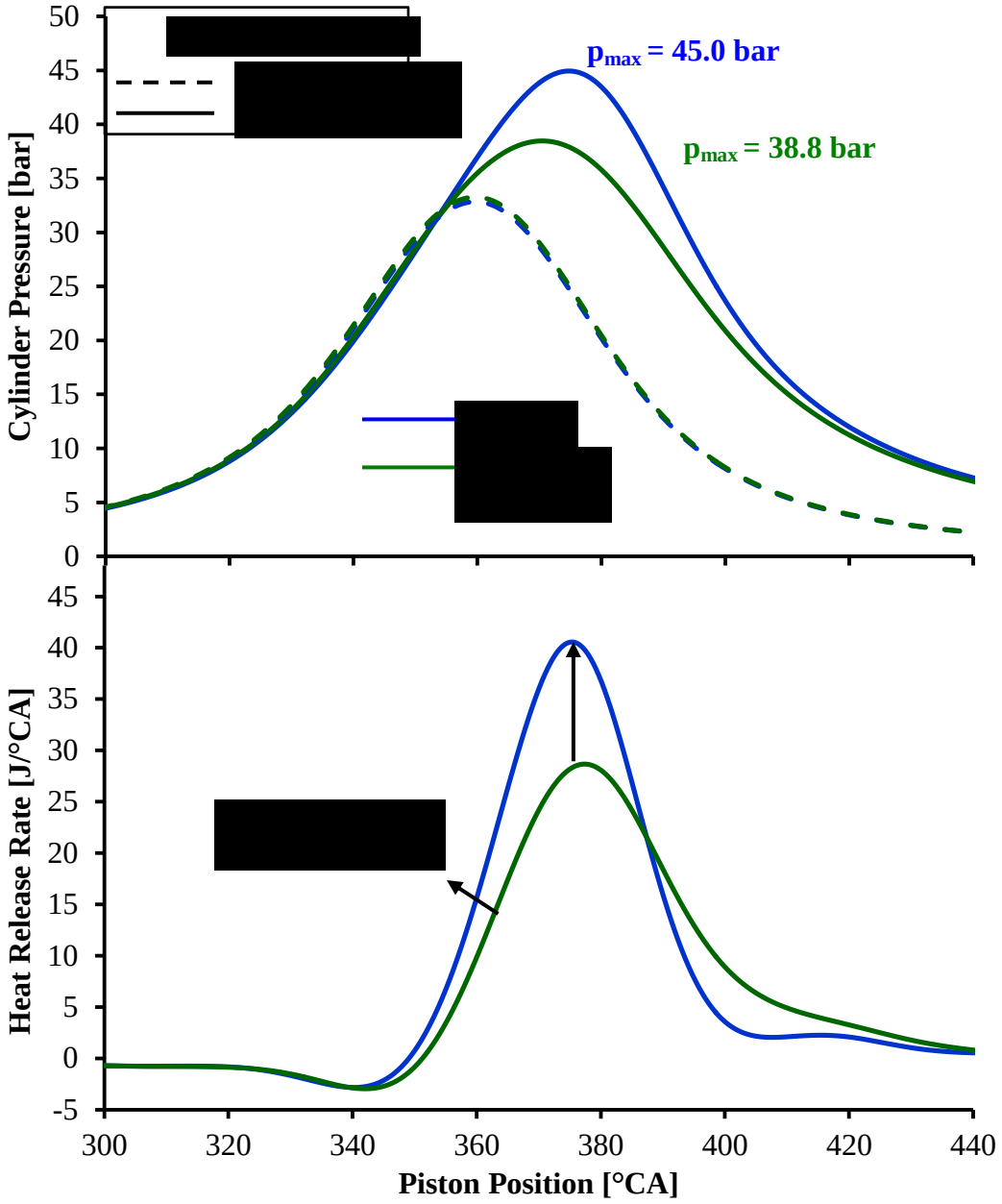

Figure 6-13: Effect of Enhanced Swirl on In-Cylinder Pressure and Heat Release Rate at $\lambda = 1.95$

The mass fraction burned (MFB) is shown in Figure 6-14 as a function of crank angle. The enhanced swirl showed a much steeper increase in the rate that the fuel energy

was released. This was true across all excess air ratios and is illustrated in Figure D-3 in Appendix D, shown by a decreased variation in the burning rate for the enhanced swirl. The increased burning rate enabled a decrease in the combustion duration (CA10-CA90) by 11.2° CA (27%).

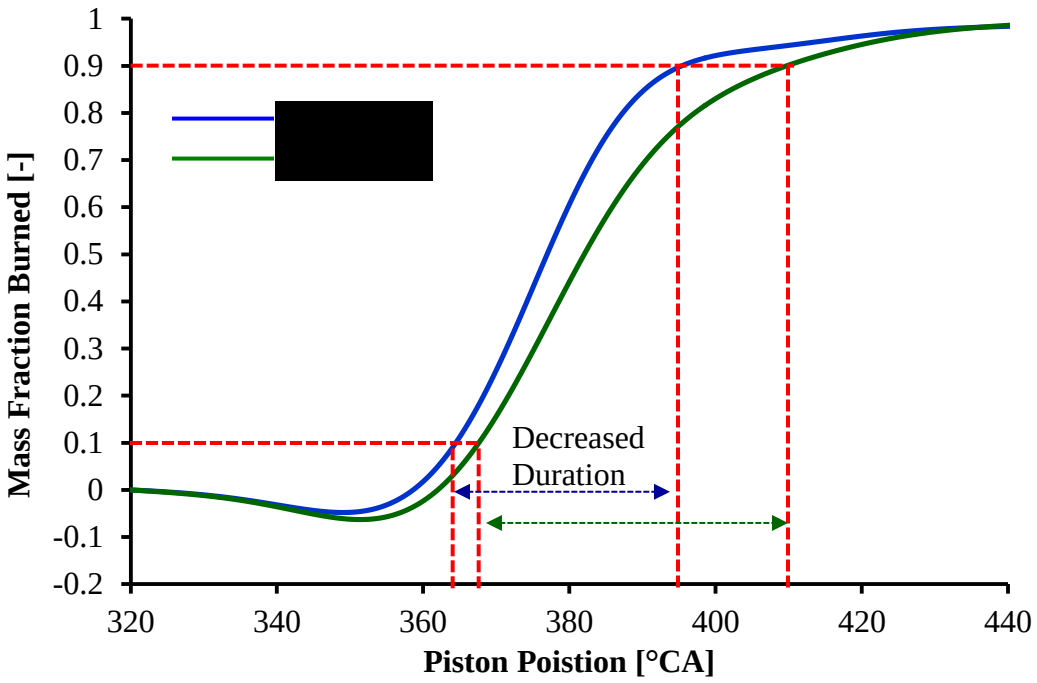

Figure 6-14: Effect of Enhanced Swirl on Combustion Speed at λ = 1.95

Figure 6-15 displays the effect of enhanced swirl on the indicated thermal efficiency. The thermal efficiency was calculated using Equation 6.2 and a lower heating value (LHV) of 43 MJ/kg was used for gasoline [45].

$$\eta_{thermal} = \frac{P_{ind}}{\dot{m}_{fuel}\, LHV} \qquad \text{Eqn 6.1}$$

where $\eta_{thermal}$ is the indicated thermal efficiency [-], P_{ind} is the indicated power [kW], $\dot{m}_{fuel}$ is the mass flow rate of fuel [kg/s], and *LHV* is the lower heating value of the fuel [kJ].

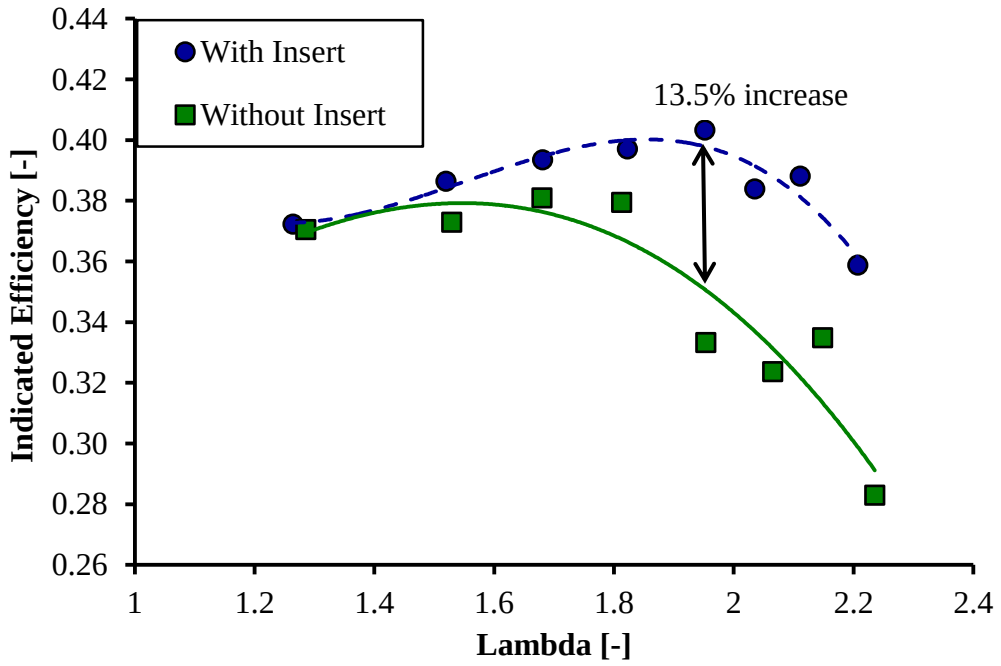

Figure 6-15: Effect of Enhanced Swirl on Indicated Thermal Efficiency at High Load

As can be seen from Figure 6-15, the enhanced swirl had the ability to increase the indicated thermal efficiency across all excess air ratios. As the excess air ratio was increased, from λ=1.2 up to λ=1.6, a slight increase in the thermal efficiency was noticed. A maximum thermal efficiency of 38.1% for the baseline condition occurred at λ=1.68. The increase in efficiency between 1.2>λ>1.95 was linear until reaching a maximum of 40.3% at λ=1.95 with the enhanced swirl. At leaner conditions (λ>1.95), the efficiency decreased, although at a reduced rate than the baseline. This was mainly caused by the combustion instability, indicated by the increased cycle-to-cycle variations.

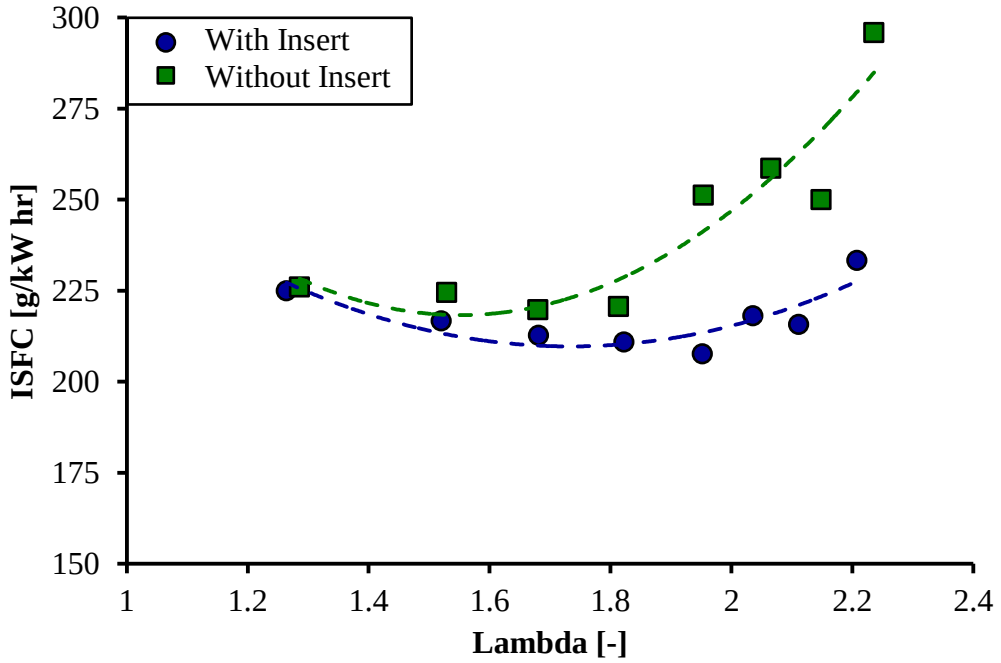

Figure 6-16: Effect of Enhanced Swirl on Indicated Specific Fuel Consumption

Figure 6-16 illustrates the effect of enhanced swirl on the indicated specific fuel consumption (ISFC). It was shown that the enhanced swirl had a major impact on the reduction in the specific fuel consumption. The largest reduction occurred at λ=1.95, that is a decrease in fuel consumption by more than 17% over the baseline. As the air dilution was increased further, the ISFC increased due to the poor combustion resulting from the unfavourable combustion conditions and slow flame speeds.

6.3 Chapter Summary of the Effect of Enhanced Swirl on Combustion

These engine tests demonstrated that the increased swirl noticed on the flow bench with the insert translated to an increase in performance when the excess air ratio of the cylinder charge was increased. For both load conditions, the mass air flow rate and

fueling rate for the tests conducted with the insert were matched to the corresponding baseline measurements.

The enhanced swirl was investigated at a constant engine load of approximately 3 bar IMEP. The increased swirl maintained the engine load beyond $\lambda > 1.6$ and significantly lowered the COV_{IMEP}. The CO emission concentrations were reduced throughout all excess air ratios. This indicated an increase in the combustion efficiency with the enhanced swirl. In addition, the combustion duration was lowered compared to the baseline results.

The effect of the enhanced swirl was investigated at a higher engine load of approximately 6 bar IMEP. At $\lambda = 1.95$, the increased swirl enabled a load of 6.95 bar IMEP with a COV_{IMEP} of 5% in contrast to the baseline result of 5.77 bar IMEP and a COV_{IMEP} of over 18%. A lowered THC emission was achieved with the increased swirl; especially as the dilution level was increased, indicating that the combustion efficiency was improved by the increased oxidation of hydrocarbons. Further analysis of the cylinder pressure curves was conducted. It was found that the maximum cylinder pressure was increased with the enhanced swirl. This could be caused by the increased flame speed and as a result the heat release rate was increased. This was noticed for all air-fuel equivalence ratios indicated in Figure D-1 in Appendix D. Overall, an increase in the indicated thermal efficiency was achieved. The largest improvement occurred at $\lambda = 1.95$ producing an efficiency of 40.3%. Finally, the fuel consumption was compared which showed that the overall trend decreased the indicated specific fuel consumption with enhanced swirl until the cycle-to-cycle variations increased and misfire occurred.

CHAPTER 7: CONCLUSION AND FUTURE WORK

In this chapter, a summary of the results achieved throughout this research work are presented. Recommendations for future work are also provided for the continuation of this research.

7.1 Summary of Results

A steady-state flow bench system was developed and used to conduct tests to investigate the air motion, specifically swirl motion, produced by the intake port geometry of a two-valve single-cylinder engine. The swirl speed measurements were obtained from a vane-type swirl meter developed in-house. Flow bench tests provided a baseline measurement of the swirl ratio generated by the intake port. An intake generated swirl ratio of 1.34 was determined from the baseline measurements.

A mold of the intake port was cast and 3D scanned to obtain a geometrically correct model for a three dimensional CFD numerical model. The results from two different models were compared with experimental test results and the model with the finer grid appeared to show a more similar trend. The finer meshed model was used for the evaluation of different geometries to increase the swirl. Simulation results indicated that the helically shaped insert produced the largest increase in swirl speed and was selected for manufacturing. The helical insert was tested on the flow bench to determine the increase in swirl speed and new swirl ratio. The insert proved to increase the swirl ratio from 1.35 to 1.54, a 14% increase in the overall intake generated swirl ratio. Engine tests were conducted incorporating the insert to increase the swirl motion. A combustion analysis was completed to investigate the effects of increase swirl motion on diluted

combustion. The results showed that the COV was decreased at both low and high loads. The hydrocarbon emissions were also decreased, indicating that the combustion was more complete. A combustion efficiency analysis was performed which showed that the case with the increased swirl exhibited higher efficiency. Analysis of the pressure curves for the MBT between the two cases show an advanced combustion phasing with the insert. The increase in swirl shows some advantage for lean-burning combustion.

7.2 **Recommendations for Future Work**

The following are recommendations for the continuation and pursuance of future work related to this research:

- The performance of the vane-type swirl meter should be investigated due to the associated disadvantages of this type of device for the measurement of swirl. An impulse-torque swirl meter, which incorporates a flow straightening device, can be used to measure the angular momentum at the same positioning as the vane-type swirl meter to determine the possible benefits of using this device for swirl measurement.
- Measurements of tumble air motion, which is the rotational air motion about an axis perpendicular to the cylinder axis, should be made to determine if there are any changes with the use of the insert. This investigation would provide further insight into the change in air motion influenced by the insert.
- Higher test pressures for the steady flow measurements of swirl should be used to investigate the effect on the flow parameters and resulting swirl ratio value.

- Particle Image Velocimetry (PIV) tests should be conducted to obtain the velocity in different planes within the cylinder. This would add an additional method of comparison with the CFD results for further model validation. The swirl speed can also be analyzed through PIV tests, as a less intrusive investigation and compared with the swirl meter results.
- Further engine tests should be conducted with and without the insert incorporating a regular, single pole, spark plug to differentiate the benefit of the insert and three-pole spark plug. Investigations should be made to determine the effect of the air motion and ignition system separately.
- Furthermore, an optical access window into the combustion chamber along with high-speed imaging would provide further insight into the effect of the air motion on the combustion process by providing a visual aspect on the in-cylinder combustion.

REFERENCES

1. Heywood, J.B., “Internal Combustion Engine Fundamentals”, McGraw-Hill Co, Singapore, ISBN 13: 9780070286375, 1988.
2. Diesel, R., “Method of and Apparatus for Converting Heat into Work”, U.S. Patent 524846, July 16, 1895.
3. European Automobile Manufacturers Association, “Share of Diesel in New Passenger Cars”, http://www.acea.be/statistics/tag/category/share-of-diesel-in-new-passenger-cars, 2016, Accessed: 5 February, 2017.
4. European Environment Agency, “Nominal and Real Fuel Prices – Transport”, https://www.eea.europa.eu/data-and-maps/daviz/nominal-and-real-fuel-prices-3#tab-chart_1, 2016, Accessed: 15 May, 2017.
5. U.S. Energy Information Administration, “Short-Term Energy Outlook – Real Prices”, https://www.eia.gov/outlooks/steo/realprices/, 2017, Accessed: 10 May, 2017.
6. United States Department of Transportation - Bureau of Transportation Statistics, “BTS Fact Sheets – 2015 Diesel-Powered Passenger Cars and Light Trucks”, http://www.rita.dot.gov/bts/sites/rita.dot.gov.bts/files/publications/bts_fact_sheets/oct_2015/html/figure_01.html, 2015, Accessed: 7 February, 2017.
7. United States Environmental Protection Agency, “NO_x – How Nitrogen Oxides Affect the Way We Live and Breathe”, EPA-456/F-98-005,1998.
8. United States Department of Transportation - Bureau of Transportation Statistics – Table 4-23, “Average Fuel Efficiency of U.S. Light Duty Vehicles (April 2017)”,

https://www.rita.dot.gov/bts/sites/rita.dot.gov.bts/files/publications/national_transportation_statistics/html/table_04_23.html, 2017, Accessed: 6 May, 2017.

9. United States Environmental Protection Agency, "EPA Emission Standards for Light-Duty Vehicles and Trucks", https://www.epa.gov/emission-standards-reference-guide/epa-emission-standards-light-duty-vehicles-and-trucks, 2016, Accessed: 15 February, 2017.
10. U.S. National Traffic Highway Traffic Safety Administration – Laws and Regulations, "Corporate Average Fuel Economy", https://www.nhtsa.gov/laws-regulations/corporate-average-fuel-economy, 2016, Accessed: 18 May, 2017.
11. Wang, Z., Liu, H., Song, T., Qi, Y. et al., "Relationship Between Super-Knock and Pre-Ignition", International Journal of Engine Research, 16 (8): pp. 166-180, 2014.
12. Takahashi, D., Nakata, K., Yoshihara, Y., Ohta, Y. et al., "Combustion Development to Achieve Engine Thermal Efficiency of 40% for Hybrid Vehicles", SAE Technical Paper 2015-01-1254, 2015.
13. Ceviz, M. A., Kaymaz, I., "Temperature and Air-Fuel Ratio Dependent Specific Heat Ratio Functions for Lean Burned and Unburned Mixture", Energy Conversion and Management, 46 (15-16): pp. 2387-2404, 2005.
14. Kang, K., Reitz, R., "The Effect of Intake Valve Alignment on Swirl Generation in a DI Diesel Engine", Experimental Thermal and Fluid Science, 20, pp. 94-103, 1999.
15. Heim, D. M., Ghandi, J. B., "Investigation of Swirl Meter Performance", Proceedings of the Institution of Mechanical Engineers, Part D: Journal of Automobile Engineering, 225 (8): 1067-1077, 2011.

16. Stone, R., “Introduction to Internal Combustion Engines”, SAE International, Warrendale, PA, ISBN-13: 9780768020847, 2012.
17. Alcock, J., “Air Swirl in Oil Engines”, Proceedings of the Institution of Mechanical Engineers, 128 (1): 123-193, June 1934.
18. Fitzgeorge, D., Allison, J. L., “Air Swirl in a Road-Vehicle Diesel Engine”, Proceedings of the Institution of Mechanical Engineers, 16 (1): pp. 151-177, 1962.
19. Stone, C. R., Labommatos, N., “The Measurement and Analysis of Swirl in Steady Flow”, SAE Technical Paper 921642, 1992.
20. Sun, Z., Li, X., Du, W., “Research on Swirler for Intake Induced Swirl in DI Diesel Engine”, International Conference on Digital Manufacturing and Automation, 2010.
21. Kawashima, J., Ogawa, H., Tsuru, Y., “Research on a Variable Swirl Intake Port for 4-Valve High-Speed DI Diesel Engines”, SAE Technical Paper 982680, 1998.
22. Gale, N., “Diesel Engine Cylinder Head Design: The Compromises and the Techniques”, SAE Technical Paper 900133, 1990.
23. Tippelmann, G., “A New Method of Investigation of Swirl Ports”, SAE Technical Paper 770404, 1977.
24. Hill, P. G., Zhang, D., “The Effects of Swirl and Tumble on Combustion in Spark Ignition Engines”, Progress in Energy and Combustion Science, Vol 20 (5): pp. 373-429, 1994.
25. Nordgren, H., Hildingsson, L., Johansson, B., et al., “Comparison Between In-Cylinder PIV Measurements, CFD Simulations and Steady-Flow Impulse Torque Swirl Meter Measurements”, SAE Technical Paper 2003-01-3147, 2003.

26. Asad, U., Kumar, R., Han, X., Zheng, M., “Precise Instrumentation of a Diesel Single-Cylinder Research Engine”, Measurement, 44 7, pp. 1261-1278, 2011.
27. Zheng, M., Shui, Y., Tjong, J., “High Energy Multipole Distribution Spark Ignition System”, International Conference on Ignition Systems for Gasoline Engines, pp. 109-130, 2016.
28. Sevik, J., Wallner, T., Pamminger, M., et al “ Extending Lean and Exhaust Gas Recirculation-Dilute Operating Limits of a Modern Gasoline Direct-Injection Engine Using a Transient Plasma Ignition System”, Journal of Engineering for Gas Turbines and Power, 138 (11), 2016.
29. Xu, H., “Some Critical Technical Issues on the Steady Flow Testing of Cylinder Heads”, SAE Technical Paper 2001-01-1308, 2001.
30. Wang, T. Y., Peng, Z. Y., Wang, G. D., “In-Cylinder Air Motion Characteristics with Variable Valve Lift in a Spark Ignition Engine – Part1: Swirl Flow”, Proceedings of the Institution of Mechanical Engineers, Part D: Journal of Automobile Engineering, 225 (4): pp. 479-497, 2011.
31. Wei, H., Zhu, T., Shu, G., Tan, L., Wang, Y., “Gasoline Engine Exhaust Gas Recirculation – A Review”, Applied Energy 99, pp. 534-544, 2012, doi:10.1016/j.apenergy.2012.05.011.
32. Cha, J., Kwon, J., Cho, Y., Park, S., “The Effect of Exhaust Gas Recirculation (EGR) on Combustion Stability, Engine Performance and Exhaust Emissions in a Gasoline Engine”, KSME International Journal, 15 (10), pp. 1442-1450, 2001.

33. Xie, F., Hong, W., Su, Y., Zhang, M., et al., “Effect of External Hot EGR Dilution on Combustion, Performance and Particulate Emissions of a GDI Engine”, Energy Conversion and Management, 142, pp. 69-81, 2017.
34. Hacohen, J., Ashcroft, S. J., Belmont, M. R., “Lean Burn Versus EGR S.I. Engine”, SAE Technical Paper 951902, 1995.
35. Lumsden, G., Eddleston, D., Sykes, R., “Comparing Lean Burn and EGR”, SAE Technical Paper 970505, 1997.
36. Tang, Q., Liu, J., Zhan, Z., Hu, T., “Influences on Combustion Characteristics aand Performances of EGR vs. Lean Burn in a Gasoline Engine”, SAE Technical Paper 2013-01-1125, 2013.
37. Hill, P. G., Zhang, D., “The Effects of Swirl and Tumble on Combustion in Spark-Ignition Engines”, Progress in Energy and Combustion Science, 20 (5): pp. 373-429, 1994.
38. Whitelaw, J. H., Xu, H. M., “Cyclic Variations in a Lean-Burn Spark Ignition Engine Without and With Swirl”, SAE Technical Paper 950683, 1995.
39. Matsuki, M., Nakano, K., Amemiya, T., Tanabe, Y., et al., “Development of a Lean Burn Engine with a Variable Valve Timing Mechanism”, SAE Technical Paper 960583, 1996.
40. Todd, D., “DIY Flowbench Design”, DTec Devices
41. International Organization for Standardization, “ISO-5167 Standard, “Measurement of Fluid Flow by Means of Pressure Differential Devices Inserted in Circular Cross-Section Conduits Running Full – Part 1: General Principles and Requirements”, ISO 5167-1:2003, 2003.

42. Converge CFD, “ConvergeCFD Manual Series – Converge Manual 2.3”, 2016.

43. Converge CFD, “Converge CFD IC Engine Training Slides”, 2016.

44. Yang, X., Kuo, T., Guralp, O., Grover, R., et al., “In-Cylinder Flow Corrections Between Steady Flow Bench and Motored Engine Using Computational Fluid Dynamics”, Proceedings of the ASME Internal Combustion Engine Division 2016 Fall Technical Conference ICEF2016-9316, 2016, doi:10.1115/ICEF2016-9316.

45. Han, X., “Study of Fuels and Fuelling Strategies for Enabling Clean Combustion in Compression Ignition Engines”, a PhD Dissertation, Electronic Theses and Dissertations, University of Windsor, Paper Series 5103, 2014.

46. Asad, U., “Advanced Diagnostics, Control and Testing of Diesel Low Temperature Combustion”, a PhD Dissertation, University of Windsor, 2009.

47. Lancaster, D. R., Krieger, R. B., Lienesch, J. H., “Measurement and Analysis of Engine Pressure Data”, SAE Technical Paper 750026, 1975.

48. Asato, K., Miyasaka, T., Watanabe, Y., Tanabashi, K., “Combined Effects of Vortex Flow and the Shchelkin Spiral Dimensions on Characteristics of Deflagration-to-Detonation Transition”, Shock Waves, 23, pp. 325-335, 2013.

49. Kook, S., Bae, C., Miles, P., Choi, D., et al., “The Effect of Swirl Ratio and Fuel Injection Parameters on CO Emission and Fuel Conversion Efficiency for High-Dilution, Low-Temperature Combustion in an Automotive Diesel Engine”, SAE Technical Paper 2006-01-0197, 2006.

50. Pitcher, G. F., “An Investigation and Comparison Between Standard Steady Flow Measurements and Those in a Motored Engine”, a PhD Dissertation, Electronic

Theses and Dissertations, Loughborough University, https://dspace.lboro.ac.uk/2134/12576, 2011.

51. Olmeda, P., Martin, J., Blanco-Cavero, D., Warey, A., "Effect of In-Cylinder Swirl on Engine Efficiency and Heat Rejection in a Light-Duty Diesel Engine", International Journal of Engine Research, 18 (1-2), pp 81-92, 2017.

APPENDIX A: CALIBRATION OF DIGITAL PRESSURE SENSORS

The following shows the test results of the differential sensor calibration of both the orifice and port. A U-tube manometer filled with water and red coloured dye was used and the visual reading was recorded. The electronic signal from the pressure sensors were recorded in a LabVIEW program. The NXP USA MXPV7025 differential pressure sensors had a range of ±25 kPa which was more than suitable for this application. The figure below shows the test results of the pressure sensor and manometer readings. The valve lift was fixed while the mass flow rate was varied.

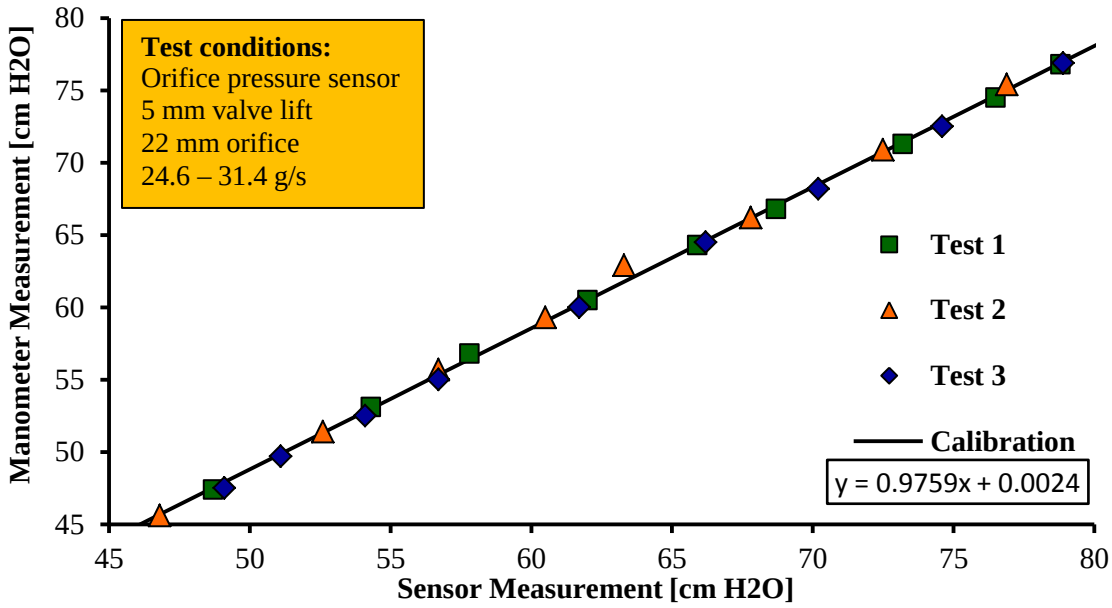

Figure A-1: Calibration Test of Orifice Pressure Sensor

The values of the line fit of all three tests were averaged and the resultant calibration equation line was input in the LabVIEW program to account for the correction

in the pressure readings. In a similar manner, the port pressure sensor was calibrated from the test data shown below.

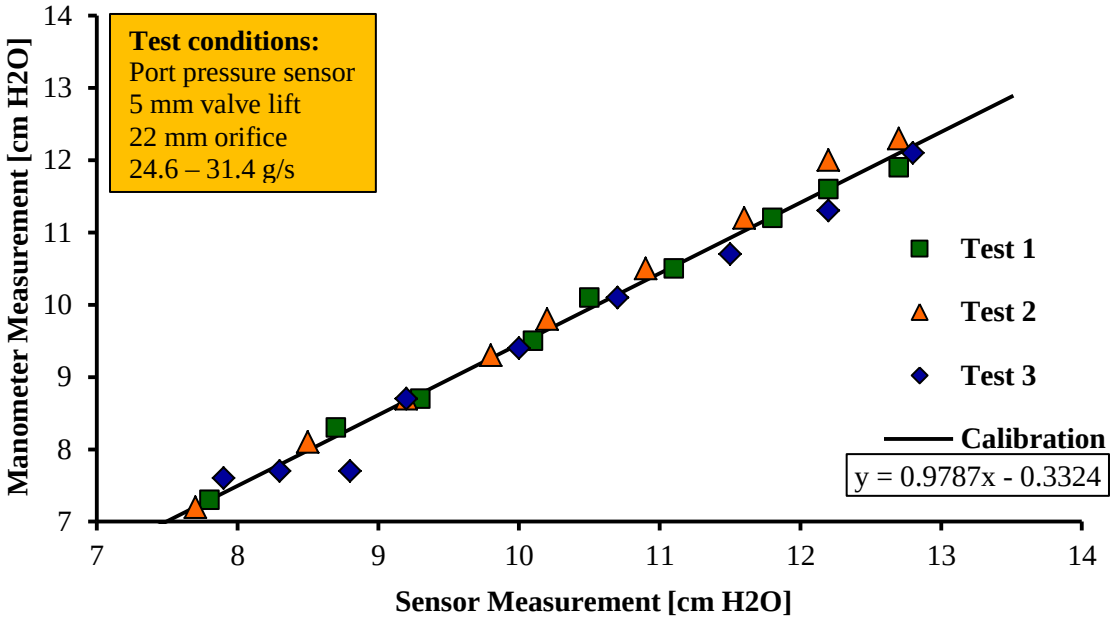

Figure A-2: Calibration Tests of Port Pressure Sensor

APPENDIX B: AIR BOX DESIGN AND FABRICATION

This section will discuss the air box design and fabrication outlining the materials and components. The design was inspired by the flow bench design guide found in [40].

The vacuum motors selected for the air box are the same models which are used for commercially available flow benches. The air box structure is made from ¾ inch medium density fiber board (MDF) and fastened together with wood glue and 2.5 inch # 10 screws. A chamfer was cut along the outside edges of the structure using a wood router in efforts to remove any shape edges and corners. A bead of silicon sealant was applied to all inside joints, shown in Figure B-1**,** in efforts to minimize the chances of internal leakage.

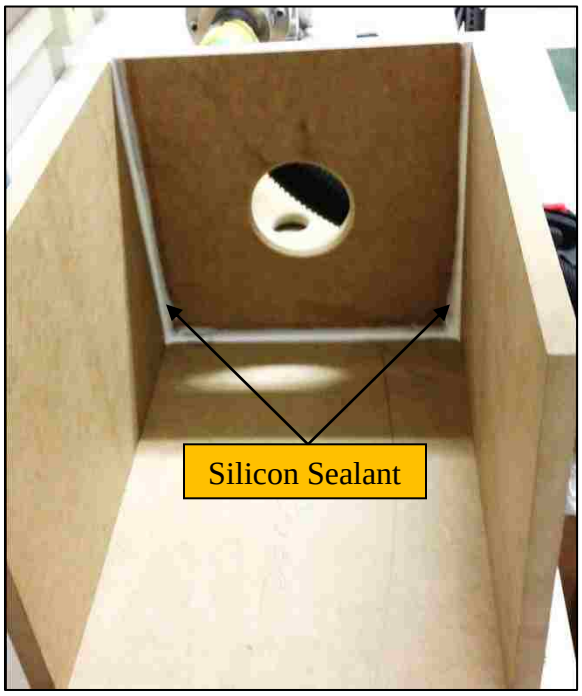

Figure B-1: Sealing of Air Box Joints

Four holes were, larger than the vacuum intake nozzle, were cut into the divider section of MDF. In order to ensure a smooth entry of air to the motors, a radius was cut into the edges of the holes as indicated in Figure B-2.

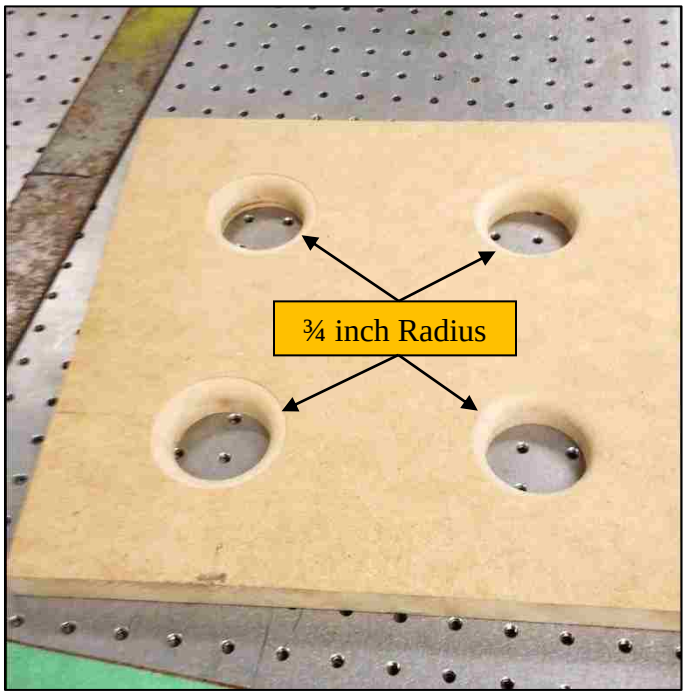

Figure B-2: Divider Board Inlet Entrance to Vacuum Motors

The vacuum motors were mounted to the divider board using an industrial strength two part epoxy. A hole was cut into the side of the box to allow the electrical wires to pass through then later sealed with silicon. The electrical wires were brought into an electrical junction box and connected to four switches; one for each motor. The current draw from an individual motor was measured at approximately 10 amps. Due to the electrical breaker limitation of 15 amps, a power cable was wired to each switch to enable the ability to use separate outlets.

For convenience, the top was made removable for inspection and was sealed using adhesive weather stripping. A 4 inch hole was cut into each end of the box for the air inlet and outlet. A 4 inch to 2 inch plumbing reducer was mounted on the outlet side for the connection to the approximate 2 inch inlet on the orifice flow meter. The final product is shown in Figure B-3.

Figure B-3: Air Box Assembly

APPENDIX C: SWIRL METER DESIGN

This section provides the detailed dimensions of the paddle wheel swirl meter design for this work. All components were fabricated in-house at the University of Windsor. The blade profile was cut on a wire EDM (Electrical Discharge Machine) which uses high voltage and current to cause a breakdown of the material. Due to the very thin wire and low residual stresses, very intricate geometries can be obtained. The overall geometry of the blade is detailed in Figure C-1. The diameter of the blade is approximately 88.6% the size of the bore.

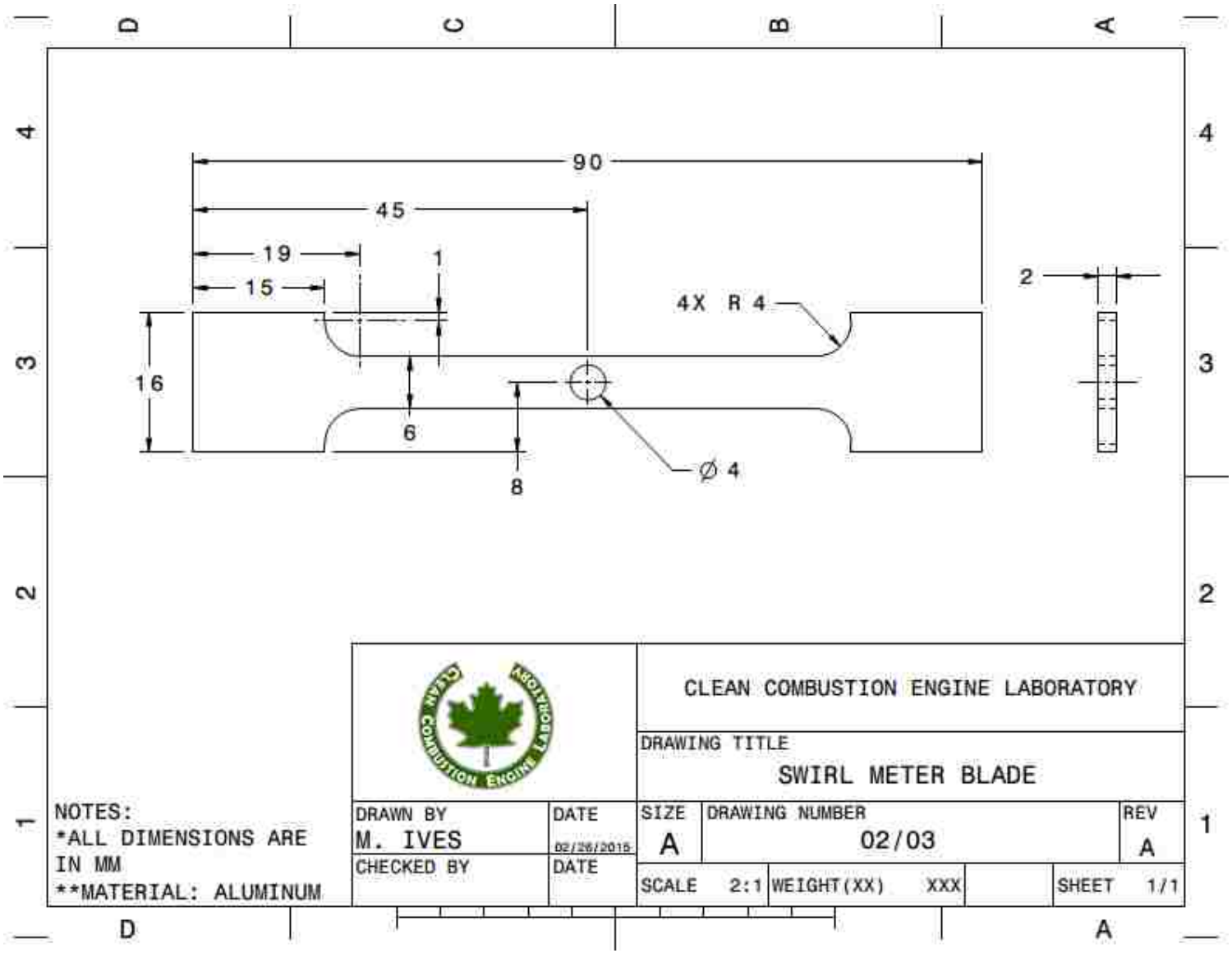

Figure C-1: Swirl Meter Blade Dimensions

APPENDIX D: PRESSURE, HRR AND MBF OF MBT TIMING AT HIGH LOAD

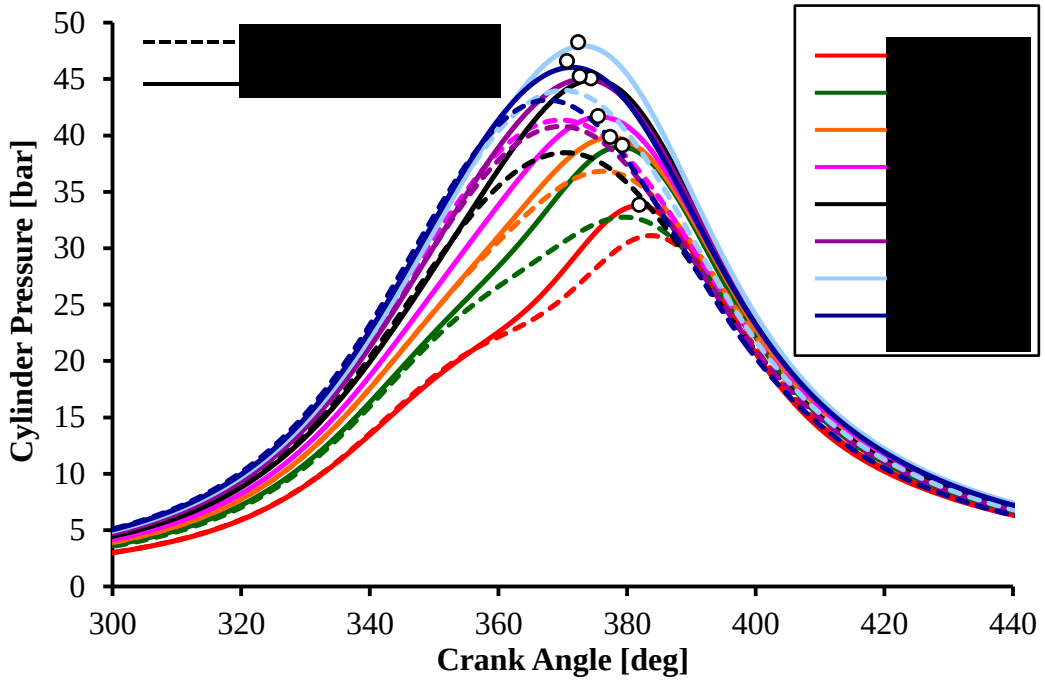

Figure D-1: Effect of Enhanced Swirl In-Cylinder Pressures at High Load

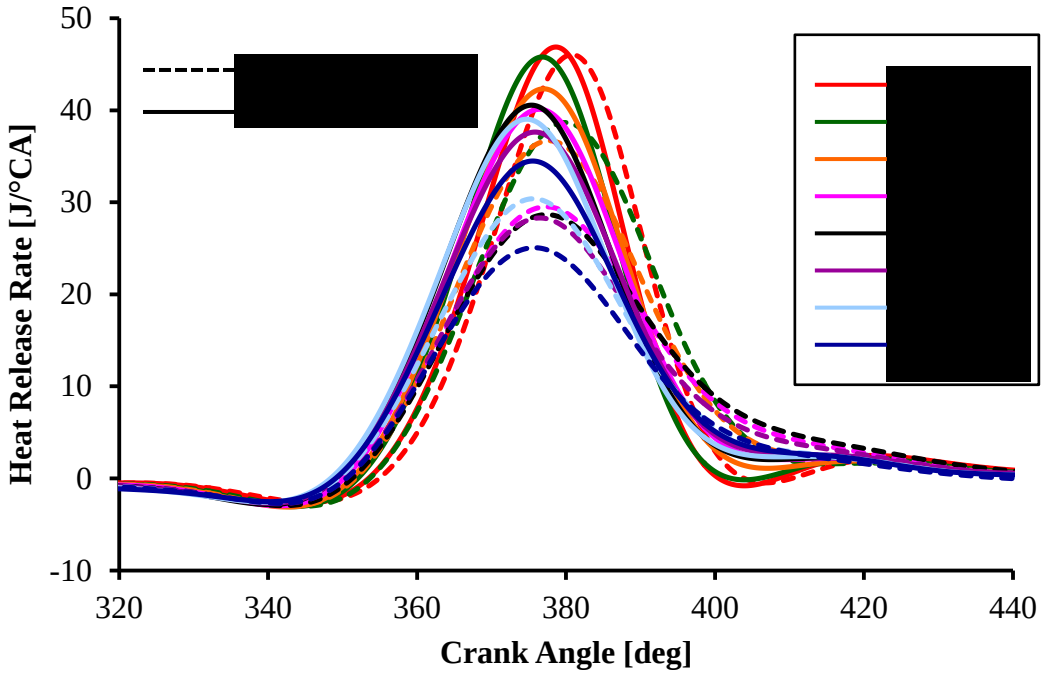

Figure D-2: Effect of Enhanced Swirl on the Heat Release Rate

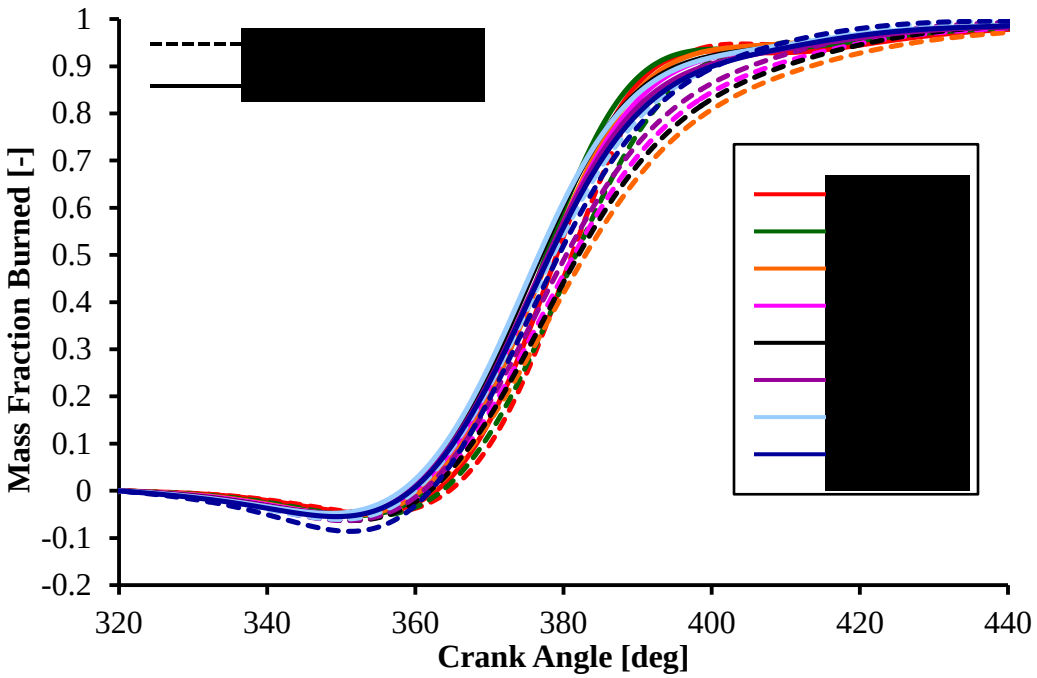

Figure D-3: Effect of Enhanced Swirl on the Mass Fraction Burned

LIST OF PUBLICATIONS

Papers in Refereed International Conference Proceedings

1. Yu, X., Yang, Z., Yu, S., **Ives, M**., Zheng, M., "Impacts of Gas Motion on the Ignition Characteristics of Transistor Coil Ignition Systems," ICEF2017-3657, Proceedings of the ASME Internal Combustion Engine Division Fall Technical Conference, 15 pages, Seattle, WA.
2. Dev, S., Gao, T., Yu, X., **Ives, M**., Zheng, M., "Fuel Stratification and Partially Premixed Combustion with Neat N-Butanol in Compression Ignition Engine," ICEF2017-3676, Proceedings of the ASME Internal Combustion Engine Division Fall Technical Conference, 15 pages, Seattle, WA.
3. Yu, X., Yu, S., Yang, Z., Tan, Q., **Ives, M**. et al., "Improvement on Energy Efficiency of the Spark Ignition System," SAE Technical Paper 2017-01-0678, 10 pages, 2017.
4. Yu, S., Tan, Q., **Ives, M**., Liu, M. Li, L., Chen, X., and Zheng, M., "Parametric Analysis of Ignition Circuit Components on Spark Discharge Characteristics," SAE Technical Paper 2016-01-1011, 11 Pages, 2016.

Papers in Non-Refereed International Conference Proceedings

5. **Ives, M**., Dev, S., and Zheng, M., "Preliminary Investigation of Intake Swirl Motion in a Compression Ignition Engine," Proceedings of Combustion Institute – Canadian Section Spring Technical Meeting, 6 Pages, 2016, Waterloo, ON.

6. Yang, Z., Aversa, C., **Ives, M.,** Divekar, P., Ting, D., and Zheng, M., "Hydrogen as a By-Product of Diesel Engine Low Temperature Combustion" Proceedings of 2015 Natural Gas & Hydrogen Storage Symposium, 7 Pages, June 2015, Windsor, ON.

Selected Poster Presentations

7. **Ives, M**., Aversa, C., Jeftic, M., "Biofuels for Advanced Engine Technologies," NSERC CREATE Program in Clean Combustion Engines, Combustion Summer School, 2016, Toronto, ON.
8. **Ives, M**., Aversa, C., Jeftic, M., Gao, T., Xie, K., Zheng, M., "Biofuels for Advanced Engine Technologies," Auto21 Annual Conference, 2015, Ottawa, ON.
9. Yanai, T., Han, H., Gao, T., **Ives, M**., Yu, S., "Engine Efficiency Improvement Using Biofuels in Compression Ignition Engines," Ford Canadian Appreciation, 2014, Dearborn, MI.

VITA AUCTORIS

Mark Ives was born in Windsor, Ontario in 1989. After completing his high school studies at Holy Names Secondary School in Windsor, Canada, he attended St. Clair College where he obtained an advanced diploma in mechanical engineering technology in 2010. Mark continued his education joining the University of Windsor's mechanical engineering program. While at Windsor, he was an active member of the Formula SAE team. He graduated in 2014 and received his Bachelor's Degree in Applied Science with Distinction. Mark joined the Clean Combustion research group as a graduate student in 2015. He is currently a candidate for the Master's Degree in Applied Science at the University of Windsor and plans to graduate in fall 2017.